Heralded Quantum Imaging

Reuben S. Aspden

A thesis submitted in fulfilment of the requirements for the degree of
Doctor of Philosophy

School of Physics and Astronomy
College of Science and Engineering
University of Glasgow

June 2015

Abstract

Imaging systems play a crucial role in shaping understanding of our surroundings. Modern imaging systems enable the acquisition of images of objects at length-scales and resolutions previously deemed impossible. However, as the drive for better images and novel applications increases, several questions fundamental to our understanding of imaging are being raised. We are familiar with images containing many millions of photons, but how many photons does it take to form an image? In scenarios requiring covert imaging, or where high-light levels damage the sample being imaged, is it possible to image a sample with a very small number of very low-energy photons? This thesis will focus on answering these two questions.

In order to answer these questions I developed a heralded quantum imaging system. The strong spatial correlations inherent between down-converted twin photons have been utilised in many quantum imaging techniques for the past 25 years. Thus far, standard quantum imaging techniques have relied on scanning a fibre detector across the field of view in order to measure the spatial information in the image. However, the scanning mechanism fundamentally limits the detection efficiency of the imaging system.

Recent years have seen an increased interest in using the latest camera technology within quantum imaging systems. The advent of single-photon-sensitive cameras has opened up new possibilities within the quantum imaging field. It is now possible to obtain images of objects by detecting very low-light illumination across the full scene simultaneously.

In the heralded quantum imaging system presented in this thesis, a combination of quantum mechanics and a high-sensitivity camera was employed to obtain high

contrast images containing very few photons. This was the first such system built. Using the correlations between the twin photons generated by our down-conversion source, and our development of compressive sampling techniques to post-process the acquired data enabled the acquisition of an image containing an average of only 0.5 photons per pixel. This represents a significant reduction when compared with a conventional image that contains of order 10^5 photons per pixel.

I also developed this imaging system to use twin photons at vastly different wavelengths. The object was probed with low-energy infrared photons whilst the image was developed on a camera using the correlated visible photon. This disparity in energy between the two photons enabled the acquisition of images using only several thousand photons, corresponding to an energy deposition on the sample of only a few pJ.

Contents

List of Figures

List of Tables

Acknowledgements

I owe a huge debt of gratitude to many people for getting me to this position. Many have provided food, cake or wine! Some expert advice, some support and encouragement, and others have simply put up with my bad jokes and terrible dancing.

A massive thanks is due to Miles: for taking me on, supervising me and giving me many opportunities to learn, meet new people, try new things and enjoy delving into the world of optics as part of a relaxed and inspiring research group. Dan Tasca taught me an incredible amount, and put up with an endless stream of stupid questions as I tried to find my feet at the beginning. He (and the rest of the quantum optics group) was also really welcoming and helpful in Rio when I went out to visit. Peter has joined me in many an enjoyable day (and almost as many frustrating days!) in the lab and has been a pleasure to work with. As has Nathan for the (extended!) time he came through to work with us. I have badgered many people for help, advice and problem solving skills over the course of the past 3 and a half years, not least Graham Gibson, Matt Edgar and Neal Radwell, all of whom have indulged my questions with much patience! The folks in the optics group as a whole have been a great colleagues and friends to work alongside. Large amounts of cake, random conversations over lunch and learning to unicycle are particular highlights of the past few years! Thank you also to many collaborators and helpful folks I've met along the way, particularly to those in the Quantum Theory group at Glasgow (formerly Strathclyde).

I'm incredibly grateful to the InnerCHANGE Glasgow team and the folks at Clay Community Church, for food, wine, chat, support through hard times and lots of great times in between. It's great having a community that remind you to rest, have fun and that there's much more to life than work! Thanks to countless friends who

have heard me moan, and get excited, and made life outside of work great so that regardless of what happens in the lab life is good! And finally thanks to my family for advice and encouragement, and words of wisdom when I got overexcited or too morose with the whole thing.

Declaration of Authorship

I hereby declare that this thesis is the result of my own work, except where explicit reference is made to the work of others, and has not been presented in any previous application for a degree at this or any other institution.

Reuben S. Aspden

Publications

This thesis is the culmination of the work carried out during my PhD in the Optics group at the University of Glasgow, under the supervision of Prof. Miles Padgett. A list of the peer-reviewed papers co-authored in the three and a half years of the PhD programme is given below.

1 R. S. Aspden, D. S. Tasca, R .W. Boyd and M. J. Padgett, "EPR-based ghost imaging using a single-photon-sensitive-camera". *New J. Phys.*, 15(073032), 2013.

2 D. S. Tasca, R. S. Aspden, P. A. Morris, G. Anderson, R .W. Boyd and M. J. Padgett, "The influence of non-imaging detector design on heralded ghost-imaging and ghost-diffraction examined using a triggered ICCD camera". *Opt. Express*, 21(25):30460-30473, 2013

3 R. S. Aspden, D. S. Tasca, A. Forbes, R .W. Boyd and M. J. Padgett, "Experimental demonstration of Klyshko's advanced-wave picture using a coincidence-count based, camera-enabled imaging system". *J. Mod. Optic.*, 61(7):547–551, 2014.

4 P. A. Morris, R. S. Aspden, J. E. C. Bell, R .W. Boyd and M. J. Padgett, "Imaging with a small number of photons". *Nat. Commun.*, 6 (5913), 2015.

Additionally, two papers are currently in preparation for submission.

1 R. S. Aspden, N. R. Gemmell, P. A. Morris, D. S. Tasca, M. Tanner, R. Kirkwood, L. Mertens, A. Ruggeri, A. Tosi, R. W. Boyd, G. S. Buller, R. H. Hadfield and M. J. Padgett, "Visible imaging with infrared illumination: Ghost-microscopy".

2 D. S. Tasca, L. M Rudnicki, R. S. Aspden, M. J. Padgett, P. H. Souto Ribeiro and S. P. Walborn, “Testing for entanglement with periodic images”.

Abbreviations

AR	**A**nti- **R**eflection
AWP	**A**dvanced **W**ave **P**icture
BBO	β- **B**arium **B**orate
BS	**B**eam **S**plitter
DCT	**D**iscrete **C**osine **T**ransform
DDG	**D**igital **D**elay **G**enerator
DI	**D**irect **I**maging
DMD	**D**igital **M**icromirror **D**evice
EMCCD	**E**lectron **M**ultiplying **C**harge-**C**oupled **D**evice
EPR	**E**instein **P**odolsky **R**osen
FOV	**F**ield **O**f **V**iew
GI	**G**host **I**maging
HE	**H**eralding **E**fficiency
ICCD	**I**ntensified **C**harge-**C**oupled **D**evice
IR	**I**nfra**R**ed
NA	**N**umerical **A**perture
PBS	**P**olarising **B**eam **S**plitter
PPKTP	**P**eriodically **P**oled **P**otassium **T**itanyl **P**hosphate
PSF	**P**oint **S**pread **F**unction
QE	**Q**uantum **E**fficiency
ROI	**R**egion **O**f **I**nterest

SBR	**S**ignal to **B**ackground **R**atio
SLM	**S**patial **L**ight **M**odulator
SNR	**S**ignal to **N**oise **R**atio
SNSPD	**S**uper-conducting **N**anowire **S**ingle **P**hoton **D**etector
SPAD	**S**ingle **P**hoton **A**valanche **D**etector
SPDC	**S**pontaneous **P**arametric **D**own **C**onversion
SWIR	**S**hort **W**ave **I**nfrared
TI	**T**riggered **I**maging
TTL	**T**ransistor **T**ransistor **L**ogic

"Am I jumping the gun, or are the words 'I have a cunning plan' marching with ill-deserved confidence in the direction of this experiment?"

Blackadder (adapted)

Chapter 1

Introduction

1.1 Preamble

Imaging systems fundamentally shape the way we perceive, understand and describe our surroundings. From the very early experiments investigating optical phenomena through to the development of microscopes and telescopes which allow measurements at extreme length scales, the ability to image an object and record the results has been pivotal to furthering our understanding of the universe.

Imaging apparatus have developed in tandem with human society, from the apparent use of pinhole cameras in the Palaeolithic era [1], through lenses in the great civilisations of antiquity [2, 3], on to more recognisable optical instruments such as spectacles from the early 12th century [4] and to the ubiquitous high quality cameras of today. With each technological advance, the applications of these technologies to the field of imaging have become increasingly ingenious, enabling a myriad of modern imaging techniques. It is now possible to image at very low light levels [5, 6], at extremely high resolutions [7], across a wide frequency bandwidth [8] and even without the camera actually "seeing" the object being imaged [9–11].

The advancement of detector technology has placed imaging at the heart of modern society. Most people now carry a smartphone with an integrated multi-megapixel camera, whilst easy internet access ensures images can be shared quickly and easily via a wide range of platforms. Given the plethora of imaging technologies, speed of technological advance and ubiquitous use of imaging apparatus, one could be forgiven for thinking the field of imaging had advanced beyond fundamental physics research and was now the preserve of materials scientists and engineers.

However, as the technological level of cameras increases, questions of a different scale are being raised. Cameras contain an ever increasing number of pixels, but is it possible to image using just one pixel? An average image contains approximately 10^5 photons per pixel [12], but how many photons are needed to create a distinguishable image? As we push the boundaries on what we wish to measure and sample in the drive to discover and understand more about our surroundings, is it possible to utilise novel quantum imaging techniques to probe even smaller length scales, using even less energy? These questions have inspired a range of interesting and exciting research areas, throwing up some unexpected answers [6, 13–15].

The research presented in this thesis predominantly addresses two of these questions:
- "How many photons does it take to form an image?"
- "Is it possible to image a sample with a very small number of very low-energy photons?".

In order to answer these questions, my coworkers and I have developed an imaging technique that uses a combination of quantum mechanics and the latest camera technology. We utilise spatial correlations between twin photons to develop an image of a sample using photons that have not themselves directly interacted with the sample. In this thesis I shall present the development of this imaging technique and the results obtained thus far, with reference to answering the above questions. The experimental work in chapters 2, 3 and 6 was carried out alongside Dr. Daniel Tasca,

the work in chapter 4 with Peter Morris and the work in chapter 5 with Peter Morris and Nathan Gemmell. In this thesis I shall distinguish between work performed solely by myself and work performed as part of a team by the use of "I" and "we".

In chapter 3, I shall show that it is possible to image using both the position correlations and momentum anti-correlations inherent in a quantum source, and in chapter 4 show that using statistical techniques enables the acquisition of an image with fewer than 0.5 photons per pixel. Using the same heralded imaging technique, chapter 5 presents the transfer of image data from infrared wavelengths to visible, thus enabling the use of standard cameras in the acquisition of images beyond their conventional technological capabilities. I shall also explore the theoretical considerations concerning optimising this imaging experiment in chapter 6.

In this introductory chapter I shall detail the historical background of the heralded quantum imaging technique, the previous work which inspired this thesis, and some of the theoretical background.

1.2 Correlations and Entanglement

The experiments presented in this thesis rely on strong transverse spatial correlations between two photons. These correlations are inherent in the entangled photon pairs generated through the spontaneous parametric down-conversion (SPDC) process. In this section I shall discuss what is meant by correlations and entanglement and the role they play in the imaging process.

Whilst it is not uncommon to encounter strong correlations in everyday life - if I see a wet umbrella in the corridor I can be fairly convinced it's raining outside without having to go and check - entangled states exhibit strong correlations in complementary variables and it is these correlations that led to Einstein's famous

"Spooky action at a distance" and various other counter-intuitive phenomena [16–19].

Following reference [20], we describe an entangled state by first defining a pure state of two quantum systems, a and b,

$$|\psi\rangle = |\lambda\rangle_a |\phi\rangle_b \,. \tag{1.1}$$

According to the superposition principle, any superposition of product states (*i. e.* composite states that are described by the product of two pure states, such as those in equation 1.1) is also an allowed state of our two systems. We can therefore consider the two qubit state, a two-state quantum-mechanical system,

$$|\psi\rangle = \frac{1}{\sqrt{2}}(|0\rangle_a |0\rangle_b + |1\rangle_a |1\rangle_b) \,. \tag{1.2}$$

This particular superposition of product states cannot be expressed separately as a product of one state for system a and a separate one for system b, as in equation 1.1. States which have this property are entangled. It is important to note that being a superposition of states alone is not sufficient to guarantee entanglement, rather it is the condition that it is impossible to express the state as a product of pure states that makes a state entangled [20]. Intuitively, this can be understood by considering an interaction between two states. A system containing states that have never interacted with each other will always be able to be expressed as a product of pure states. However, if there is an interaction between the two states such that some form of indistinguishability is introduced (*i. e.* a beam splitter that erases information about the source of the photon emerging from each output port), the overall system after this interaction could no longer be expressed as a product of pure states and so would be entangled.

When confronted with an entangled state, such as the one described by equation 1.2, one sees that the measurement of one part of the system gives information about other, non-local parts of the system. It was this aspect of entanglement that led to the famous paper by Einstein, Podolsky and Rosen (EPR) [16] where they argued that this quantum mechanical description of reality must be somehow incomplete. Assuming locality, they argued that the ability to infer the state, for example position, of one particle based on the measurement of a spatially separate particle meant that both the position and the momentum of these particles were simultaneous realities - a violation of the Heisenberg uncertainty principle. This was later formalised as the EPR-paradox, and is resolved by relaxing the insistence on realism or locality. Correlations which violate the inequality

$$\Delta^2_{\min}(x_1|x_2)\Delta^2_{\min}(p_1|p_2) > \frac{1}{4} \tag{1.3}$$

where $\Delta^2_{min}(x(p)_1|x(p)_2)$ is the variance of the position (momentum) of particle 1 based on a measurement of the position (momentum) of particle 2, are described as EPR states and violating this inequality is the weakest (and easiest to perform) measure of entanglement [21–23].

The entangled nature of SPDC sources has provided a rich test bed for demonstrations of the EPR paradox and quantum entanglement [22]. However, in this thesis the entangled nature of the photons produced in the SPDC process is largely redundant. The heralded nature of our imaging system requires strong temporal and spatial correlations between a pair of photons, such that the detection of one photon gives precise spatial information about the other photon, detected at a well defined relative time. Were a reliable, highly position-correlated, twin-photon classical source available, it could also fulfil these criteria.

The above spatial and temporal criteria are valid for the majority of experiments presented in this thesis. However, the experiment presented in chapter 3 also requires strong correlations between the momenta of the two photons. These additional correlations are accessible through using the EPR nature of a quantum source. This additional feature, and the absence of a classical source that displays all the necessary correlations, promote the use of a quantum source for the heralded imaging system.

1.3 Spontaneous Parametric Down-Conversion

The parametric nature of the SPDC process and the phase matching conditions mean the joint quantum state of the generated photons is highly entangled [22–28].

The experiments presented in this thesis, and the quantum ghost imaging technique, rely on the transverse spatial correlations inherent between the twin photons generated through the SPDC process. The spatial and temporal correlations between the optical fields generated through SPDC were first observed by Burnham and Weinberg [29]. Since then, there has been a rich thread of research investigating the strength of these correlations, both temporal [30, 31] and spatial [17, 19, 32, 33], and the relationship between the angular spectrum of the pump beam and the observed spatial correlations between the down-converted photons [34]. Given the commonplace application of SPDC sources in many different areas of optics, it is remarkable to consider that such methods were only first observed a little over 25 years ago. I will present a brief overview of the important features in SPDC within the remit of this thesis here; a more detailed overview of spatial correlations in SPDC is available in the review by Walborn *et al.* [22].

Parametric down-conversion is a process whereby a high energy photon undergoes a non-linear interaction in a medium, generating two lower energy photons called the

signal and idler. This is a second-order interaction, governed by the $\mathcal{X}^{(2)}$ component of the non-linear Hamiltonian for the electromagnetic field [22, 24], where $\mathcal{X}^{(2)}$ is the second-order non-linear susceptibility of a medium and is a term of the induced dipole moment per unit volume, P. This is described by [35]

$$\boldsymbol{P} = \epsilon_0[\mathcal{X}^{(1)}\boldsymbol{E} + \mathcal{X}^{(2)}\boldsymbol{E}^2 + \mathcal{X}^{(3)}\boldsymbol{E}^3 + ...] \tag{1.4}$$

where E is the electric field amplitude. For condensed matter, $\mathcal{X}^{(1)}$ is of order 1 m/V, where as the second-order non-linear susceptibility is approximately 12 orders of magnitude smaller at $\sim$ 1 pm/V, and it is therefore clear that SPDC occurs predominantly for large electric field amplitudes. It is also worth noting that $\mathcal{X}^{(2)}$ effects occur only in noncentrosymetric crystals, as symmetry considerations require that the second-order component of P vanishes identically [35].

For the SPDC process to occur momentum and energy must be conserved,

$$\boldsymbol{k}_p = \boldsymbol{k}_1 + \boldsymbol{k}_2 \tag{1.5}$$

$$\omega_p = \omega_1 + \omega_2 \tag{1.6}$$

where $\boldsymbol{k}_{p,(1,2)}$ and $\omega_{p,(1,2)}$ are the wavevectors and angular frequency of the pump and signal and idler photons respectively. These are known as the phase-matching conditions [29]. Ordinarily, the energy of the pump photon is split evenly, giving degenerate signal and idler photons with $\omega_1 = \omega_2 = \omega_p/2$, although it is also possible to work with correlated photons far from degeneracy, as presented in chapter 5 of this thesis and references [36, 37].

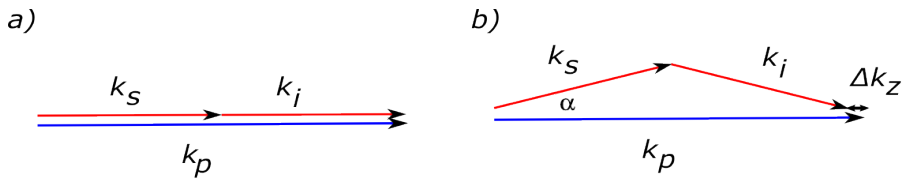

FIGURE 1.1: **Phase Matching**: a) Collinear and b) Near-collinear phase matching. In order for SPDC to take place the vector sum of the wavevectors of the down-converted photons must equal the wavevector of the pump. There is a certain allowed wavevector mismatch, Δk_z that determines the emission angle, α.

Within the phase-matching criteria there is a certain permissible wavevector mismatch, Δk_z, between the wavevectors of the pump, signal and idler fields, as shown in figure 1.1. The efficiency of the down-conversion process depends on this axial mismatch and scales as $\text{sinc}^2(L\Delta k_z/2)$ [38]. As well as determining the efficiency of the down-conversion process, Δk_z also determines the angle of emission of the down-converted photons. The experiments in this thesis work in a near-collinear phase-matching regime, which means that the photons are emitted over a narrow range of angles, $L\Delta k_z \lesssim \pi$ [38], where L is the length of the non-linear crystal. In the near collinear regime, the phase mismatch can be written

$$\begin{aligned} \Delta k_z &= k_p - 2\cos(\alpha)k_s\,, \\ &\simeq k_p - k_p\cos\alpha\,, \\ &\simeq \frac{\alpha^2 k_p}{2}. \end{aligned} \tag{1.7}$$

This leads to a maximum emission angle for the down-converted photons of

$$\alpha^2 \lesssim \frac{2\pi}{k_p L}. \tag{1.8}$$

The phase-matching criteria are dependent on the refractive index of the crystal due to the refractive index dependence of the frequency, $\omega = \frac{ck}{n}$, and are most commonly met by exploiting the birefringence displayed by many crystals. Where this is not possible, for instance when a crystal does not display birefringence, quasi-phase matching is achieved by periodically inverting one of crystalline axes [35]. There are two commonly used non-linear crystals for the SPDC process, both exhibiting a high $\mathcal{X}^{(2)}$ component; $\beta-$barium borate (BBO) crystals and periodically poled potassium titanyl phosphate crystals (PPKTP). The birefringence of BBO crystals allow phase-matching whereas PPKTP crystals rely on quasi-phase-matching. PPKTP sources have a higher brightness than BBO sources; indeed, using PPKTP crystals in SPDC has achieved a generation rate of 273000 pairs s^{-1} mW^{-1} nm^{-1} [39]. In our system, using a pump power of $\sim$ 100 mW, a BBO crystal and a detection bandwidth of 10 nm, we generated approximately 250000 photon pairs per second. In comparison, for similar experimental parameters the above quoted SPDC pair generation rate using PPKTP crystal would be 2.73×10^8, three orders of magnitude higher.

Phase matching is typically accomplished by either angle tuning or temperature tuning. Angle tuning is commonly used to achieve phase-matching with BBO crystals. By rotating the crystal around an appropriate axis [40], the relative contributions to the refractive index from the ordinary and extraordinary axes can be changed until the phase-matching refractive index is matched. This carries the drawback that, aside from when the crystal is oriented at 0° and 90°, the Poynting vector and propagation vector are not parallel for extraordinary rays. Therefore, ordinary and extraordinary rays diverge from each other during propagation through the crystal leading to walkoff effects. This is particularly problematic if using a long crystal [35]. Temperature tuning does not induce walkoff effects, and is commonly used with PPKTP crystals where the refractive index has a strong temperature dependence [41, 42].

SPDC processes fit into two categories: type I, where both down-converted photons

have orthogonal polarisations to the pump photon, and type II, where the down-converted photons have orthogonal polarisations to each other. These two categories arise from the phase matching criteria, and are particularly intuitive when considering phase-matching in birefringent crystals where the refractive index depends on the direction of polarisation of the incident optical radiation. The experiments in this thesis used type-I down-conversion.

In the experiments presented in this thesis, we worked in a very low-light regime ($\ll 1$ generated SPDC pair per pump laser pulse) and as such did not need to consider the brightness of the source. The ease of phase matching and pair-generation when using BBO crystals therefore made BBO an ideal source of down-converted photons for use in the lab.

1.4 Ghost Imaging

In 1995 Pittman *et al.* [43] demonstrated the first instance of a novel coincidence imaging technique, dubbed "ghost imaging" (GI) due to its counter-intuitive, "spooky" characteristics. Using an entangled photon pair, they created a system where one photon probed an object and was detected by a single pixel detector, whilst the other photon, which never interacted with the object was detected by a detector which scanned across the scene, as shown in figure 1.2. Although neither detector alone was capable of resolving the object, a 2D image was retrieved from the sum of many coincidence measurements made between these two detectors.

Presumed initially to be a feature of entanglement, it was therefore believed GI was fundamentally reliant on quantum mechanics. In the years that followed, the reliance on entanglement in GI was heavily debated and these discussions led to subsequent demonstrations utilising purely classical correlations. In these systems the SPDC source was replaced with a thermal source, and the correlations were detected between

the classical fields detected at each detector [44, 45]. Rigorous analysis has shown that classical GI systems can recreate almost all aspects of quantum GI. Indeed, it is now commonly accepted that the only distinctive feature of quantum GI is the ability to acquire high-visibility images in both the near and far-field of the source [25, 46–49].

More recently, a new branch of classical GI has evolved utilising programmable devices, such as spatial light modulators (SLM's) or digital micromirror devices (DMD's), capable of spatially modulating light fields [9, 14, 50, 51]. As the spatial modulation applied to the incident light field is programmed and therefore recorded on a computer, there is no longer any need to record the intensity distribution of the light field on a CCD. Therefore, one can utilise the correlation between the light measured by only one single-pixel detector, and the spatial information of the incident light field stored in computer memory to reconstruct the image using the same statistical process as implemented in classical GI. This is termed computational GI. The rapid modulation rates of such devices and ever increasing computer processing power has opened the door for the development of novel imaging solutions, useful for instance in cases where existing detector arrays are limited [52].

The advances in classical and computational GI have evolved to answer several of the questions raised in section 1.1. They cannot, however, answer the questions that form the aim of this thesis, and the rest of this thesis will therefore focus solely on quantum GI and related heralded imaging techniques.

1.5 Quantum Ghost Imaging

The first GI experiment [43] utilised quantum entangled photons generated through the spontaneous parametric down-conversion (SPDC) process. A simplified schematic of the experimental setup used is shown in figure 1.2. A pump beam was incident

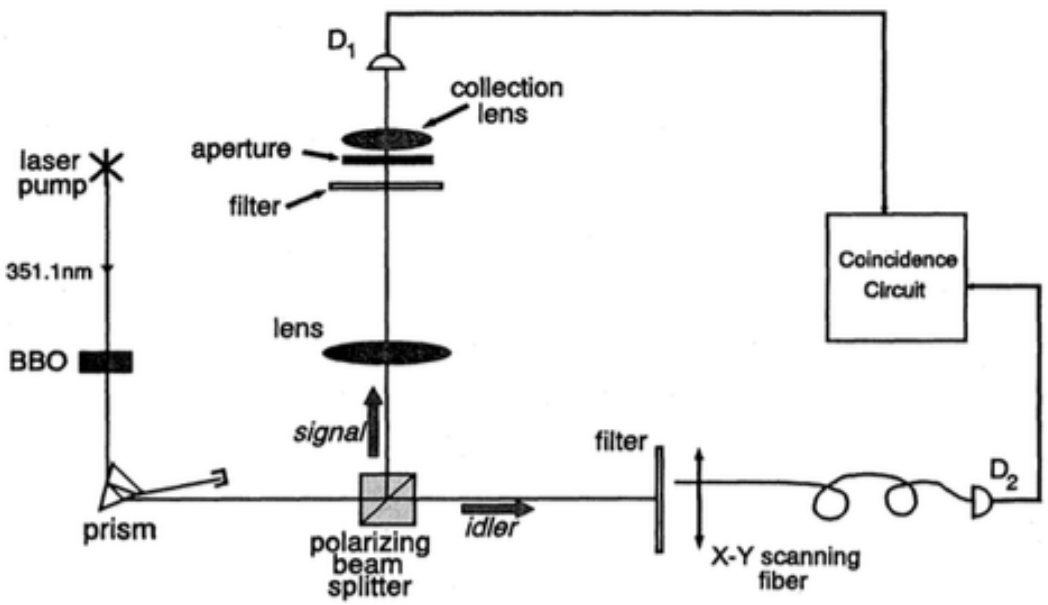

FIGURE 1.2: **Schematic of the first ghost imaging experiment [43]:** Correlated photons generated in the SPDC process were split at a polarising beam splitter (PBS). The signal photon probed an aperture, a binary mask displaying the letters UMBC - the intials of their institution - and was detected by a bucket detector, the idler photon was detected by a scanning single mode fibre. An image of the object was obtained in the coincidence counts.

on a β-barium borate (BBO) crystal which generated a down-converted pair of photons, termed the signal and idler. A polarising beam splitter (PBS) sent the signal and idler photons into two separate optical paths. The signal photon was incident on a transmissive object and, if transmitted, was subsequently collected by a large area single-pixel detector, often referred to as a "bucket detector". The detector registered the presence of the photon but was not capable of resolving spatial information. Meanwhile, the idler photon, which did not propagate along the path of the object, was recorded by a scanning fibre detector. This detector recorded the spatial distribution of the idler photon, but clearly measured no information about the object. Whilst it was impossible to obtain an image of the object using the measurements from each detector alone, by summing many photon pairs measured in coincidence a reconstruction of the object was deduced.

In general, subsequent investigations of quantum GI can be categorised by two different research objectives: performing fundamental tests of quantum mechanics or the development of novel imaging applications. Investigations of the former include demonstrating entanglement by going beyond the well known EPR bound, as described by equation (1.3) [23, 25], as well as utilising alternative variables as the measurement basis [53, 54]. In the pursuit of novel imaging applications, some experiments have sought to enhance the optical efficiency by using compressive techniques to reduce the number of measurements required [5, 15, 55]. By replacing the scanning detector with a bucket detector and patterning the incident light field collected by the two bucket detectors using programmable devices, they exploited characteristics of real images to statistically reconstruct an image using significantly fewer measurements than ordinarily required by the Nyquist limit.

Although ghost imaging was one of the first imaging systems that utilised the spatial correlations in down-converted light, many other notable quantum imaging examples have also been developed. These include a non-local Young's double slit experiment [17], a type of advanced quantum interference [19, 36] and detection of non-local optical vortices [56]. However, whilst each of these systems demonstrates fascinating quantum effects, not one of them is able to answer the questions raised in section 1.1.

All of the aforementioned GI techniques have utilised systems based on a scanning fibre detector to detect the spatial information of the correlated photons. This is a result of the historical development of the technique from a simple coincidence system common to many quantum optics laboratories, to point-to-point correlation measurements by scanning a single-mode fibre. It was a solution to detecting orthogonal spatial states in the absence of single-photon-sensitive cameras. However, this scanning approach fundamentally limits the detection efficiency of the technique to a maximum of $1/N$, where N is the number of pixels in the final image. When wishing to image with a very low number of photons, this fundamental limit in detection

efficiency renders such imaging systems impractical. In the work presented in this thesis, I utilised a camera which can detect across the full field of view (FOV) of the system, thus removing the need to sequentially sample each pixel in the scene. This was used in a heralding system such that it only imaged a photon when triggered by the detection of a photon in the other arm of the system. Using this heralded imaging technique enabled full-field, low photon number, low noise imaging, as I shall describe in the following chapters.

1.5.1 Theoretical background

I shall now formulate the theoretical background to quantum ghost imaging. The initial theoretical framework presented here is applicable to an imaging system similar to the original Pittman *et al.* [43] experiment where a bucket detector collects all transmitted photons through the object and a scanning detector measures the correlated photons propagated along a separate optical path. I shall then expand on this framework to describe the heralded imaging system used throughout this thesis.

We assume frequency degenerate SPDC, pumped using a beam with a large Gaussian transverse profile and use the thin crystal approximation, an approximation that allows us to ignore birefringent walkoff effects in the crystal. In this case the spatial structure of the two-photon field can be described as

$$|\Psi\rangle = \int d\boldsymbol{\eta}_1 d\boldsymbol{\eta}_2 \Psi(\boldsymbol{\eta}_1, \boldsymbol{\eta}_2) |\boldsymbol{\eta}_1\rangle |\boldsymbol{\eta}_2\rangle \,, \tag{1.9}$$

where η_1 and η_2 are the transverse coordinates at the SPDC source and $|\eta\rangle$ is the pure state of a single photon in transverse position η [22, 34, 57].

If we assume an EPR, non-separable state [58] we can write the transverse wavefunction Ψ in the form

$$\Psi(\boldsymbol{\eta}_1, \boldsymbol{\eta}_2) = T(\boldsymbol{\eta}_1 + \boldsymbol{\eta}_2)\Gamma(\boldsymbol{\eta}_1 - \boldsymbol{\eta}_2)\,, \tag{1.10}$$

where T is the transverse beam profile and Γ is the Fourier transform of the phase-matching function, $\gamma(\boldsymbol{H}) = \sqrt{2L/K\pi^2}\mathrm{sinc}\left(\frac{L|\boldsymbol{H}|^2}{4K}\right)$, where L is the length of the crystal, K is the wave number of the pump beam, $\boldsymbol{H}$ is the Fourier transform of η and $\mathrm{sinc}(x) = \sin(x)/x$. As Γ is much narrower than T, the transverse positions of the photons are correlated [22, 34, 59]

The generated photon pair described by equation (1.9) is split at a beam splitter (BS) such that photon 1 propagates along the path containing the object and bucket detector, and photon 2 propagates along the path containing the spatially resolving detector.

The photon in the object path is incident on a transmissive object with an aperture function described by $A(\boldsymbol{\eta}_1)$ where $A = A^*$, *i. e.* the function is real (an intensity mask). It is collected by a multimode bucket detector which records photons across all spatial modes. Thus the detected spatial state of the photon in the object path at the bucket detector is described by

$$|\phi_1\rangle = \int d\boldsymbol{\eta}_1 g_1(\boldsymbol{\eta}_1)|\boldsymbol{\eta}_1\rangle\,, \tag{1.11}$$

where $g_1(\boldsymbol{\eta}_1)$ is the transfer function of the spatial properties of the beam from the crystal to the detector in the object arm, and is a convolution of the aperture function and the relay optics.

The photon in the detector path propagates through the system and is detected by a scanning single mode detector. The detected spatial state in the detector path is therefore described by

$$|\phi_2^i\rangle = \int d\boldsymbol{\eta}_2 f_i(\boldsymbol{\eta}_2)|\boldsymbol{\eta}_2\rangle\,, \tag{1.12}$$

where $f_i(\boldsymbol{\eta}_2)$ is a function of the spatial properties of the beam at each detection point i and a subset of the transfer function of the spatial properties of the beam in the camera arm, such that $\sum_i^N f_i(\boldsymbol{\eta_2}) = g_2(\boldsymbol{\eta_2})$, where N is the number of detection points over the full field of view.

The probability of a coincidence detection at the i^{th} detection point is then given by

$$P_i = |\langle\phi_1|\langle\phi_2^i|\Psi_{1,2}\rangle|^2 = \iint d\boldsymbol{\eta}_1 d\boldsymbol{\eta}_2 \Psi(\boldsymbol{\eta}_1,\boldsymbol{\eta}_2) g_1^*(\boldsymbol{\eta}_1) f_i^*(\boldsymbol{\eta}_2)\,. \tag{1.13}$$

It is clear when one considers the individual measurements at each detector in both paths, described by equations (1.11) and (1.12), that no image of the object is obtained as there is no spatial resolution in the object path and no object in the detector path. In coincidence detection however, described by equation (1.13), there is a clear dependency on both the aperture function from the object path and the spatial information from the detector path.

In order to reconstruct an image using the coincidence counts at each detection point, we describe the average number of photons detected at the i^{th} detection point as

$$\langle D_i\rangle = DQ_iP_i\,, \tag{1.14}$$

where D is the number of photon pairs generated and Q_i is the probability of the detector being in position i. In the case of a scanning fibre, $Q_i = 1/N$. The obtained image is described by

$$G(\boldsymbol{\eta}) = \sum_{i}^{N} \langle D_i \rangle \delta(\boldsymbol{\eta} - \boldsymbol{\eta}_i) \tag{1.15}$$

When one considers the question raised in section 1.1, "How many photons does it take to form an image?", it is clear from the above equation (1.14), that the scanning element within the imaging system fundamentally limits the efficiency of the system, and thus increases the number of photons required to illuminate the sample. The experimental strategy discussed in this thesis increases the maximum efficiency of the system by a factor of N by utilising a time-gated camera in place of the scanning detector. This camera is triggered based on the detection of a photon in the object arm, thus resulting in a heralded detection system. The time delay between measurements in the object and detector arm can be accomodated within the system design and as such the measurements are still described as simple coincidences. Using a multi-pixel camera means that each measurement, rather than asking a binary question (are you in this pixel?), asks a high-dimensional question (which pixel are you in?). This increase in dimensionality of the detector enables the detection across all pixels simultaneously, thereby removing the dependence on Q_i in equation 1.14. Thus the average number of photons detected in the i^{th} pixel of the image is described by

$$\langle D_i \rangle = DP_i \tag{1.16}$$

Whilst the probability of a coincidence detection at each detection point is unchanged and described by equation 1.13, removing the dependence on the probability of the detector being in the i^{th} position results in a $1/N$ increase in detection efficiency.

1.6 Walkthrough

Having presented the historical and theoretical background to the quantum heralded imaging technique, chapter 2 will summarise the experimental setup and methodology. I will describe salient features of each of the main pieces of apparatus and highlight key aspects of their function within the imaging system. I will also discuss how the system is aligned, including a description of Klyshko's advanced-wave picture.

Chapter 3 presents the first experiment performed with a camera-enabled, heralded imaging system. I will present the images obtained with this system in both the image plane and far-field of the source, and discuss how these images highlight the EPR nature of our source.

In chapter 4, the use of this imaging system in low-light imaging applications is discussed. I will present an image processing technique that allows the reconstruction of an image from a very sparse data set, and show how the combination of this technique and our imaging system allows the acquisition of images using very few photons.

Chapter 5 presents a further advancement to the imaging system, where the sample is probed using infrared photons but the image is developed using correlated visible photons. This imaging system demonstrates the ability to image a sample with very few, very low energy photons.

Having presented several experiments which work towards answering the questions posed at the beginning of this thesis, chapter 6 considers the design and implementation of the system, and how to design an optimum system for maximising image

resolution, contrast and acquisition efficiency. I will discuss the influence of the non-imaging heralding detector design, and the source characteristics and how these effect the signal detected at the camera.

Chapter 2

Experimental Methods

2.1 Introduction

All the experiments presented in this thesis, whilst investigating different aspects of the heralded imaging technique, share many common experimental methods and apparatus. In this chapter I will describe these features, including the technical aspects of the equipment and descriptions of techniques that have been developed to aid with building and aligning the system. Aspects of the system that are unique to individual experiments, and variations on this standard setup will be presented in the relevant chapters.

A reduced schematic of the experimental setup is presented in figure 2.1. The imaging system relies on the spatial correlations inherent between the twin photons generated through the SPDC process, as described in chapter 1. The twin photons generated through the SPDC process are split at a BS into two spatially distinct arms of the experiment. In the heralding arm, the photon is incident on a transmissive object before being detected by a single-pixel detector - the heralding detector. The correlated photon is re-imaged through a free-space, image-preserving delay line before being

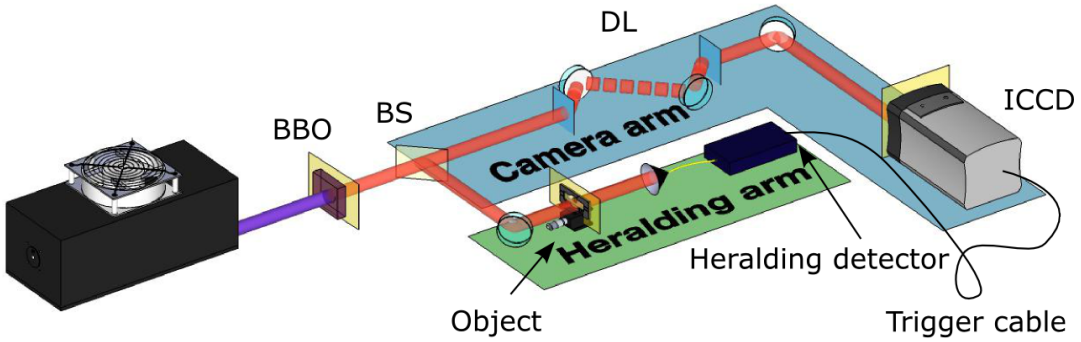

FIGURE 2.1: **Basic experimental setup:** Collinear down-converted photon pairs at 710 nm were generated by pumping a BBO crystal with a UV laser at 355 nm. The yellow planes are all conjugate image planes of the BBO crystal (lenses are removed for clarity). The down-converted photons were split at a beam splitter (BS). One photon probed the object and the transmitted photons were detected by a single-pixel heralding detector. The correlated twin photon passed through an image-preserving delay line before being detected by an ICCD camera. The camera was triggered based on the detection of a photon by the heralding detector. The electronic delay in the trigger mechanism was accounted for by the image-preserving delay line (DL), such that the photon imaged by the camera was the correlated twin of that detected by the heralding detector.

detected by an intensified charge-coupled device (ICCD) camera. The magnification in both arms is $M = 3$, therefore the size of the image on the camera matches that of the object in the heralding arm. In the following section I shall describe the characteristics of our source and equipment, and shall then proceed to discuss building and aligning the system and how we acquired images.

2.2 Experimental Apparatus

2.2.1 Down-conversion source

Our down-conversion source, shown in figure 2.2, consisted of a high-repetition rate laser and a BBO crystal. We used a JDSU Xcyte laser at 355 nm, pulsed at 100 MHz with a temporal pulse width of ≈ 10 ps. The average output power at the laser head was 150 mW. The 355 nm beam was generated through frequency-tripling an ND:YAG pump and so we used a dichroic mirror to filter the spurious laser lines. The beam was then spatially filtered using a 20 μm pinhole at the focus of a 150 mm lens and recollimated to ensure a pure Gaussian mode at the BBO crystal. Our BBO crystal was cut for type-I phase matching, generating a near-collinear down-converted photon pair. We selected the down-converted wavelength through the use of 10 nm bandpass interference filters. SPDC is polarisation dependent and so we were able to attenuate the process on a continuous scale by the use of a neutral density filter and half-wave plate in the pump beam path. This down-conversion source is the same for each experiment presented in this thesis and so in future experimental setup figures the source will be depicted simply as the laser and BBO crystal.

2.2.2 Intensified CCD camera

We captured our images using an ICCD camera. ICCDs use an intensifier tube to multiply the signal from each detected photon, before detecting the signal on a CCD chip. The intensifier mechanism enables a wavelength dependent peak quantum efficiency (QE) (an efficiency describing the percentage of incident photons that generate charge carriers) of up to $\approx 50\%$ [60]. We used an ICCD for our heralded imaging system rather than other types of single-photon sensitive cameras, *e. g.* electron multiplying CCDs (EMCCDs), as they have the ability to utilise a very high timing

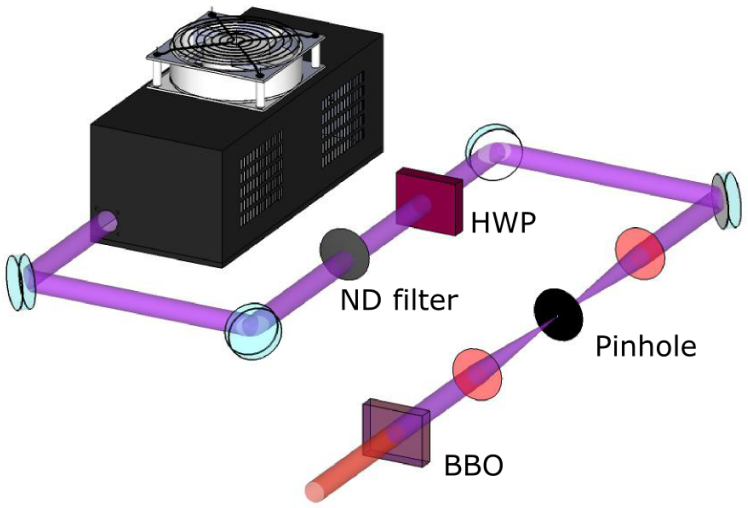

FIGURE 2.2: **SPDC Source:** The 355 nm pump laser was spatially filtered at the focus of a 150 mm lens by a pinhole and recollimated in order to produce a pure Gaussian mode at the BBO crystal. The power of the pump beam was attenuated on a continuous scale by using a neutral density (ND) filter and a half-wave plate (HWP).

resolution [60, 61]. There are two timing measures of note in an ICCD: the exposure time, which determines the time for which a signal is accumulated on the chip before being read out - typically of order several seconds; and the intensifier gate width, which is the time the intensifier fires during each exposure time and is typically of order nano-seconds. The intensifier can be set to fire multiple times during a single exposure. In this case the signal read out from the camera at the end of the exposure time is the signal accumulated on the CCD chip during each gating of the intensifier.

The intensifier can be triggered either internally using a digital delay generator (DDG), or externally using a transistor-transistor logic (TTL) trigger pulse. When triggering the intensifier using an external trigger signal, two different mechanisms can be used to determine the intensifier gate width. The gate can be controlled so as to be ON when the input TTL pulse is high, meaning the gate width is set by the width of the trigger pulse: direct gate mode. Alternatively, the rising edge of the input TTL pulse can be used to trigger the DDG such that the pulse profile is set

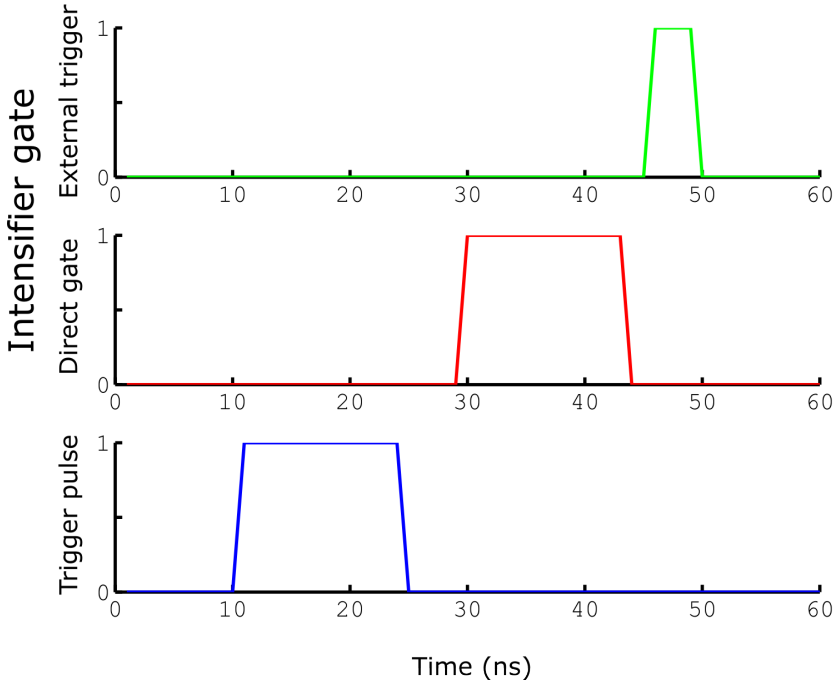

FIGURE 2.3: **ICCD trigger timings:** The blue pulse is a 15 ns TTL trigger pulse from the SPAD. The insertion delay of the camera means the camera intensifier fires later. In the case of Direct Gate triggering, the insertion delay is 19 ns and the pulse width is equivalent to that of the input trigger pulse. For External Triggering, the insertion delay is 34 ns but the intensifier gate width can be set manually, in this case 5 ns.

internally on the camera: external trigger mode. Inherent in both external trigger mechanisms is the electronic delay time associated with inputting a trigger pulse - the insertion delay. In direct gate mode this is $\sim$ 19 ns, whereas in external trigger mode this insertion delay is $\sim$ 35 ns. The timing associated with these trigger mechanisms are shown in figure 2.3. The experiments presented in this thesis utilise both trigger modes as will be stated in the relevant chapters.

The ICCD contains 1024×1024 pixels of pitch 13 µm, giving a FOV of $(13.3 \text{ mm})^2$. Due to the size of the down-converted beam we were detecting, we typically utilised a smaller region of interest (ROI) within each acquisition. This allowed for detection across the full spatial extent of the illuminating beam, whilst decreasing both the readout time and file size of the acquired images.

Two different ICCD cameras were used for the experiments in this thesis, an Andor iStar Gen2 intensifier model and an iStar Gen3 intensifier camera. Both cameras were air cooled to reduce the read-out noise inherent in the camera electronics, the Gen2 intensifier was cooled to $-15°$ and the Gen3 camera was Peltier-cooled to $-30°$. The maximum external trigger rate for the Gen2 camera was 50 kHz compared with 500 kHz for the Gen3 model and the QE at 710 nm improved from $\approx 10\%$ for the Gen2 model to $\approx 35\%$ for the Gen3 model.

2.2.3 Heralding detectors

The external trigger signal used to trigger the ICCD came from the single-pixel detector in the heralding arm of the imaging system. This heralding detector gave a signal for each detected photon that was transmitted through the object but recorded no spatial information. The characteristics of the heralding detector played a large role in determing both the efficiency and FOV of the acquired heralded images, as will be discussed in chapter 6. In this section I shall describe the properties of the detectors we used for our experiments.

Three different detectors were used as heralding detectors in our experiments: a fibre-coupled, free running single-photon avalanche detector (SPAD); a free-space, triggered SPAD; and a fibre-coupled detector based on a super-conducting nanowire (SNSPD). Each of the fibre-coupled detectors utilised a $4\times$ magnification objective lens to focus the incident light onto the input facet of the fibre.

When detecting photons with a wavelength of 710 nm we used an SPCM-AQR series SPAD from Perkin Elmer. This SPAD was fibre-coupled with an active area of 175 μm^2, a QE of $\approx 70\%$ at 710 nm and a dark count rate of ≈ 1000 counts per second. The output pulse was a TTL pulse of width 15 ns. We used this SPAD in free-running mode, where the SPAD was constantly gated.

The triggered SPAD was based on InGaAs/InP (Indium Gallium Arsenide/Indium Phosphate) and designed to detect telecoms bandwidth infrared (IR) photons. It was a free-space detector, with a square active detection area of 625 µm^2 and a numerical aperture (NA) of ~ 0.7. We used a trigger signal from the pump laser to trigger the gate of the SPAD. This correlated the gating of the SPAD with the pulses from the pump, and so allowed us to set a narrow gate width of 1.4 ns, thus reducing dark counts. Within the detection mechanism of a SPAD, there is a small probability that the avalanche detection mechanism is triggered again by the signal from the previous photo-detection. This leads to a double pulse for a single photo-detection. Known as after-pulsing, this can be negated by setting a hold-off time, a period after each detection where the SPAD is blind. In order to determine the optimum hold-off time we acquired several heralded images with hold-off times between 20 µs and 5 µs and varying count rates, as shown in figure 2.4. For each image I also calculated the heralding efficiency (HE), the ratio of photons detected at the camera during the trigger window of the intensifier to photons detected at the heralding detector, shown in table 2.1. The HE is highest for the configuration used in figure 2.4-e). However, by considering the cross-sections of the images it is clear the background in this image is also much higher than in the other images and so, according to this subjective analysis, the optimum configuration is that used to acquire figure 2.4-c) - a hold-off time of 10 µs with 9000 counts per second. A more detailed description of the role of the pump power with respect to the contrast of the heralded image will be discussed in chapter 6. The SPAD was cooled using an inbuilt Peltier system to 230 K and had a QE at 1555 nm of approximately 25 %.

The SNSPD detection mechanism is based on a perturbation of the superconducting state in a nanowire by an incident photon. A nanowire is cooled below its superconducting transition temperature and biased just below the critical current. Absorption of an IR photon triggers the formation of a resistive hotspot followed by an increase

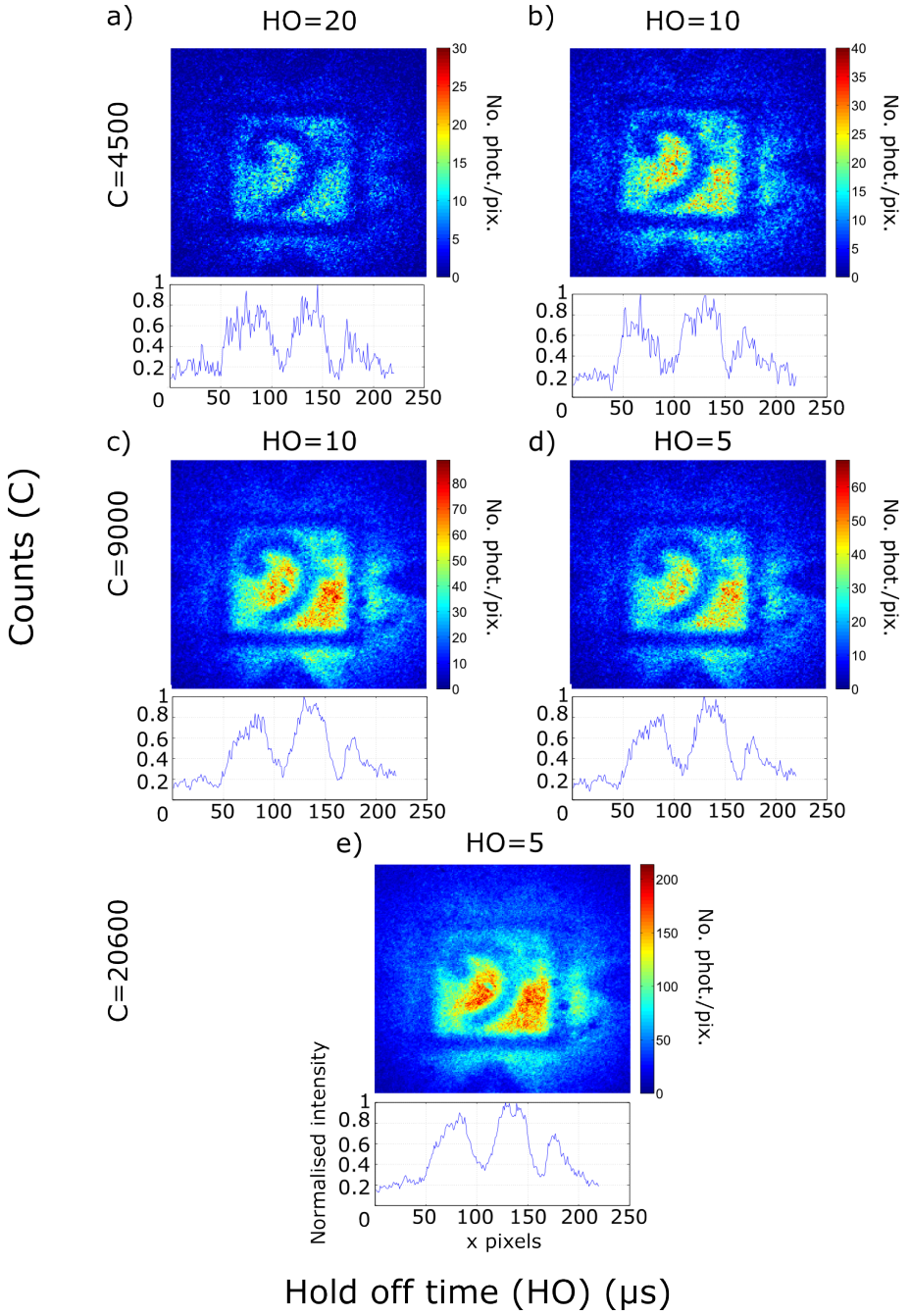

FIGURE 2.4: **Comparision of InGaAs/InP SPAD hold-off times:** The hold-off time of the InGaAs/InP SPAD determines the time the SPAD is blind after each photo-detection. This reduces the probability of after-pulsing effects. These images show the effect of changing the hold-off time and pump laser power. A hold-off time of 10 µs and count rate of 9000, as used to acquire the image in c), subjectively gives the best heralded image with highest quantum efficiency. The Gaussian profile of the down-converted field is apparent in the intensity profile of the heralded images.

Image	Hold-off time (µs)	Trigger rate	No. Phot. Image	HE %
a	20	4500	174×10^3	2.1
b	10	4500	372×10^3	4.6
c	10	9000	1×10^6	6.2
d	5	10600	673×10^3	3.5
e	5	20600	2.757×10^6	7.4

TABLE 2.1: **Comparison of heralding efficiencies for changing InGaAs SPAD hold off times:** The number of photons and heralding efficiencies for each hold-off time and trigger rate used to acquire the images in figure 2.4.

in current density in the surrounding region of the wire. This change in state allows a detectable voltage pulse to be read across the device and amplified using room temperature low-noise amplifiers. Current is shunted out of the wire, which returns to the superconducting state permitting the return of the bias current and another possible detection event. The SNSPD used in the experiment presented in this thesis consisted of a 6 nm thick, 10 nm wide meander NbTiN wire (10 µm × 10 µm area) patterned on a 225 nm SiO_2 layer on top of a silicon substrate, forming a half optical cavity designed for increased absorption at telecom wavelengths. The device was optically coupled via a 9 µm diameter core single mode fiber and housed in a Gifford-McMahon closed-cycle refrigeration system operating at ≈ 3 K. The practical single-photon system efficiency from the fiber input was measured to be ≈ 20% at 1550 nm with ≈ 1 kHz ungated dark count rate.

2.3 Building the System

2.3.1 Delay line

Our imaging system utilised the detection of a photon by an ICCD camera within a precise trigger window, determined by the detection of the correlated twin photon at a single-pixel detector. Inherent in the triggering process was a non-trivial electronic

delay resulting from the readout electronics within the single-pixel detector and the insertion delay of the ICCD. This had to be accounted for so as to ensure the photon detected by the ICCD was the correlated twin of the heralding photon.

In order to fully characterise this electronic delay I initially coupled the camera arm photons into a multimode fibre. The output facet of the fibre was placed beside the camera window and the camera was triggered using the signal from the heralding detector. I changed the length of fibre until I detected a beam on the camera. Using this technique, the total electronic delay of the read-out from the SPAD and insertion delay of the ICCD was found to be $\sim$ 70 ns, corresponding to $\sim$ 23 m free space propagation of a photon.

Our imaging system relies on measuring the spatial distribution of the camera arm photon and therefore the delay line must be image preserving. In order to achieve this we built a free-space, folded imaging system, shown in the full experimental schematic in figure 2.5. We used a type-I down-conversion source with the optical axis of the BBO crystal orientated horizontally, thus generating vertically polarised down-converted photons. The polarisation of the photons in the camera-arm was rotated by 90° using a half-wave plate at 45°, so they were transmitted through the PBS. They were then imaged through the PBS to the input mirror of a telescopic imaging system with unit magnification constructed with 1 m focal length lenses. The photons propagated through this imaging system and were back-reflected along the same path, double-passing through a quarter-wave plate set at 45°, thus rotating the polarisation of the photons back to horizontal. They were therefore reflected when incident again on the PBS and re-imaged on to the camera.

Whilst this form of delay line is long and cumbersome it was the most practical solution we could find after considering various options. For example, we initially used two bespoke curved mirrors. Each mirror had a small hole where the photon could enter/exit the cavity. The mirrors were arranged such that they formed an

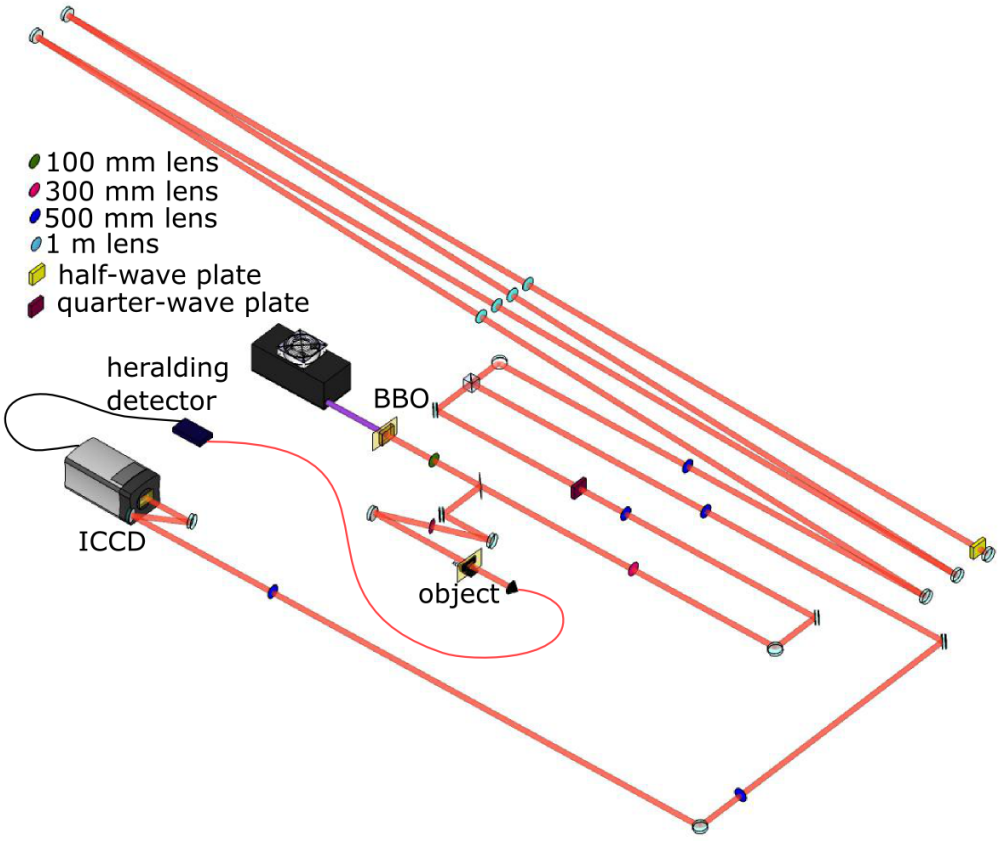

FIGURE 2.5: **Full experimental setup:** Collinear down-converted photon pairs at 710 nm were generated by pumping a BBO crystal with a UV laser at 355 nm. The down-converted beam was Fourier transformed onto the beam splitter. A 300 mm focal-length lens was used after the beam splitter in each path to Fourier transform the down-converted fields at the beam splitter onto the planes of the object and the input plane of an image preserving delay line respectively. The image-preserving delay line consisted of 7 telescopic imaging systems, 4 with 1000 mm focal length lenses and 3 with 500 mm focal length lenses. The total length of the image-preserving delay line was 22 m. The yellow planes indicate image planes of the BBO crystal.

image preserving cavity. However, the radius of curvature of the mirrors gave a cavity focal length of only 30 cm and the 2 inch diameter mirrors supported only ≈ 10 round trips [62], giving a total free space length of ≈ 6.2 m. I also investigated using a fibre based delay line, such as an endoscope. However, the need to preserve the spatial information contained in the photon made this unfeasible, as coupling light into many fibres is very lossy and all commercial fibre based imaging systems I could find had a camera at the input to a fibre, with an electronic signal then

transmitted through the length of the endoscope fibre.

2.4 Aligning the System

2.4.1 Klyshko Advanced Wave Picture

The imaging system had a total free-space optical path-length of 23.4 m; 700 mm in the heralding arm and 22.7 m in the camera arm, as described previously. In order to aid alignment of this system we used a continuous wave (CW) diode laser, emitting at the same wavelength as our down-converted photon pairs, and the Klyshko Advanced Wave Picture (AWP). What follows is an introduction to the AWP, and a description of how we used it in the full alignment process. It is worth noting that as the relay optics and ICCD in the camera arm were multi-mode in nature and we built the system using highly stable mounts, the system only required the full re-alignment process after several weeks of imaging at a time.

2.4.1.1 Introduction to the AWP

The twin photons generated in the SPDC process are highly entangled, and as such have very strong spatial correlations between them, as discussed in section 1.2. However, despite the inherent quantum nature of these correlations, Klyshko showed that the spatial distribution of these correlations could be predicted from a simple argument based upon geometrical optics [63].

The photons generated in the SPDC process are correlated in position and anti-correlated in momentum. Thus simultaneous measurements of signal and idler photons in a re-imaged plane of the crystal show strong correlations in position, whereas

if measured in the far-field of the crystal their positions, corresponding to their momenta, are anti-correlated [22]. Additional optical components or objects placed in either signal or idler beam change the strength or form of the correlations in a manner that can be calculated from the two-photon wavefunction, equation (1.9) [58, 64].

Klyshko recognised that the form of these correlations could be predicted by a classical analogue [63]. Rather than using two detectors, one detector is notionally replaced by a light source. Light emitted from this source and directed back towards the down-conversion crystal is in essence the time-reversal of the parametric emission. After transmission through any optical elements, this light is reflected from the down-conversion crystal towards the other detector, *i. e.* the crystal is replaced by a mirror. The detected intensity at this second detector is proportional to the anticipated fourth-order correlation when the experiment is run in down-conversion mode.

This classical configuration is analagous to the quantum system in many respects. For example, a converging or diverging pump beam at the down-conversion crystal corresponds to making the back reflecting mirror curved, changing the direction of the pump beam corresponds to tilting the mirror[34, 65–67]. Beyond the pump beam and back-reflecting mirror, the detailed nature of the detectors (area and numerical aperture) map directly onto the emission properties of the light source that is substituted.

2.4.1.2 Demonstration of the AWP

A demonstration of the Klyshko AWP is shown here by replacing the single-pixel detector in the heralded imaging system with a laser diode at 710 nm as shown in figure 2.6-b). This laser diode was coupled to the end of the multimode fibre and the light back-propagated through the heralding arm to the BBO crystal. A fraction of this back-propagated laser light was reflected at the crystal facet and redirected to the

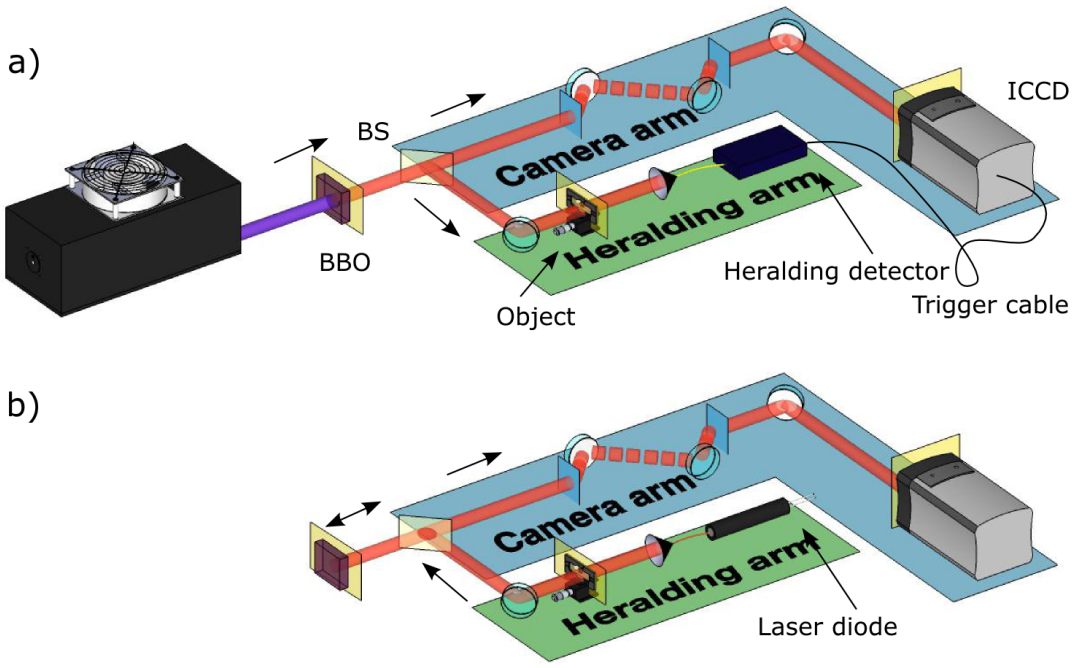

FIGURE 2.6: **A comparison between the heralded and advanced wave picture imaging configurations:** a) The experimental setup in the heralded imaging configuration. b) The experimental set up for a demonstration of Klyshko's AWP. The heralding detector was replaced by a laser diode which back-propagated through the object arm and used the BBO crystal as a mirror, before propagating through the camera arm and being detected by the camera.

camera arm, propagating through the delay line before being recorded on the ICCD. The overall transformation undergone by the back-propagated light from the object to the ICCD was given by an unity magnification imaging system with $M_{PC} = -M_{MC}$ for the position and momentum configurations respectively. The images recorded in the AWP configuration are shown in figure 2.7-b). The spatial distribution of the images taken in the back-propagated configuration match the corresponding heralded images.

The back-propagated beam couples into multiple guiding modes within the multi-mode fibre and the relative phase and polarisation of each mode is not preserved along propagation. Additionally, there is mode coupling between the different modes

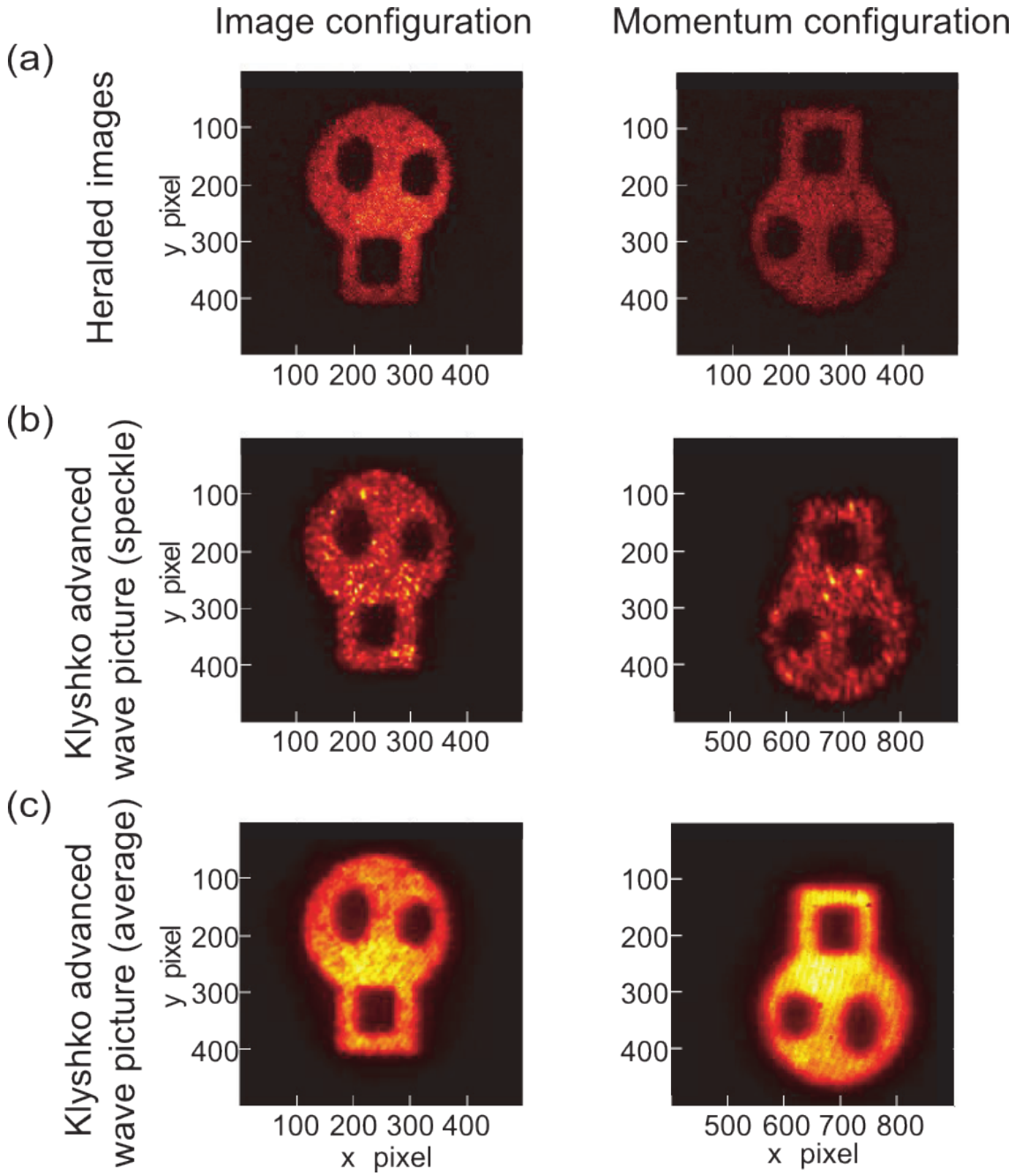

FIGURE 2.7: **AWP results:** (a) Heralded images obtained in the position and momentum configurations respectively. (b) Images obtained using the position and momentum configurations in the Klyshko AWP setup. The displacement of the momentum image is due to the inclination of the BBO-crystal and the speckle arises from mode-coupling in the multi-mode fibre. (c) Images using the position and momentum configurations in the Klyshko AWP whilst shaking the fibre to time average the speckle.

within the fibre. These effects give rise to a speckle pattern which is evident in the AWP images. Figure 2.7-c) shows AWP images taken whilst twisting the multi-mode fibre. In this case, the mechanical bending of the fibre throughout the acquisition changed the mode-coupling conditions within the fibre and thus degraded the spatial coherence of the illumination. This resulted in a time averaging of the speckle pattern and we obtained smooth images comparable to the heralded images taken with the down-converted light.

In order to work in the near-collinear phase matching regime discussed in section 1.3, we slightly tilted our BBO crystal relative to the pump beam normal. In the AWP, this tilt corresponded to the crystal acting as an inclined mirror to the back-propagated light, thus changing the mirror normal. In contrast, in the down-conversion configuration this tilt did not affect the effective mirror normal, which was set by the orientation of the pump beam. When imaging in the position configuration, the BBO crystal was in the image plane of both the source and camera in the AWP. Therefore, whilst changing the mirror normal resulted in the back-propagating light arriving at the camera at a different angle to the down-converted photons, it did not affect the spatial distribution of the image detected, as shown in figure 2.8-a). In this case the images recorded in the heralded and AWP configurations have the same intensity distribution and are registered at the same position on the camera, as shown in the left hand column of figure 2.7.

In the momentum configuration however, changing the mirror normal of the back-propagated light did result in a displacement of the back-propagated image, shown in figure 2.8-b). The measured offset of the far-field back-propagated image on the ICCD (figure 2.7-b) right image) due to the BBO crystal inclination was approximately 400 pixels or 5.2 mm. Using the effective focal length $f_e = 300$ mm of the Fourier system, we calculated the angle of the crystal in relation to the pump beam to be $\theta = 5.2$ mm$/f_e \approx 1^\circ$, which corresponded to the inclination angle measured with the rotation

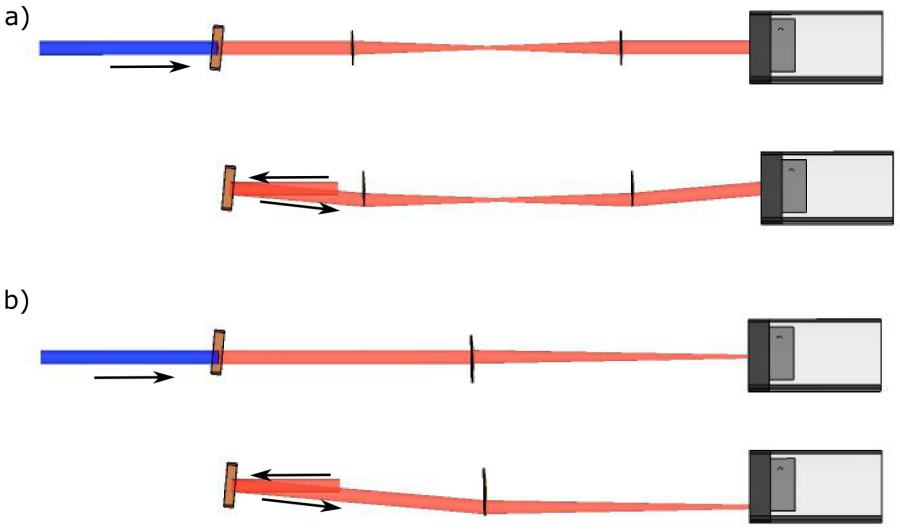

FIGURE 2.8: **Phase matching angles in the AWP:** The effect of the phase-matching inclination of the BBO crystal on the (a) beam propagation through the system when imaging the crystal and (b) the spatial location of the back-propagated image when in the far-field of the crystal. The angle of the crystal's inclination with respect to the optical axis is set by the orientation of the c-axis in the BBO crystal with respect to the facet normal and is a small angle of order one degree.

stage. A key advantage of using a camera to detect the full FOV is apparent in this context as it detects the image which would ordinarily be lost when using a scanning fibre.

Using a camera gave the ability to detect high resolution AWP images in both position and momentum configurations regardless of the BBO crystal orientation. This allowed the utilisation of the AWP for the alignment of coincidence-count experiments which had not previously been possible when using scanning fibre detectors [68].

2.4.2 The AWP and alignment

When aligning our system, we not only required that the beam pass through the middle of all optical elements in the optical path, but that the FOV of the single-pixel

detector overlapped with the center of the down-converted beam profile. This meant that the spatial distribution of the coincidence counts in both position and momentum configurations had to be centred around the same position. As shown above, when working in the position configuration, the image of the beam acquired on the camera using the AWP was exactly equivalent to that obtained in the heralded imaging configuration. However, the displacement of the beam obtained in the momentum configuration made full alignment using the AWP slightly harder.

There were several steps in the alignment process to ensure the entire system was fully aligned. We initially marked the path of the pump beam using pinholes before and ~ 1 m after the BBO crystal. We then forward propagated our alignment laser such that it overlapped exactly with the pump beam, and aligned the camera arm optics using the alignment laser.

With the camera arm aligned, we captured an image of the down-converted photons that were incident directly on the ICCD using the internal trigger mechanism of the camera. Backpropagating the alignment laser in the manner described in the AWP, allowed us to predict the full FOV of the correlated measurement on the camera. The fibre facet on the single-pixel detector was mounted in a translation stage with 6 degrees of freedom, allowing us to fine tune both the relative angle of the fibre facet to the coupling lens, and also the position of the coupling lens and fibre facet ensemble. In the AWP when adjusting the position of the ensemble, the position of the beam on the camera in the position configuration changed. Similarly, when we moved the angle of the fibre facet relative to the collection lens the position of the beam on the camera in the momentum configuration moved. We adjusted the position of the fibre facet and collection lens ensemble until this overlapped with the position of the directly imaged down-converted photons. We then adjusted the angle of the fibre facet with respect to the collection lens such that the back-propagated beam passed directly through the pinhole behind the crystal.

Repeating this process iteratively enabled the full alignment of the relay optics in both arms of the system, and the position and angle of the single-pixel detector. This ensured maximum detection efficiency of the down-converted fields at both detectors and therefore optimised the detection efficiency.

2.5 Image Acquisition

We used an ICCD camera to acquire our images. A great advantage when using an ICCD camera is the very high timing resolution, coupled with the ability to fire the intensifier of the camera conditional on an external trigger signal, as discussed in section 2.2.2. The combination of these two camera properties allowed the detection of only the desired photons on the camera, thus enabling the acquisition of very high-contrast images with a very low background. It was also possible to count the number of photons acquired in the image and thus calculate the energy deposition on the sample.

In this section I will describe how images were obtained and how the signal from the ICCD was interpreted and analysed. A more detailed discussion on image contrast and the various contributing signals to the camera readout signal follows in chapter 6.

During each acquisition by an ICCD, a charge is built up on each pixel regardless of any signal incident on the CCD chip, leading to a readout signal per pixel which is dependent on the exposure time and trigger rate but not any external factors. We characterised this signal by blocking the shutter of the camera and acquiring an image using the same trigger signal as for the data acquisition. This "dark image" was used to plot a histogram of signal output per pixel on the ICCD, as shown in figure 2.9-a). We used this histogram to determine a threshold, a signal over which was considered to be a real photon. For each threshold we could then calculate a noise probability

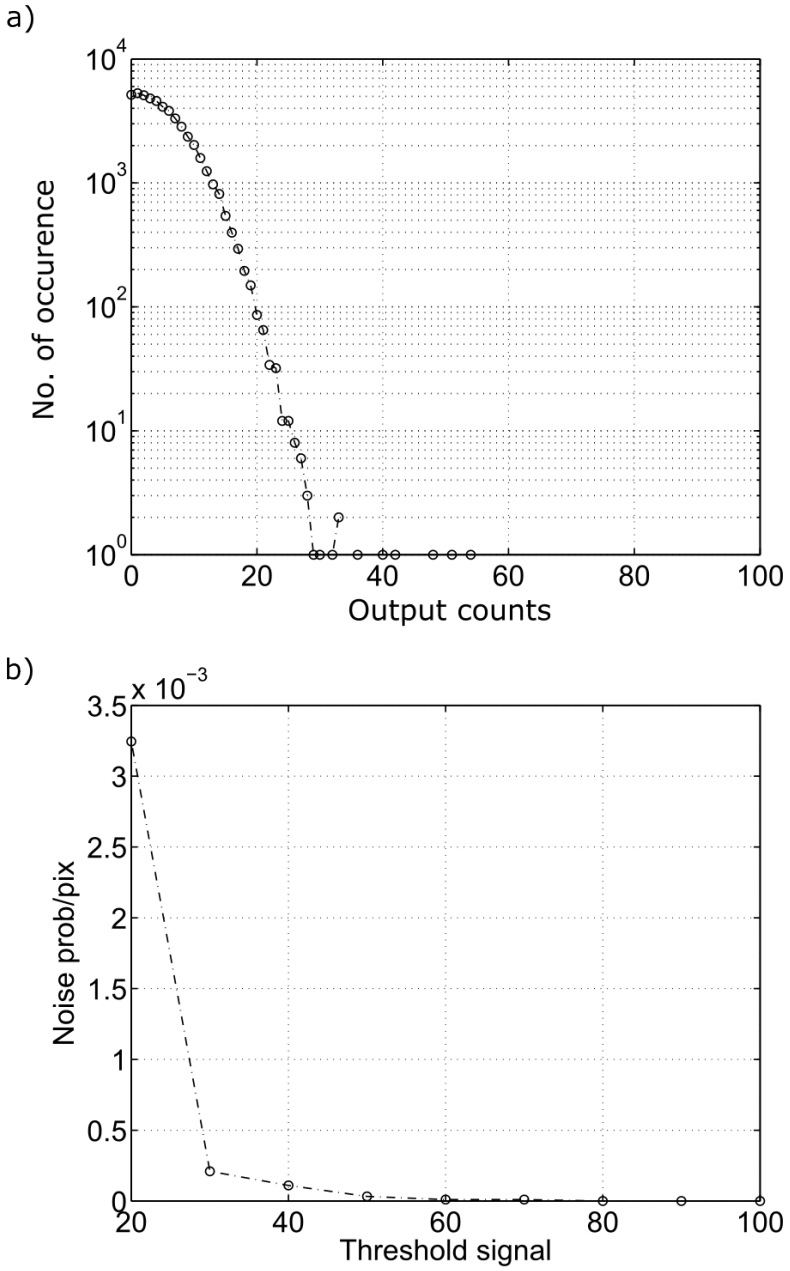

FIGURE 2.9: **Signal threshold on ICCD camera:** a) A histogram of the output counts from a "dark" image acquired on the ICCD camera. b) The noise probability per pixel based on a certain threshold.

per pixel, shown in figure 2.9-b), and thus calculate the expected number of noise events per image. There was a trade off between setting a very high threshold so as to avoid labelling spurious noise signals as real photons whilst ensuring that all real photons detected were labelled as such. We typically set the threshold such that the probability of a false reading per pixel, $\xi \approx 2 \times 10^{-4}$.

The duration of the exposure time per frame was set as a function of down-converted photon flux. As our photon counting methodology did not distinguish between one and many photon events per pixel per frame, we set the exposure time such that the probability of multiple photon detection per pixel within a single frame was very low. We determined this by acquiring triggered images of the beam for equivalent total acquisition times but with varying exposure times per frame. The exposure time for which the total number of photons in the final image began to decrease was the maximum exposure time for which we could be sure we detected only one photon per pixel. A sample graph and images showing the change in number of photons with exposure time for the trans-spectral imaging system described in chapter 5 is shown in figure 2.10. For the trans-spectral imaging system we typically used an exposure time of 0.1s, for the other experiments in this thesis we used an exposure time of 2 s.

2.6 Conclusion

I have described the key components in our optical setup, and how to build and align the heralded imaging system by making use of the AWP. The system and the techniques described here were developed and refined over 3 years of working with the system, and allow for the quick and efficient alignment of the imaging system and acquisition of images. Chapters 3, 4 and 5 describe imaging experiments conducted using this and similar systems, while chapter 6 provides a more detailed study of the aspects of the system that most affect the acquired image resolution and contrast, and how these can be optimised.

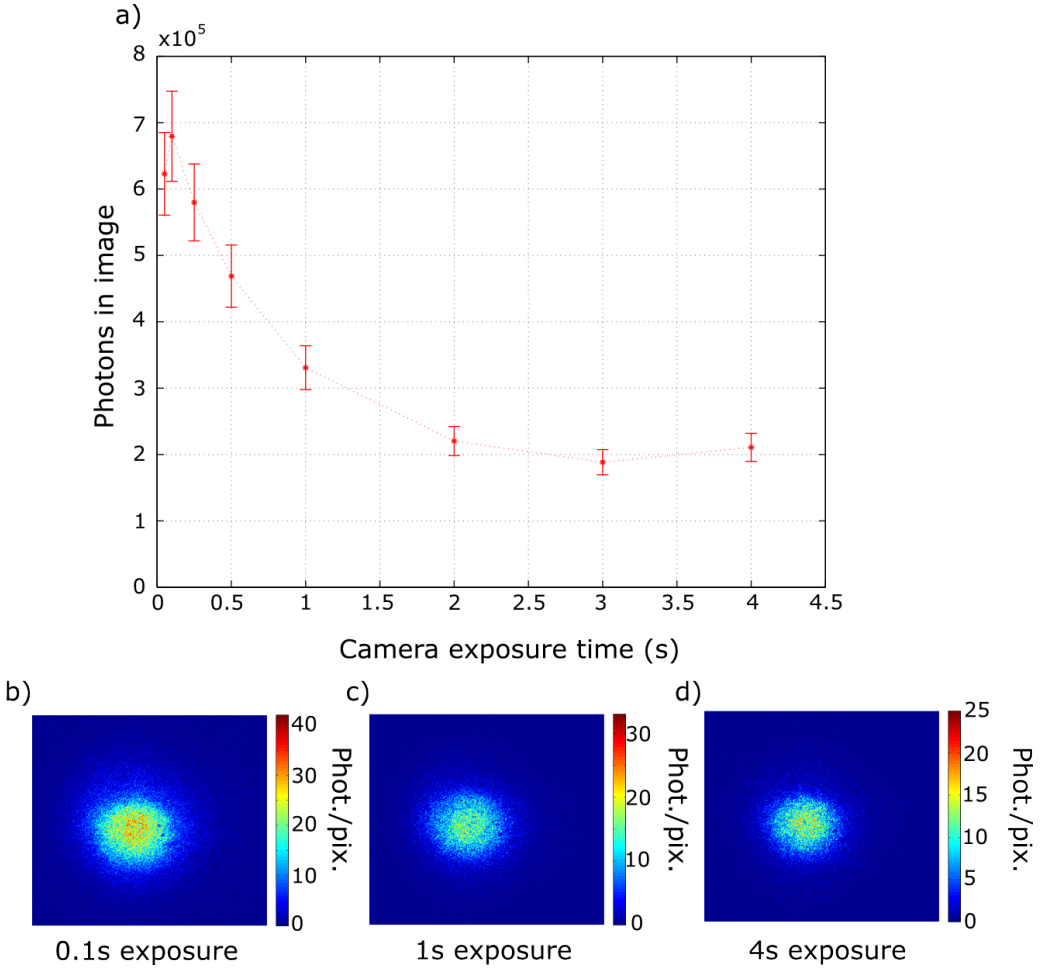

FIGURE 2.10: **Camera exposure times:** a) The number of photons in the triggered images of the beam for varying exposure times. b)-d) The acquired triggered images of the beam for varying exposure times. For exposure times of more than 0.1s we detect more than one photon per pixel and so our photon counting methodology discards many real photo-events and the total number of photons in the images decreases.

Chapter 3

EPR-enabled Imaging

3.1 Introduction

Quantum imaging is a term commonly used to describe imaging with single photons. However, a more rigorous definition of quantum imaging would require the utilisation of distinctly quantum properties of light within an imaging system. A hallmark of quantum entanglement is strong correlations between complementary variables, as discussed in section 1.2. When considering imaging, a natural set of complementary variables is position and momentum, measured by detecting the light field in the image plane or far-field of the source respectively. In this chapter, I shall present heralded images acquired using both position and momentum correlations between the photons generated in the SPDC process. This was the first experiment to utilise a camera within a heralded imaging system, and improved on the HE of a scanning system by 3 orders of magnitude. I will firstly discuss the source of the position and momentum correlations and present the high-resolution, high-contrast images of the object obtained using these correlations in both the image plane and far-field of the source - a utilisation of the EPR-type correlations of the source.

3.2 Image Plane and Far-field Imaging

To obtain in-focus heralded images, the ICCD camera and the object must be located in planes where the down-converted photons exhibit strong intensity correlations [23, 58]. Therefore, it is the location of the object and the camera relative to each other, rather than to the source, that is crucial for this experiment. This stipulation is particularly intuitive when one considers the system according to the AWP, discussed in section 2.4.1. The AWP describes a simple classical imaging system, and as such the position of the light source (the plane of the bucket detector) and the position of the mirror (the plane of the crystal) are irrelevant when considering the focus of the resultant images; what is critical is the relative position of the object and the camera. This condition was demonstrated for ghost imaging in the first such experiment, where Pittman *et al.* placed the object and detector in imaging planes of each other in the AWP, whilst not being in any specific plane of the crystal [43]. This experiment was followed by a similar one demonstrating interference and diffraction by placing the scanning detector in the far-field of the object according to the AWP [69].

Down-converted photons exhibit maximum intensity correlations in either the near-field or the far-field of the source, corresponding to position correlations and momentum anti-correlations. These intensity correlations can be described by the following derivation, following ref. [58].

Assuming a polarised, nearly monochromatic pump and down-converted beams, we use the description of the transverse wavefunction, Ψ, generated in the SPDC process shown previously in equation 1.10, $\Psi(\eta_1, \eta_2) = T(\eta_1 + \eta_2)\Gamma(\eta_1 - \eta_2)$, where $\eta_{1(2)}$ are the transverse coordinates at the SPDC source.

Assuming a Gaussian pump beam profile and approximating $\gamma(\boldsymbol{H})$ and T as Gaussians, the position-space wave function takes the form

$$\Psi(\boldsymbol{\eta}_1, \boldsymbol{\eta}_2) = \frac{1}{\pi\sigma_-\sigma_+}\exp\left[-\frac{|(\boldsymbol{\eta}_1+\boldsymbol{\eta}_2)|^2}{4\sigma_+^2}\right]\exp\left[-\frac{|(\boldsymbol{\eta}_1-\boldsymbol{\eta}_2)|^2}{4\sigma_-^2}\right], \tag{3.1}$$

where $\sigma_\pm$ are the standard deviations of two Gaussian functions that describe the strength of the position and momentum correlations respectively. Equation 3.1 has a Fourier transform given by

$$\Psi(\boldsymbol{H}_1, \boldsymbol{H}_2) = \frac{\sigma_+\sigma_-}{\pi}\exp\left[-\frac{\sigma_+^2}{4}|(\boldsymbol{H}_1+\boldsymbol{H}_2)|^2\right]\exp\left[-\frac{\sigma_-^2}{4}|(\boldsymbol{H}_1-\boldsymbol{H}_2)|^2\right]. \tag{3.2}$$

In the SPDC process, $\sigma_- \ll \sigma_+$, giving correlations in the near-field of the crystal (position) and anti-correlations in the far-field of the crystal (momentum).

In order to utilise the maximum intensity correlations described by equations (3.1) and (3.2), we placed both the camera and the object in either image or far-field planes of the crystal respectively. We switched between these two configurations through the use of an interchangeable lens system located between the BBO crystal and the beam splitter, as indicated in figure 3.1.

3.3 Experimental Methods

In order to perform image-plane and far-field imaging, we used the system shown in figure 3.1, which was very similar to that described in chapter 2. We pumped a 3 mm long BBO crystal with a Gaussian pump beam of waist 1.5 mm FWHM as a down-conversion source, and split the down-converted photons into the camera and heralding arm respectively using a pellicle BS. Between the BBO crystal and the BS we placed two sets of interchangeable lenses, thereby either imaging or Fourier transforming the down-converted field from the plane of the crystal onto the plane

of the BS. Changing the plane of the crystal relative to the BS also changed the plane of the camera and the object with respect to the crystal - allowing us to image either the image plane or far-field of the source. The interchangeable lens system set a relationship between the crystal and object/camera planes characterised by either an imaging system with a magnification of $M = 3$, or a Fourier system with an effective focal length of $f_e = 300$ mm. Crucially for this experiment, the object and the camera remained in the same plane relative to each other regardless of the lens configuration. The pump power was attenuated to ~ 2 mW, and we used a multi-mode fibre with a FOV that extended across the full scene as the input to our heralding detector. The Andor iStar Gen2 camera therefore received a trigger signal at a rate of approximately 15 kHz in the image plane configuration and 10 kHz in the far-field configuration. The camera was operated in direct triggering mode, described in section 2.2.2, with a gate width of 15 ns, equivalent to the width of the TTL output from the SPAD.

3.4 Image Acquisition

An image preserving delay line was necessary in the setup to ensure that the camera imaged the correlated twin of the photon detected at the bucket detector, as discussed in section 2.3.1. The theory of the heralded imaging system presented in section 1.5.1 has no explicit time dependence despite the timing discrepancy between the measurements made by the two detectors on the assumption that the delay line is tuned correctly so as to account for these delays. However, were this delay not optimised then the coincidence nature of the detections, and therefore the image, would be lost. It was possible to demonstrate experimentally the coincident nature of the image by detuning the electronic delay between the bucket detector and camera. This was done by changing the length of trigger cable between them. Figure 3.2

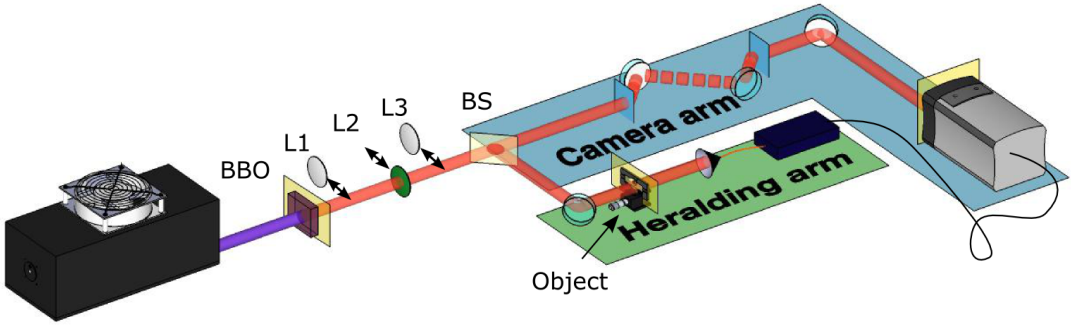

FIGURE 3.1: **EPR-enabled imaging experimental setup:** An interchangeable lens system was inserted between the BBO crystal and the beam splitter (BS). Lenses 1 and 3 imaged the down-converted source onto the plane of the BS, thus placing the object and ICCD camera in the far field of the source. Lens 2 Fourier transformed the down-converted photons onto the plane of the BS, such that the object and ICCD camera were both in an image plane of the BBO crystal. Importantly, the object and ICCD camera remained in the same plane of the crystal as each other regardless of the lens configuration.

shows a set of heralded images taken in both the position correlated and momentum anti-correlated configurations for several different values of the delay of the triggering pulse. As the timing of the triggering pulse was changed relative to the time of arrival of the correlated photon on the ICCD, the coincidence was lost and therefore no image was recorded.

In order to demonstrate the inversion of the image that occurs as a consequence of imaging using momentum anti-correlations, we acquired long single-exposure images of a transmission mask depicting a chain link. Rather than using the photon counting methodology described in section 2.5, we simply summed many long exposure frames on the CCD chip before reading out a single image. We therefore obtained an image of the recorded intensity distribution without subtracting camera readout noise or calculating the number of photons recorded in the images. We positioned the object

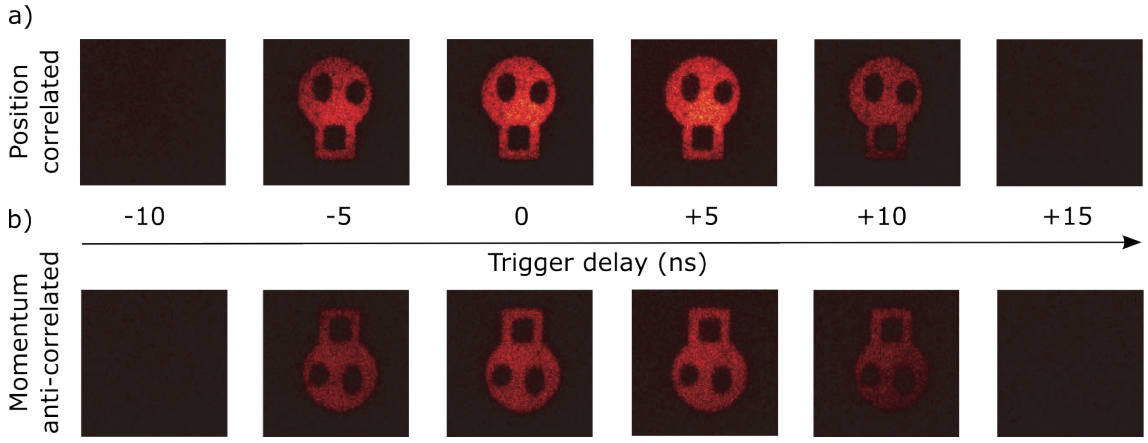

FIGURE 3.2: **Detuning the trigger window:** A demonstration of the coincidence nature of the heralded imaging system. When the timing of the trigger window was detuned by changing the length of the trigger cable, the coincidence image was lost in both a) position correlated and b) momentum anti-correlated configurations.

off-centre from the optical axis, such that when using momentum anti-correlations the image was inverted about the optical axis and so was recorded in a spatially distinct area of the CCD chip. The images obtained in the position and momentum configurations are shown in figure 3.3-a). We then switched the imaging configuration midway through the acquisition, thus obtaining an image of the intertwined links shown in figure 3.3-b). It is interesting to note again that when imaged in a single exposure in the AWP configuration the momentum is offset and thus, for the reasons described in section 2.4.1.2, the images do not intertwine, as shown in figure 3.3-c).

Within the 1024×1024 pixels on the CCD chip, we worked with a ROI of 500×500 pixels, equivalent to an area of 6.5×6.5 mm. Figures 3.4-a) and 3.4-b) show the optimum ghost images in the two configurations, both with a contrast in excess of 90%, where contrast is defined as

$$C = \frac{I_{max} - I_{min}}{I_{max} + I_{min}}. \tag{3.3}$$

All images were obtained by summing 1800 accumulations of 2 s duration. Using the

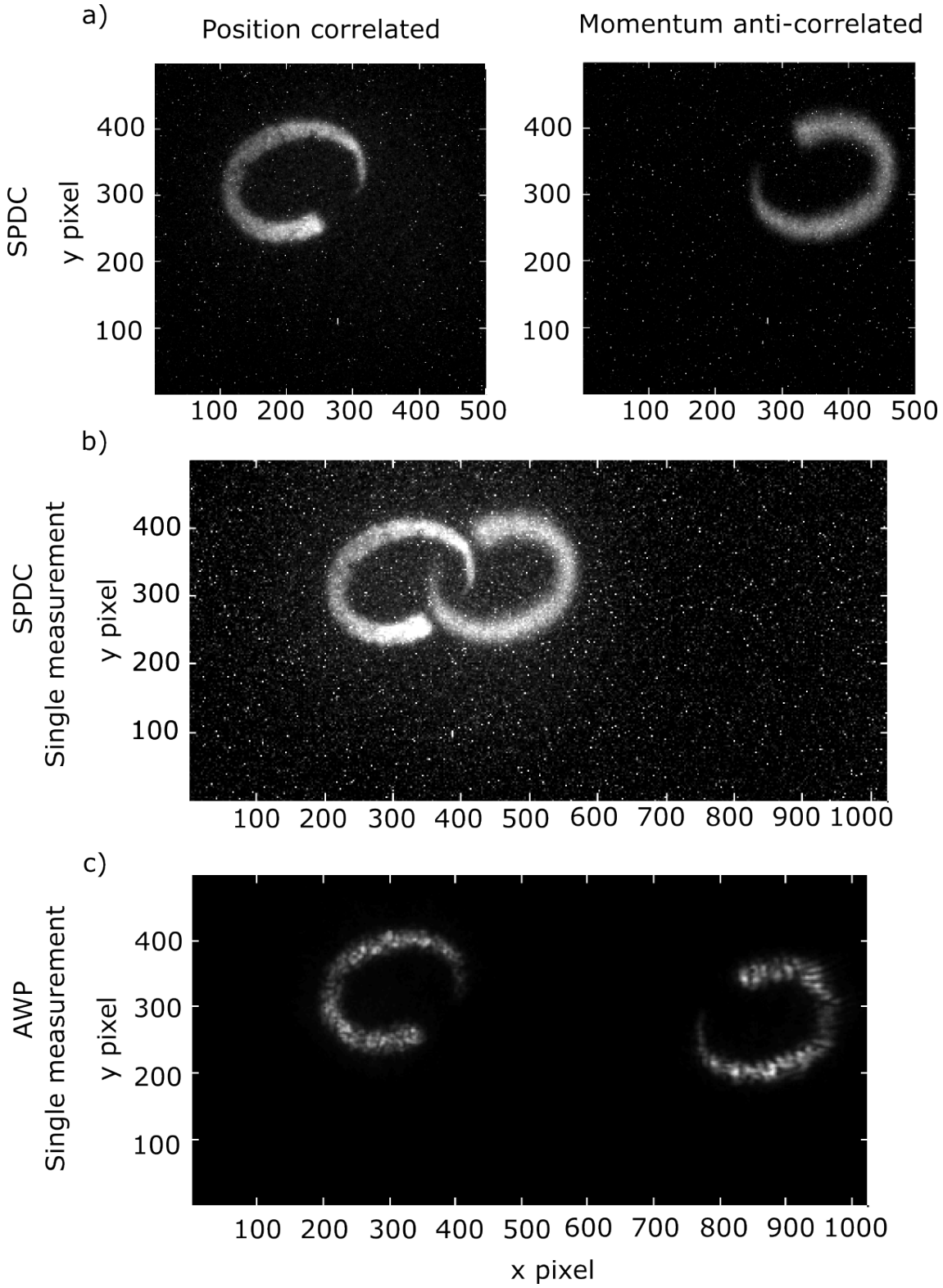

FIGURE 3.3: **Image inversion due to momentum anti-correlations:** The heralded images of a chain link positioned off-centre from the optical axis obtained in a) position correlated and momentum anti-correlated imaging configurations in separate exposures. b) Position correlated and momentum anti-correlated imaging configurations where the configuration was switched half-way through the acquisition. c) The same acquisiton as b) but in the Klyshko AWP configuration. In the heralded imaging system the image obtained using momentum anti-correlations is inverted relative to that acquired using position correlations and so the link is formed with the optical axis in the centre. In the AWP imaging configuration the image obtained using momentum anti-correlations is offset due to the inclination of the BBO crystal and so the link is not formed.

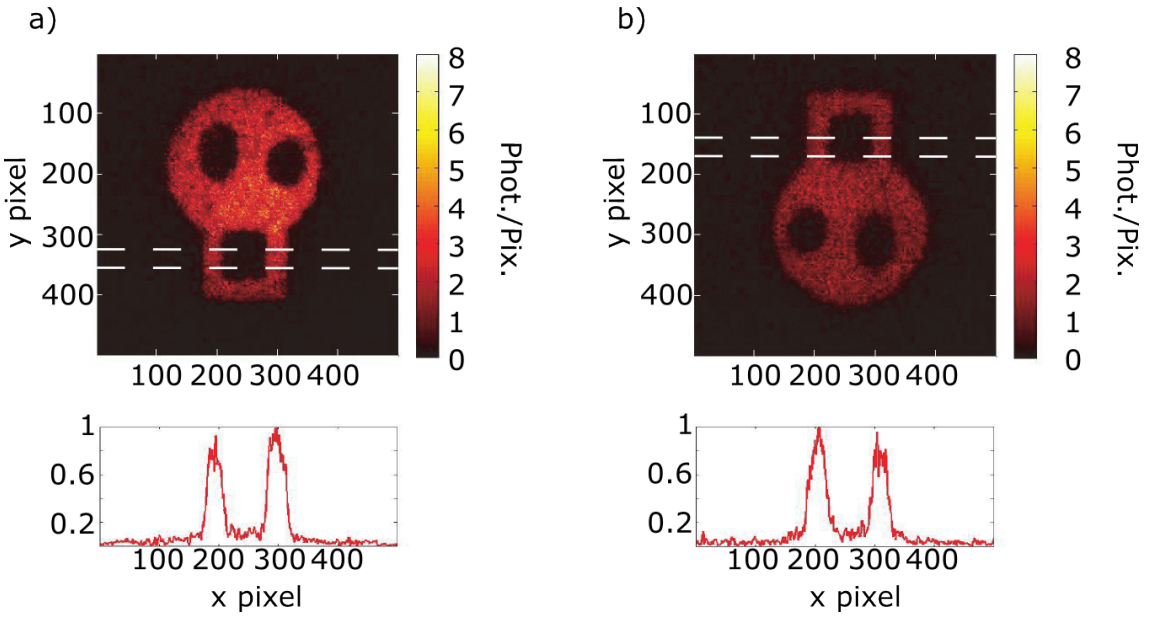

FIGURE 3.4: **EPR-enabled imaging results:** The heralded images obtained in a) position correlated and b) momentum anti-correlated imaging configurations. In both images the contrast is over 90 , with no background subtraction. The colorbar displays the number of photons detected per pixel in the image.

photon counting methodology described previously in section 2.5, the average number of detected photons per frame was approximately 70 in the position-correlated configuration and 40 in the momentum anti-correlated configuration. The intensity scale of the displayed images is the summed number of detected photons per pixel. Importantly, no background subtraction was applied to any of the images.

In the position-correlated configuration the image is upright, figure 3.4-a). In the momentum anti-correlated configuration the resulting image is inverted, figure 3.4-b). As the optical magnification in each arm is the same, the size of both images on the ICCD match the actual size of the object. The resolution of the two images is comparable and is set by a combination of the correlation length of the down-converted photons and the resolving power of our optical system. These factors will be discussed in chapter 6.

The ability to obtain high-resolution, background-free images in both the position correlated and momentum anti-correlated configurations is enabled by utilisation of

the EPR-like correlations in the spatial variables of the down-converted photons. By deconvolving the cross section of the transition shown by the dotted line in figure 3.4 with a Gaussian, I obtained point-spread-functions (PSF) for the system with $\sigma_x = 90$ µm in the position configuration and $\sigma_p = 80$ µm in the momentum configuration. These standard deviations are indicative of the strength of the position and the momentum correlations in the photon fields in the plane of the object and the resulting image. They relate to the standard deviations, Δx and Δp, of the down-converted field at the source by

$$\Delta x = \frac{1}{M}\sigma_x \tag{3.4}$$

$$\Delta p = \frac{\hbar k}{f_e}\sigma_p \tag{3.5}$$

where M is the magnification of the system from source to ICCD, f_e is the effective focal length of the Fourier system, k is the wavenumber of the photon. The variance product is therefore described by

$$\Delta^2 x \Delta^2 p = \frac{\hbar^2}{M^2}\frac{k^2}{f_e^2}\sigma_x\sigma_p\,. \tag{3.6}$$

Although not strictly equivalent to a conditional probability distribution across the whole field, the variance product is a good measure of the strength of the correlations. It should be noted that their variance product of $0.005\hbar^2$ is smaller than $\hbar^2/4$, indicative of the EPR nature of the source and quantum nature of this imaging system, as discussed in section 1.2.

The total number of photons detected in the images in figure 3.4 using our photon counting methodology was 1.26×10^5. This gave a HE of $\eta = 0.2\%$. The HE of the system is a function of the detection optics, thresholding methodology and dark

counts, which will be discussed in chapter 6. It is worth noting, however, that for a similar 500×500 pixel image obtained using a standard GI system with a scanning detector, the maximum HE would be $\eta = 1/N \approx 10^{-4}\%$.

3.5 Conclusion

This experiment was the first demonstration of a camera-enabled heralded imaging system [59]. The major advantage of full field-of-view detection, compared with a scanning system, is the dramatic increase in efficiency in the measurement of high-dimensional spatial entanglement. Recent works have demonstrated the potential of the multi-pixel detection of spatial entanglement [61, 70–74] and, albeit for multiple photons, quantum imaging [75]. However, the experiment described in this chapter was the first to combine multimode detection and single-photon sensitivity across an entire field of view, demonstrating an image-based utilisation of the EPR phenomenon. This suggests applications in low-light imaging systems and quantum information protocols [76–78].

The images obtained using this system were an improvement on previous imaging techniques, despite the fact that a relatively long acquisition time and a high photon flux at the sample were required. The next chapter will describe image processing techniques aimed at reducing both of these factors, bringing the heralded imaging system into a truly low-light imaging regime.

Chapter 4

Compressive Imaging

4.1 Introduction

Chapter 3 described an experiment which demonstrated the ability to acquire images of an object utilising both the position and momentum correlations of an SPDC source in a heralded, single-photon imaging system. When considering such an imaging system however, it is natural to ask the question: "What purpose does it serve?". Considering the long acquisition times for each image, the very low detection efficiency and the cost of building such a system, one could be forgiven for appreciating the science and then simply placing an efficient camera directly behind the sample and acquiring a conventional image.

One advantage of our heralded imaging system over a conventional camera is the ability to acquire images photon-by-photon on a negligible background, as shown by the images in figure 3.4. This characteristic, and the fact that a typical conventional camera captures approximately 10^{12} photons per image [12] again raises the question posed in section 1.1: "How many photons does it take to form an image?".

In this chapter, I shall seek to answer this question by using the heralded imaging system to investigate ultra-low photon flux imaging regimes. I shall do this by adapting the system presented previously to explore different imaging configurations and image processing techniques. I shall show that the configuration presented in the previous chapter is a useful configuration for considering low-photon imaging. I will also describe how to utilise the Poissonian statistics of our acquired data to reconstruct an image from significantly fewer photons than there are pixels in the image, and will apply these techniques to both binary and biological objects, presenting an image of a biological sample acquired with less than one photon per image pixel. I will then discuss image analysis criteria and place objective bounds on the subjective question of what constitutes an image.

4.2 Low-light imaging configurations

Chapter 3 investigated a heralded imaging system where the object and camera were in separate arms of the experiment. However, it is equally plausible to consider the system in a more simple configuration, where the object and camera are in the same arm as each other. In this chapter I shall compare three different imaging configurations referred to as the "Ghost imaging" (GI) configuration due to its similarity with the initial ghost imaging experiment [43], the "Triggered imaging" (TI) configuration, and the "Direct imaging" (DI) configuration.

The GI configuration is the same configuration as presented in chapter 3, where the object was placed in the heralding arm, and the camera was triggered externally by the signal from the heralding detector. Thus an image of the object was formed on the camera, despite none of the imaged photons having interacted with the object. For the TI configuration, the camera was again triggered by the external trigger pulse, but the object was placed in an intermediate imaging plane in the camera

arm. The camera was therefore triggered for each single photon detected by the heralding detector, yet the image consisted only of the correlated photons that passed through the object. For comparison, I also show DI, where the camera was triggered using its internal trigger mechanism. In this last configuration the image consisted only of the subset of photons that passed through the object and arrived at the camera during the camera trigger window by random chance. These three system configurations are illustrated in figure 4.1 and a more detailed description of the ICCD camera trigger mechanisms was presented previously in section 2.2.2. The experiment was performed using the same camera settings and methodology as the position configuration experiment described in section 3.4, while the intensifier trigger rate and gate width were the same for each imaging configuration. For this experiment we used an Andor Gen3 iStar camera, as described previously in section 2.2.2.

4.3 Comparing Imaging Configurations

The images shown in figure 4.2 were formed from the sum of 900 frames, each of 2 s exposure, during which time the camera intensifier fired for every trigger pulse received, either from the heralding detector or the internal trigger mechanism. We worked with a ROI of 600×600 pixels, covering an area of (7.8×7.8) mm^2 and used the photon counting methodology described in section 2.5.

As shown in figure 4.2, for both the GI and TI configurations we obtained a clear image of the test target with an image contrast of $\simeq 0.7$. By comparison, only a very faint image with a contrast of ~ 0.2 was obtained in the DI configuration. This reduced contrast for the DI configuration is a consequence of the independence of the repetition rate of the laser and the periodic nature of the intensifier trigger. Therefore, the arrival of the down-converted photon and the regular firing of the camera

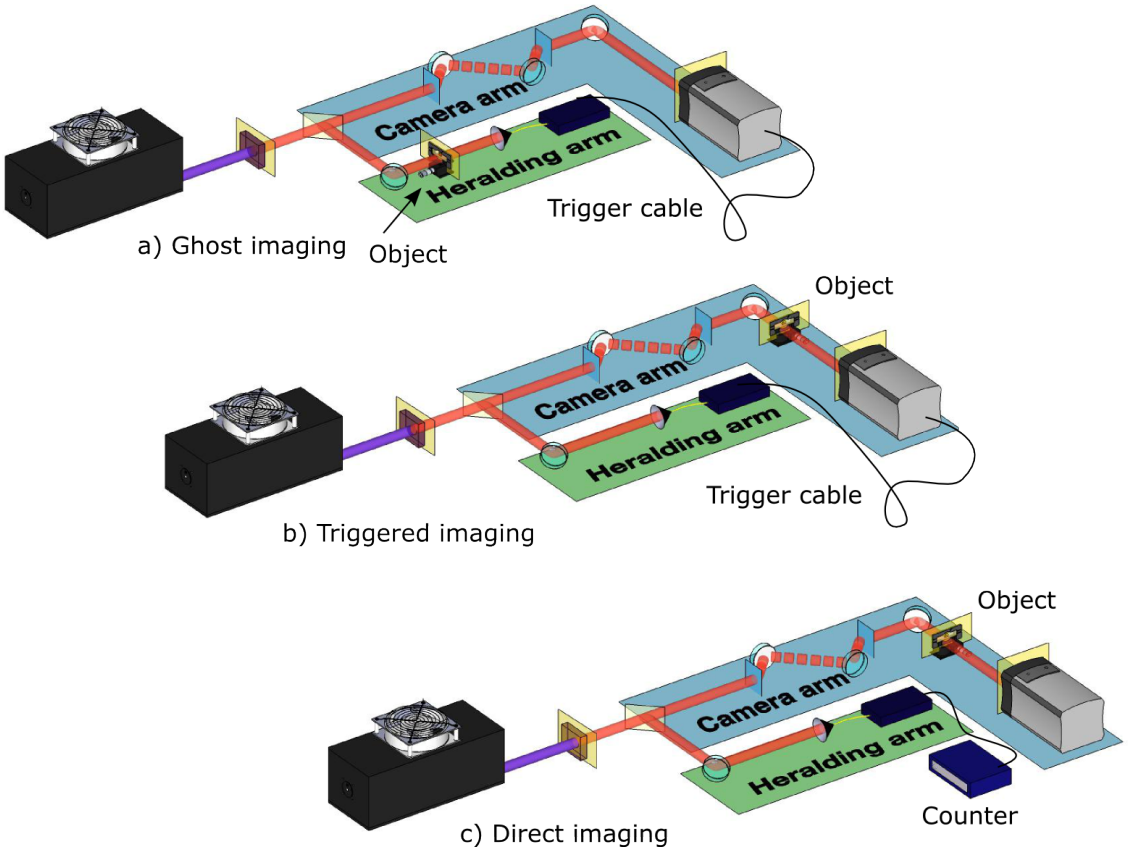

FIGURE 4.1: **A comparison of low-light imaging configurations:** a) Ghost imaging (GI) configuration as described in chapter 3. b) Triggered imaging (TI) configuration. The object is in the same arm as the camera and the intensifier of the ICCD is triggered by a signal from the heralding detector. The image is acquired by the detection of those correlated photons which passed through the object. c) Direct imaging (DI) configuration. The ICCD intensifier fires periodically and the image consists of those photons which passed through the object and arrived at the camera during one of these periodic windows.

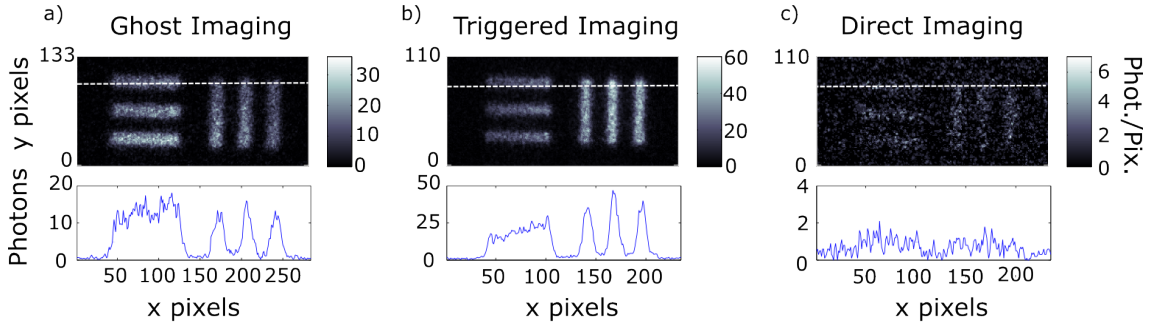

FIGURE 4.2: **Low-light imaging configuration results:** The images obtained for a) GI, b) TI and c) DI configurations. GI and TI give high contrast, high resolution images, whereas DI gives a very low contrast due to the only intermittent overlap of photon arrival time and intensifier trigger window.

intensifier window only occasionally coincided. This sporadic overlap of photon and detection window led to a very low detection efficiency.

Closer inspection of the GI and TI data reveals a slight difference in scale resulting from the magnification in the two arms not being quite the same. One also notes that although the total number of image photons is similar in the two cases, the GI configuration was obtained with fewer triggers of the intensifier than that of the TI configuration. This difference arose because although the photon pair generation rate in the two configurations was the same, when the partially transmitting object was placed in the heralding arm the trigger rate was reduced in proportion to the transmission of the object. For high flux rates the GI configuration may therefore prove to be advantageous since it places a lower technical demand upon the ICCD camera.

4.4 Compressive Sampling

Having compared possible low-light imaging configurations, I return to the question "What is the minimum number of photons that it takes to form an image?" A rough approximation would assume many photons per pixel (typically of the order of 10,000s photons/pixel for a conventional imaging system) are required, to ensure that the intensity of each pixel is not unduly subject to the Poissonian statistics associated with the quantisation of the number of detected photons [79]. It is, however, possible to store or even reconstruct an image using a much smaller data set than implied by this simplistic statement by using the techniques of compressive sampling.

The number of samples required to accurately reconstruct a signal was initially defined by Shannon [80]. For bandlimited signals, this corresponds to at least twice the maximum frequency, the Nyquist rate. For non-bandlimited signals such as images, the sampling rate is not explicitly dictated by the Shannon theorem, the

limiting factor in the sampling rate in this instance being the desired spatial resolution. Therefore, quantum imaging experiments utilising a scanning detector must scan each pixel individually and so are limited to a detection efficiency of $1/N$, where N is the number of pixels [17, 32, 43, 69]. However, despite this understandable and intuitive sampling limit, the theory of compressive sensing states that it is possible to reconstruct a signal using far fewer samples than traditionally required.

Typically, when imaging using raster scanning, to acquire a full image containing m pixels one must scan through all values of k (number of pixels) to $k = m$, but what if one only measures $k = n$ samples, where $n \ll m$? The reconstruction of the image would then require the solving of an underdetermined linear system of equations [81]. This has many possible solutions, but the concepts of compressive sampling can be used to distinguish the optimal solutions, and also inform how small n can be relative to m.

Key to compressive techniques is the concept of sparsity, the idea that when expressed in a carefully chosen basis, the desired signal has far fewer components than the bandwidth (or spatial sampling limit) would suggest [81–84]. If one expresses the signal in this desired basis one sees that most of the coefficients are very small and can thus be discarded. This enables the measurement of a signal using far fewer samples than initially expected. In the case of imaging, a natural basis to choose is the discrete cosine transform (DCT) basis. The DCT is the real part of the Fourier transform and describes the spatial frequency components of the image. The spatial frequencies present in an image describe the speed of variation between neighbouring pixels: low spatial frequencies describe very gradual changes across an image whereas high spatial frequencies indicate the presence of rapid changes between pixels. Real images, when expressed in the DCT basis are very sparse, as shown in figure 4.3. Therefore a solution to the linear system of equations that minimises the DCT is likely to be a good solution. Using compressive sampling techniques, one can both store data

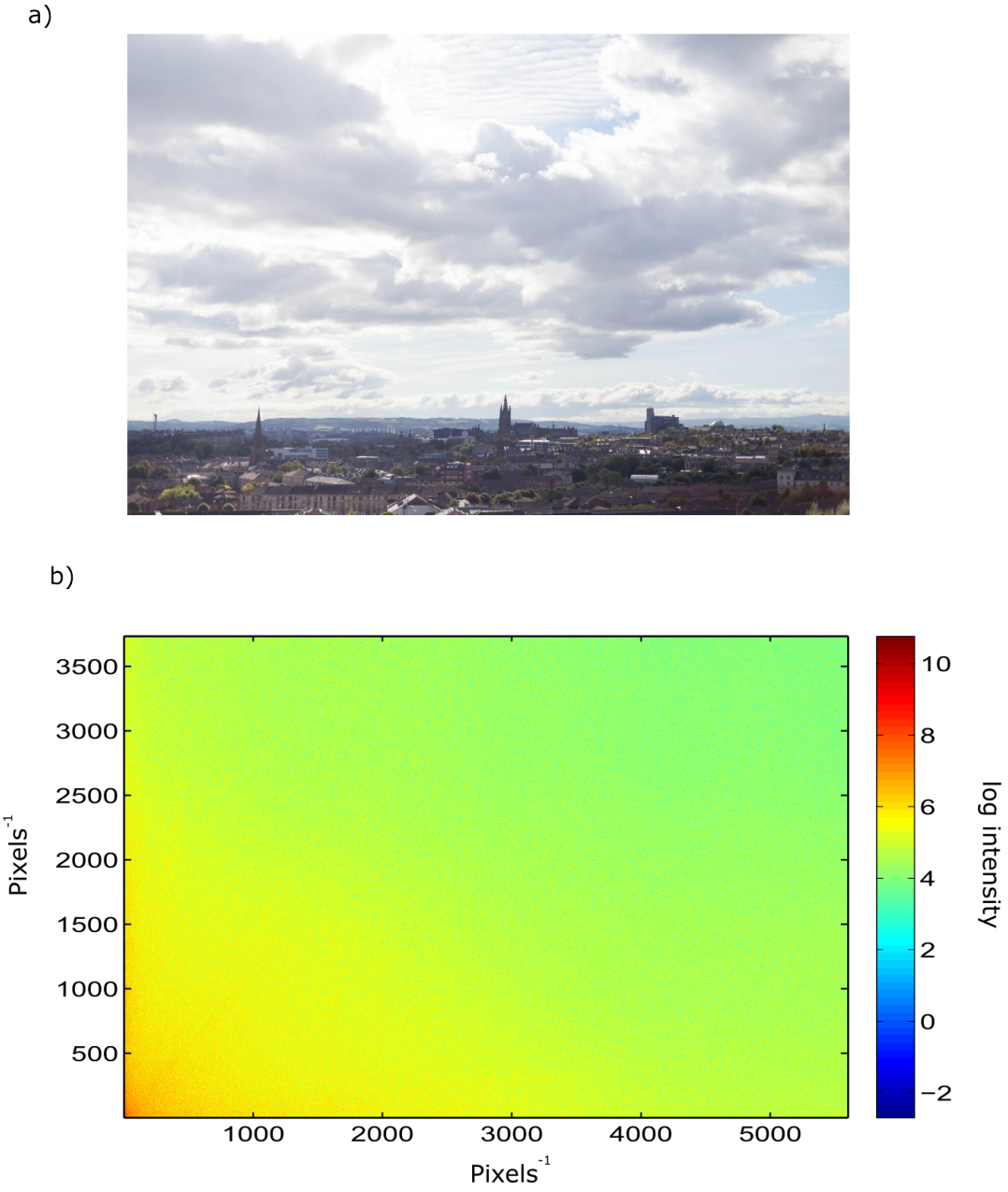

FIGURE 4.3: **Photograph and corresponding DCT:** a) Photograph of Glasgow skyline [1]. b) DCT of the photograph showing the spatial frequencies, where the log of the intensity in each spatial frequency is displayed. Very few spatial frequencies contribute significantly to the image, and these are centred around 0.

efficiently, as in JPEG compression, or by designing the sampling system effectively can significantly reduce the number of samples needed to effectively measure the desired signal [52, 85].

[1]Photo credit: Claire Aufhammer

4.5 Optimisation of the Reconstructed Image

Reconstruction techniques utilising compressive sampling techniques have been shown to enhance efficiency in applications requiring the exploration of a large state space, for example in quantum state tomography [85] and more recently in quantum imaging. This latter use of compressive techniques in a quantum imaging system allowed an image to be reconstructed using single-pixel detectors. Far fewer samples than required by the limit of the number of pixels within the image were acquired, albeit whilst still requiring many photons per pixel [5, 15].

Our heralded images, despite the long acquisition times, have a very small (typically $<$ 20) number of detected photons per pixel, and thus, even for a uniform transmittance region, the difference between neighbouring pixels in the acquired images show a large variation; a feature of the Poissonian statistics of the shot-noise. Therefore, despite a high signal to background ratio (SBR), our images have a low signal to noise ratio (SNR). The noise contributions in our images are, however, well-defined both in terms of the Poissonian characteristics of photon counting and a known probability of noise events, calculated using the photon counting methodology described in section 2.5.

As mentioned previously, real images are usually sparse in the spatial frequency domain, meaning they contain comparatively few significant spatial frequency components. We used the concepts of compressed sampling to utilise this sparsity to infer an image from fewer photons than necessary in standard imaging techniques. Here I will describe the process whereby the image data is modified to maximise the sparsity of the contributing spatial frequencies, whilst maintaining the likelihood of the resulting image within the bounds set by the Poissonian statistics of the original data.

We denote the measured number of photons for each of the N image pixels to be an integer, n_j, and the fractional intensity of each pixel of the modified image to be

I_j. Given an estimated dark count rate of ε per pixel, the Poissonian probability distribution of measuring n photons, given a pixel intensity of I, is

$$P(n_j; I_j) = \frac{(I_j + \varepsilon)^{n_j} e^{-(I_j+\varepsilon)}}{n_j!}\,. \tag{4.1}$$

We can therefore state the log likelihood, $\ln(\mathcal{L})$, of a modified image I_j, based on data n_j, to be [53]

$$\ln\left(\mathcal{L}(I_j; n_j)\right) = \sum_{j=1}^{N} n_j \ln(I_j + \varepsilon) - (I_j + \varepsilon) - \ln(n_j!). \tag{4.2}$$

Before any modifications, the intensity is equal to the measured values, $I_j = n_j$. However, we know that this data is subject to Poissonian noise, described by the square root of the measured number of photons. This well-defined noise allows us to modify the value of each pixel, provided it stays within the bounds set by this noise, giving a large range of statistically plausible alternative images. Within this range, we choose to select the image which has the sparsest discrete cosine transform (DCT). By defining the coefficients of the spatial frequencies of the whole image as a_i we can define a measure of sparsity through the number of participating spatial frequencies DCT_p as

$$DCT_p(I_j) = \frac{(\sum |a_i|)^2}{\sum |a_i|^2}. \tag{4.3}$$

The log likelihood and DCT_p are then combined as a merit function $\mathcal{M}$, defined as

$$\mathcal{M} = \ln\mathcal{L}(I_j, n_j) - \lambda \times DCT_p(I_j)\,, \tag{4.4}$$

where λ is a regularisation factor defined in order to set a balance between a solution that satisfies the recorded data and a solution that satisfies the sparsity condition. The intensity components of the image I_j are optimised based on an iterative maximisation of this merit function.

Each iteration of our optimisation routine makes a random change to the intensity value I_j of a pixel selected at random. The merit function is calculated for this modified image, and repeated iterations are performed until the image corresponding to a maximisation of this merit function is found. If λ is set to zero, the reconstructed image corresponds exactly to the data recorded, whereas if λ is set to a very high level, the reconstructed image corresponds to a uniform intensity distribution.

We used our imaging system in the GI configuration, as shown in figure 4.1-b), where the object, the USAF test target, was placed in the heralding arm of the system and the photons detected by the heralding detector were used to trigger the ICCD camera. We acquired images based on the accumulation of an increasing number of frames and hence of an increasing number of photons and optimised each image using varying values of λ. Due to the point spread function (PSF) of the intensifier in the ICCD and other factors discussed later in section 6.5.2, the observed resolution of the images was worse than the pixel size on the CCD. To better match the resolving power of our system to the pixel size in our reconstructed image and increase image processing speed, we downsampled our image by summing over adjacent pixels. The 600×600 pixels of the CCD were therefore processed as a 300×300 image.

The reconstructed images, shown in figure 4.4, highlight the effect of changing the value of λ and thus the balance between the solution that optimises the log likelihood of the reconstructed image and participation of spatial-frequencies within the merit function. As λ increases, the image becomes smoother due to increasing sparsity in the spatial frequency domain, but for high values of λ the resolution is degraded. Figure 4.4 shows the original data and images for a low-value, optimum-value and

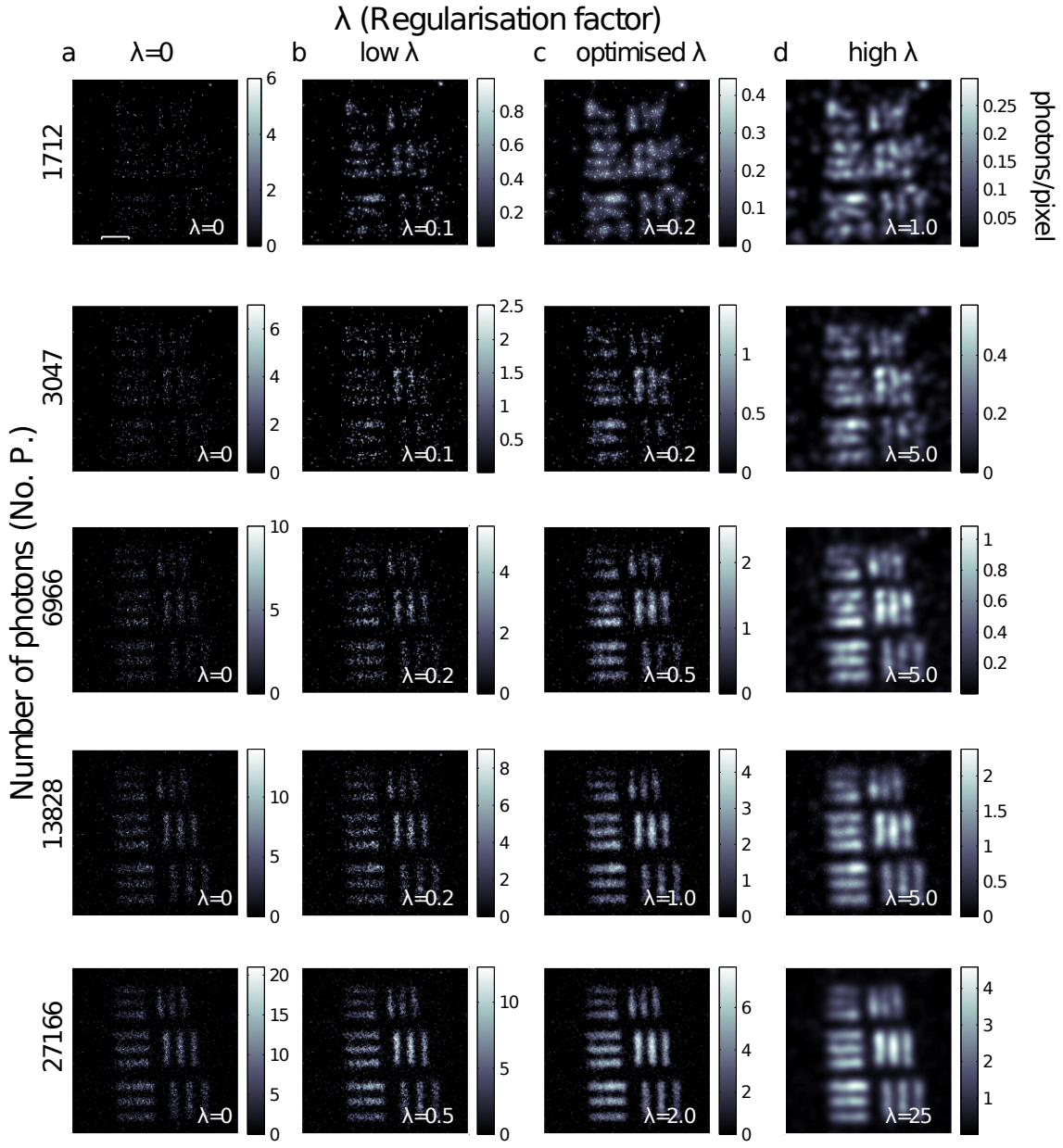

FIGURE 4.4: **Reconstructed images using an increasing number of photons and different regularisation factors:** The original data for an increasing number of photons is shown in the left hand column. The reconstructed figures for a low, optimised and high regularisation factor are shown in columns b)-d) respectively. With the correct choice of regularisation factor, one can reconstruct an image of the USAF test target using only 7000 photons. Scalebar=400 µm.

high-value of λ. The lower values of λ give images that retain the sparse characteristics of the original data, whereas the high values of λ give overly smooth images with associated loss of fine structure. The weighting factors for the central values of λ give subjectively the best images. We see that we are able to form a reconstructed image of the test target using an accumulated total of < 7000 photons, which corresponds to less than 0.2 photons per image pixel.

Having established that the system can be used in conjunction with a reconstruction technique to produce images from low numbers of photons we applied the system to the imaging of a biological sample, in our case the wing of a household wasp. The data from this wasp wing for both low and high photon number acquisitions along with their reconstructed images are shown in figure 4.5. The low photon number image comprises only 40419 detected photons over a field of view of 90,000 image pixels, corresponding to 0.45 photons per pixel. This image has a higher number of photons per pixel than the test target due to the greyscale nature of the object: whereas the test target was a binary object that had sharp edges, the wasp wing was semi-transparent leading to a greater transmission.

4.6 Image Analysis

This chapter has sought to answer the question "How many photons does it take to form an image?". Many images have been presented in order to answer this question, and the evaluation of the optimum image in a set has been performed based on the subjective analysis of a small number of image parameters. In this section I will briefly discuss these parameters and some of the subjective decisions necessary when evaluating images.

Recognising an object within an image of a scene is an active area of research [86–89]. There are arguably three distinctive characteristics an object must posess in order

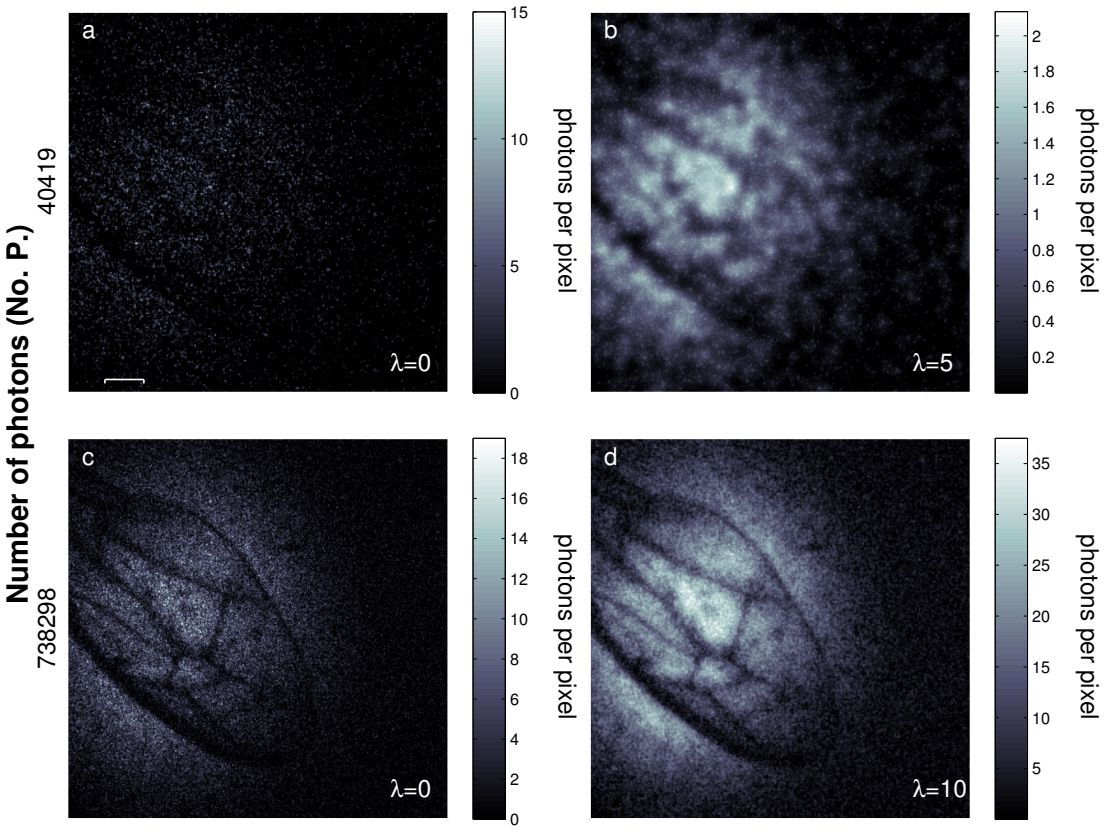

FIGURE 4.5: **Reconstructed wasp wing:** Raw data (left column) and reconstructed images (right column) of a wasp wing. Image b) shows the reconstruction of the wing using only 0.5 photons per image pixel. Scalebar=400 µm.

to be recognised as an object within a scene [88]: (a) a well-defined closed boundary in space; (b) a different appearance from its surroundings; (c) a saliencey that gives the object a degree of uniqueness within the image. Whilst these criteria are used to identify an object within a standard image, they can be adapated to illuminate our discussion of very low-light images, as presented in this thesis.

For the following discussion I will assume a binary object and an image containing very few photons such that the distribution obeys Poissonian statistics.

One method of image analysis that would detect an object fulfilling criteria a) and b) mentioned previously is to analyse the contrast across a cross-section of the image.

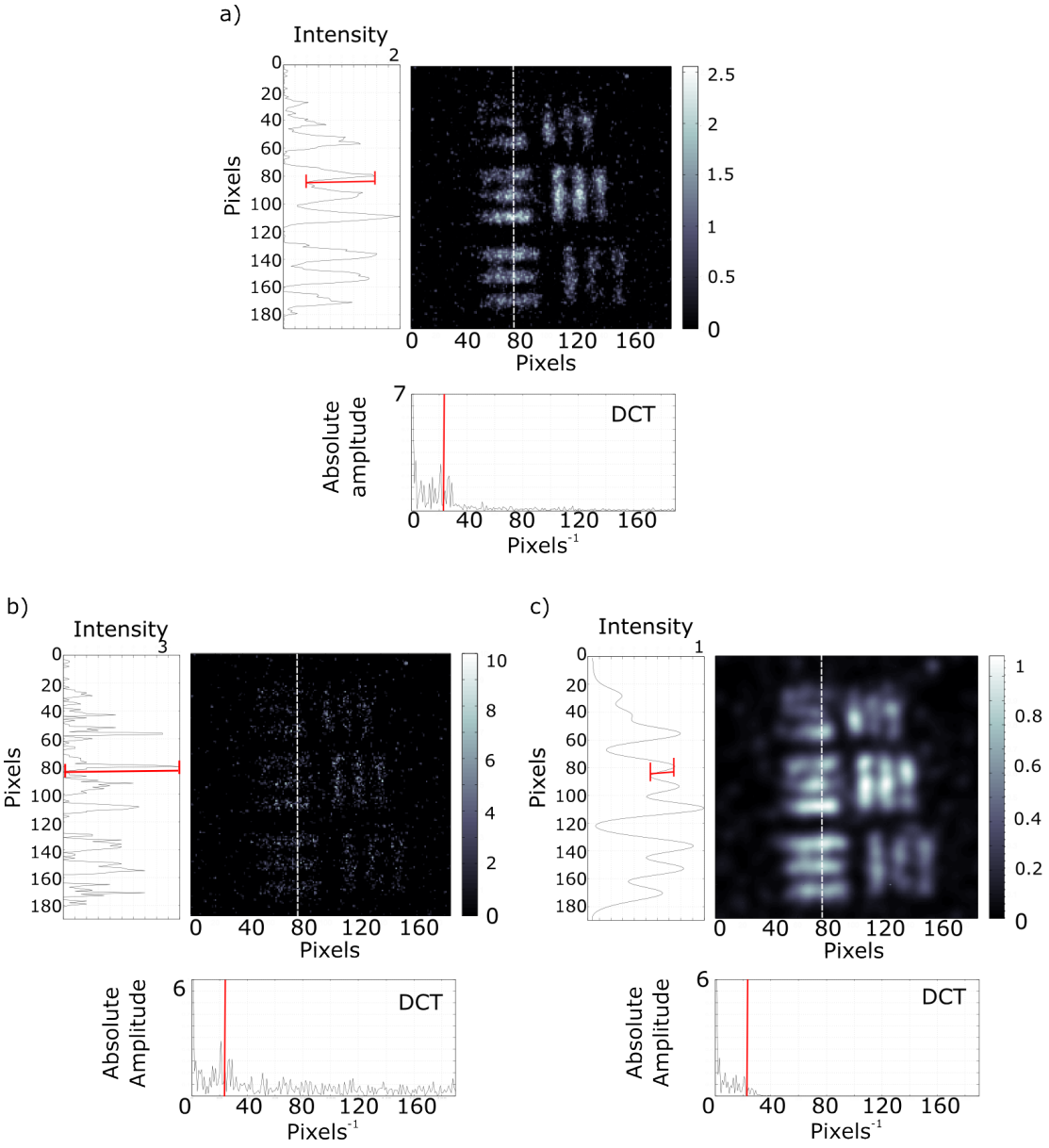

FIGURE 4.6: **Image analysis parameters:** Images of the test target with 6966 photons, as presented in figure 4.4. The vertical cross section is the average cross-section across the 5 columns indicated by the dotted line, and the transition analysed is marked in red. The DCT of the cross section is shown below the image, the red line indicates the spatial frequency of the PSF of the system. a) Optimised image. The contrast across the transition marked in red is 0.59 and 59% of the spatial frequencies in the image fall within the threshold set by the PSF. b) Original data. The contrast across the transition marked in red is 1 and 31% of the spatial frequencies in the image fall within the threshold set by the PSF. c) High λ optimised data. The contrast across the transition marked in red is 0.16 and 93% of the spatial frequencies in the image fall within the threshold set by the PSF.

Images of a binary object that fulfil these criteria will have a sharp transition between the object and the background. Whilst analysing this contrast may be sufficient to determine whether or not an object is present, it is not easy to objectively determine the quality of an image simply using this transition. The contrast required to determine when an object is present in an image is a subjective decision that is made depending on the situation; for instance, in standard imaging one would recognise an object in an image of a very foggy day with a much lower contrast than on a typical summers day. However, whilst an analysis of the contrast across a transition is a subjective measurement, it is possible to place bounds upon the measurement. In the low-light regime, the number of photons per pixel is subject to a Poissonian uncertainty of $\sqrt{D}$ photons per pixel, where D is the number of measured photons. It is therefore justifiable to assume that where the background falls within this measurement uncertainty leading to a contrast of less than $C = \frac{D-\sqrt{D}}{D+\sqrt{D}}$, this data set would not constitute an image of an object. Whilst this represents the fundamental limit, a more feasible limit for an optimum low-light binary image would be a transition contrast of approximately 50%.

When analysing criteria c) above, it is instructive to consider the spatial frequencies present within the image. As discussed in section 4.5, the noise associated with single photon counting gives rise to high spatial frequency noise in the acquired images. It is possible to threshold these spatial frequencies, working on the assumption that real images contain very few, predominantly low spatial frequency components. However, in a similar way to JPEG compression, the level of thresholding applied is a subjective measure dependent on the image and the amount of information required in the image. It is possible however to consider a minimum objective threshold. The PSF describes the minimum resolvable feature size of an imaging system, and has an associated spatial frequency. Therefore, it can be assumed that any real object information is contained in a data set that has spatial frequency components less

than or equal to this threshold. The extreme of this criteria would require all spatial frequencies to be smaller than the spatial frequency of the PSF. However this would only apply to an image with no shot noise and would therefore no longer be a low-light image. A more realistic bound would suggest that the image data should contain at least 50 % of spatial frequencies below the threshold of the PSF.

Figure 4.6 shows the optimised data for 3 of the images presented previously in figure 4.4. For each image, the contrast along a cross section of the image is analysed and the DCT of this cross section is analysed with respect to the threshold spatial frequency of the PSF. It is clear that when using a high value of regularising factor λ, 93 % of the spatial frequencies present in the image are below the PSF threshold, but the contrast across a transition is only 0.16. For the original data, there is a very high contrast of 1 across a transition but only 31% of spatial frequencies fall below the PSF threshold. For the optimised image, figure 4.6-a), the contrast across a transition is 0.59 and 59% of spatial frequencies fall below the PSF threshold.

Analysing the quality of an image is a subjective question that is dependent on many factors including the type of object being imaged, acquisition environment, and desired information content within the image. However, it is possibly to apply a measure of objectivity to the process by considering the contrast across a sharp transition within the image and the contributing spatial frequencies within the image.

4.7 Conclusion

For certain imaging applications, a low photon flux is essential; for instance in covert-imaging and biological-imaging where a high photon flux would have detrimental effects. In this chapter I have presented an image processing technique whereby we can utilise our heralded imaging system to acquire images using a very low number of photons. By characterising different imaging configurations, I have shown that the

GI imaging configuration is optimum for acquisition of low photon flux images with low readout noise from the camera and low technological demand on the camera. I then also described how one can exploit the natural sparsity in the spatial frequency domain of typical images and the Poissonian nature of the acquired data to apply image enhancement techniques that subjectively improve the quality of our images. I showed that it is possible to retrieve an image of a USAF test target using just 7000 detected photons. These image enhancement techniques, combined with the photon-counting, low-light imaging system, enable the reconstruction of images with a photon number of less than one photon per pixel. As an example of low intensity imaging of biological samples, I presented an image of a wasp wing, obtained using the time-gated ghost imaging configuration and consisting of an average photon-per-pixel ratio of 0.45. The use of compressive techniques to reconstruct images using very few samples is a burgeoning area of research [5, 15, 83, 90], although this was this first example of using these techniques to reconstruct a full-field image using very sparse data acquired by a camera [6].

Using these statisical techniques provides an answer to the question "How many photons does it take to form an image?". The precise answer to this question depends on how one determines what constitutes an image, and whilst this is inherently a subjective decision I have presented criteria based on contrast and spatial frequencies that provide an objective framework for image analysis. Within the context of these criteria, in this chapter I have presented an imaging system that allows the acquisition of images using far fewer photons than ordinarily assumed necessary.

However, whilst demonstrated using a heralded imaging system, it is clear that such techniques could also be applied to images acquired using high efficiency cameras, placed behind the sample in a conventional imaging setup at visible or near infrared wavelengths. The next chapter will further investigate practical applications of the heralded nature of this imaging system by describing an experiment which utilises

our heralded imaging system to acquire images from very few photons at wavelengths that are undetectable by standard cameras.

Chapter 5

Trans-spectral Imaging

5.1 Introduction

In the previous chapters I have described the development of a single-photon sensitive heralded imaging system, through which I have sought to answer the question "How many photons does it take to form an image". Thus far, the presented imaging system has used degenerate, 710 nm wavelength, photon-pairs generated through the SPDC process. This is useful for development and demonstration purposes, but the potential for application of such a system is limited due to ubiquitous low-light imaging systems in the visible and near IR wavelengths. However, low-light imaging at shortwave infrared (SWIR) wavelengths has many applications within both the technological and biological sectors. These applications span covert security systems, the imaging of light-sensitive biological samples and imaging within semiconductor samples/devices. However, given that the majority of single-photon sensitive, large-format detector arrays are silicon-based and therefore ineffective at wavelengths greater than 1 µm, the technological difficulties with such applications are readily apparent: crafting a camera with high quantum efficiency and low noise at infrared wavelengths is challenging and prohibitively expensive.

The SPDC process, whilst commonly used for degenerate photon pair generation, can produce correlated photon pairs where the signal and idler photons are at vastly different wavelengths. In this chapter I shall seek to answer the second question raised in section 1.1: "Is it possible to image a sample with a very small number of very low-energy photons?". In order to do so, I shall briefly discuss previous trans-spectral imaging systems, and then describe the heralded imaging experiment that we developed where the down-converted photons were at 460 nm and 1.55 µm respectively. I shall present images acquired for a range of exposure times and discuss the amount of energy deposited on the object during the imaging process.

5.2 Background

The ability to transfer image information between two disparate wavelengths is an interesting, if not entirely new area of research. There have been several different approaches to achieving this, including parametric upconversion, double SPDC interference systems and quantum GI.

Wavelength upconversion is a form of sum-frequency generation and is a second-order nonlinear interaction, acting in a similar manner to down-conversion [35]. In upconversion, a weak infrared signal is mixed with an intense beam in a non-linear crystal and is thus converted to a visible frequency. Demonstrations of upconversion were achieved as far back as the 1960's, although research into the technique was largely abandoned around a decade later as the QE of the process proved prohibitive to practical application [8, 91–93]. Recent years have, however, seen a resurgence in interest in upconversion, with demonstrations of high-resolution images obtained using upconversion and very efficient upconversion processes [94–97]. There is, however, a trade-off between efficiency and resolution in the upconversion process. In order to have a highly efficient upconversion process, long non-linear crystals are required.

However, the spatial bandwidth of the imaging system is inversely proportional to the length of the crystal, and so a longer crystal limits the resolution of the acquired images. These systems have therefore limited utility when wishing to obtain high resolution images with a very small number of infrared photons.

In 2014 an ingenious approach to imaging by transforming the wavelength between the illumination and recording light was demonstrated [36], based on induced coherence without induced emission [19]. In that work a combination of two separated SPDC sources was configured such that their infrared idler outputs overlapped and could no longer be distinguished. The object was placed in the idler path between the SPDC sources while an interferometer was formed using the two corresponding visible signal outputs from the SPDC sources. Whenever the object introduced absorption in the idler, the source of the idler became distinguishable and the interference between the signal beams changed such that a visible image was formed at the interferometer output. However, the photon flux in such a system needed to be maintained at a modest level such that the image was detectable with a low-light camera.

Traditional quantum GI systems using a non-degenerate SPDC source have also been proposed. In these systems the object is probed with an IR photon and a scanning fibre detects the correlated visible photon. As in standard GI systems, the image information is contained in the coincidence measurements between the two detections [98–100]. This has been demonstrated for a probe photon at 1550 nm and correlated photon at 810 nm [37]. However, as with the standard GI system, the reliance on a scanning detector limits the detection efficiency to a maximum of $1/N$, thus also limiting the practicality of such a system.

We used the same heralded imaging system described previously in this thesis, but replaced our source with a non-degenerate SPDC source, producing correlated photons at 460 nm and 1.55 µm. The combination of the full FOV heralded imaging

system and illumination of the sample with very low numbers of infrared photons allowed for the acquisition of an image with very few low-energy photons. Thus the imaging system presented in this chapter is the first trans-wavelength imaging system that has the potential to acquire images with a very small energy deposition in the sample. This provides a positive answer to the question raised at the beginning of this thesis, and restated at the beginning of this chapter: "Is it possible to image a sample with a very small number of very low-energy photons?"

5.3 Experimental Setup

The heralded imaging system used for trans-spectral imaging, shown in figure 5.1, shares many important characteristics with the system described in section 2. However, within this framework the differing wavelengths necessitated various changes, which I shall describe here.

The 50/50 beam splitter was replaced by a cold mirror, a dichroic mirror that reflects incident light at $\lambda \lessapprox 700$ nm and transmits longer wavelengths, with $\approx 95\%$ reflection at 460 nm and $\approx 90\%$ transmission at 1.55 μm. There are two main types of single-pixel detectors at SWIR wavelengths, as described previously in section 2.2.3 - InGaAs/InP SPAD's or SNSPD's. The images shown in this chapter were acquired using the InGaAs/InP SPAD, but the system was designed such that both detectors could be used interchangeably, and a comparison between the detector types and corresponding acquired images will be presented in section 6.7.1.

In the experiment described in chapter 2, both the camera and heralding arms of the system had a magnification of M=3. However, in order to couple the maximum possible signal into the smaller aperture of the heralding detector in this non-degenerate system, we changed the magnification in both arms of the system such that the magnification from the BBO crystal to the sample was $M_{cs} = -1/2$, from the sample

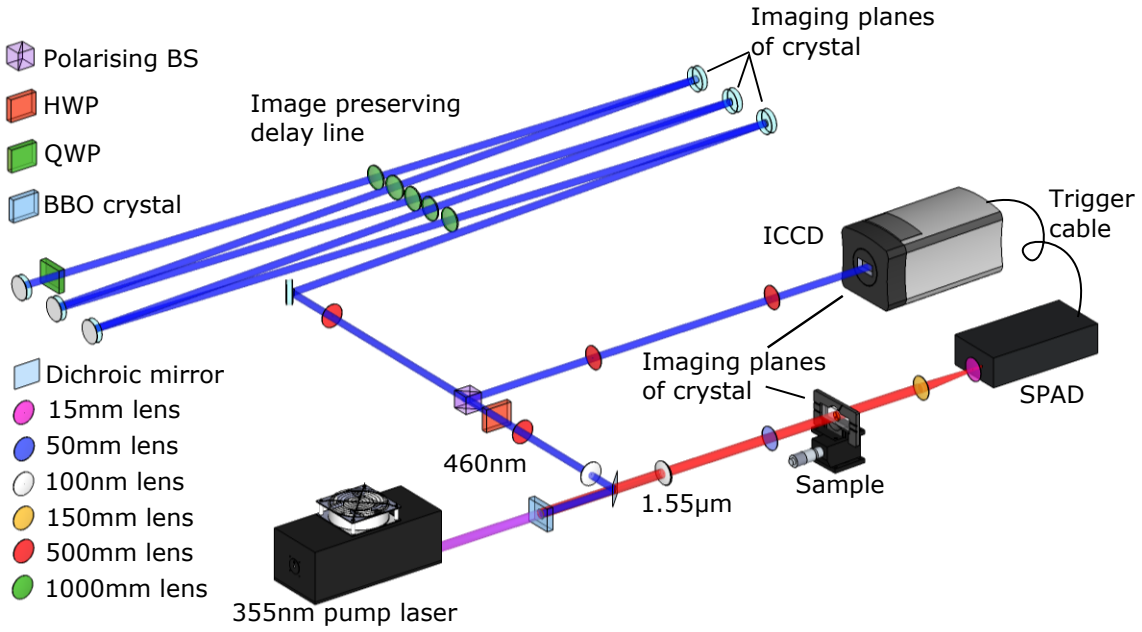

FIGURE 5.1: **Full experimental setup for trans-spectral imaging:** The 460 nm and 1.55 µm photons were split at a cold mirror. The IR photons probed the sample, with the transmitted photons detected by the InGaAs/InP SPAD. The visible photons passed through a 25.2 m delay line before being detected by the ICCD.

to the detector was $M_{sd} = -1/10$, and from the crystal to the ICCD was $M_{cc} = 5$, giving a total magnification from the sample to the ICCD of $M = -10$. This enabled the imaging of samples on microscopic length scales.

The electronic delay associated with the IR detectors was longer than that from the SPAD used in the degenerate system. To compensate for this we extended the delay line in the system from the 22 m used in the degenerate system to 25.2 m. This was predominantly achieved by increasing the number of telescopic imaging systems within the double-pass telescopic imaging line from 4 to 5, as shown in figure 5.1, the full experimental system for this chapter.

5.4 Image Acquisition

To illustrate the trans-spectral capabilities of our system we used two samples formed from a polished silicon wafer onto which was written a microscopic gold test pattern (created by electron beam lithography, electron beam deposition and lift off at the James Watt Nanofabrication Centre by Robert Kirkwood), shown in figure 5.2. The refractive index of silicon is ≈ 3.5 [101], which is significant when considering the signal detected by the heralding detector. The reflection at a refractive index step change is described by

$$R = \left| \frac{n_1 - n_2}{n_1 + n_2} \right|^2 ,$$

where $n_{1(2)}$ is the refractive index of the material on each side of the boundary. At each boundary between air ($n \approx 1$) and silicon therefore $\sim 30\%$ of the light is reflected, giving an overall transmission through the silicon of $\sim 50\%$. This loss due to reflection can be minimised with the application of an anti-reflection (AR) coating. By way of comparison, we had the chip in figure 5.2-b) AR coated for 1.55 µm, while the chip in figure 5.2-a) was uncoated.

The Greek letters on the chip have a height of 120 µm surrounded by a framing box of width 160 µm. This is within the 250 µm FOV of the heralding detector. At 1.55 µm the silicon is transparent whereas the gold is not. This means that any residual $\lambda \sim 460$ nm signal photons that are in the idler path will be fully absorbed by the silicon substrate and therefore cannot trigger the heralding detector. In a similar fashion, any $\lambda \sim 1.55$ µm light in the signal path will not be detectable by the ICCD camera as it lies outwith the detection bandwidth of the photocathode of the intensifier.

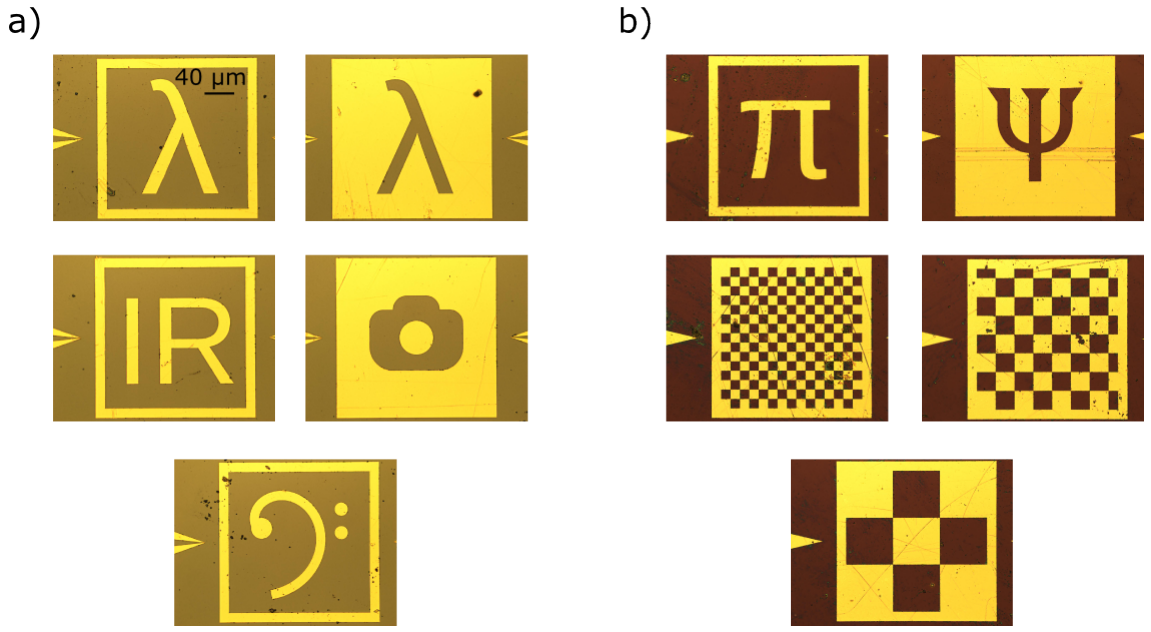

FIGURE 5.2: **Microscope images of gold deposited silicon wafers:** The yellow colour is gold, deposited onto a polished silicon wafer. The length of the boundary square is 160 µm. Chip a) was uncoated and chip b) was anti-reflection coated for 1.55 µm.

The ICCD camera was operated in external trigger mode as described in section 2.2.2, with an intensifier gate width of 10 ns. The exposure time per frame was 0.1 s and the pump laser was attenuated such that the trigger rate from the SPAD was $\approx$ 10 kHz. The SPAD was run using the settings described in section 2.2.3.

5.5 Results

In order to determine the minimum number of photons, and corresponding minimum exposure time, required to acquire an image using the trans-spectral imaging system, we summed an increasing number of frames acquired using our photon counting methodology, as outlined in section 2.5. Figure 5.3, shows the resulting images for exposure times of between 30 s and 10 minutes. It is clear that an image starts to appear after just 8500 detected photons, whilst the clarity of the image improves

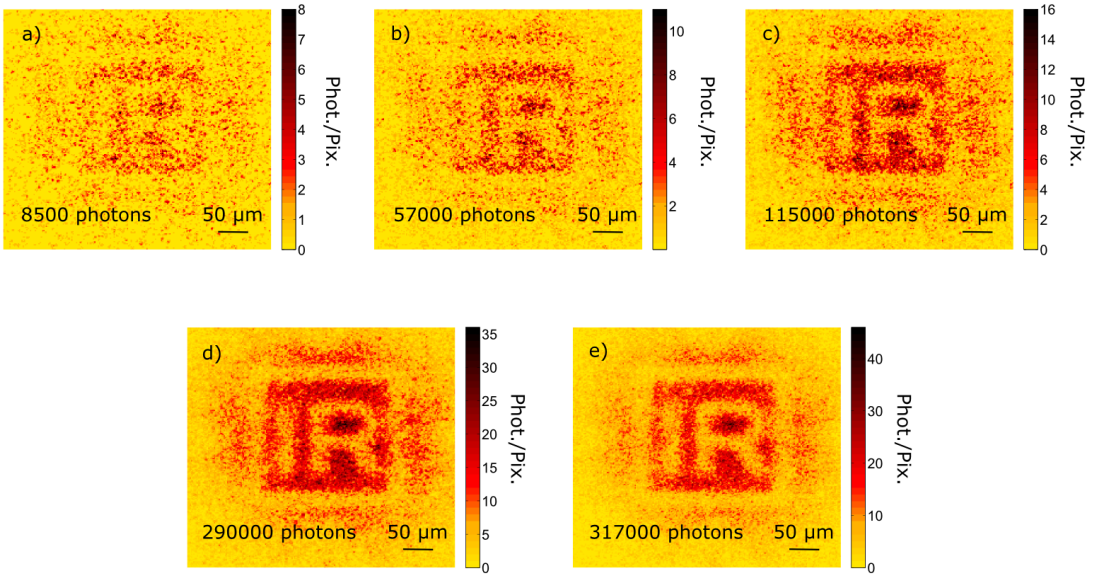

FIGURE 5.3: **Image of the letters IR with an increasing number of photons:** An image of the letters IR, shown in figure 5.2, for an increasing number of photons. The images were acquired for, from a)-e) respectively, 30 s, 60 s, 120 s, 300 s and 600 s.

with time as the higher number of photons detected in the image mitigates shot noise effects.

The spatial resolution of our system was calculated by imaging the squares shown in 5.2, with side lengths of 10 µm, 20 µm and 50 µm respectively. The acquired images are shown in figure 5.4. The deconvolution of the sharp transition between the gold and silicon squares with a step function results in a PSF with a 2σ width of 18 µm at the plane of the object. This is illustrated by figures 5.4-b) and c), where the 20 µm squares are faintly visible above a high background and there are no distinguishable features in the image of the 10 µm squares.

The high noise in the short exposure images resulting from the discrete counting of photons makes rigorous analysis of such images challenging. To overcome this we acquired a long, 30 min, exposure of the silicon λ and gold IR depicted in figure 5.2. These images and cross-sections, shown in figure 5.5, were used to calculate the contrast of the acquired trans-spectral heralded images. Using the definition

of contrast in equation (3.3), the contrast of the images was determined to $\sim 70\%$, where the maximum and minimum intensities were measured along the cross-sections shown.

As mentioned previously, the change in refractive index at the boundary of the object results in only 50 % transmission of the IR photons. In order to compare the effect this loss of signal has on the acquired heralded images, we acquired 5 min exposure images of an uncoated gold bass clef symbol and silicon camera symbol, and an AR coated gold π and silicon Ψ, shown in figure 5.6. It can be seen that there is very little difference in contrast between the images of the AR coated and uncoated objects. The trigger rates from the heralding detector for the AR coated and uncoated objects were 10000 Hz and 8000 Hz respectively, and there is a corresponding slight increase in the total number of photons in the image of the AR coated object. The difference is, however, not unduly noteworthy, due predominantly to the difference in transmission area of each object.

In all the analysis of the images presented thus far in this thesis, I have considered the number of photons in the acquired image. However, when considering low-light imaging, the number of photons detected by the camera is not the most pressing consideration. Rather, the important characteristic is the number of photons incident on the sample in the duration of the acquisition. I calculated this by measuring the number of photons detected by the heralding detector with no object present. Given the detection efficiency of this heralding detector, I inferred the number of infrared photons at the plane of the sample within the boundary box of the object to be 2×10^5 per second. This photon flux corresponded to an illumination power of 25 fW, and an energy deposition on the sample of approximately 40 pJ cm^{-2} s^{-1}. The images in figure 5.7 were acquired for 30 s, 2 mins and 10 mins respectively, and thus the total energy deposition on the sample within the boundary box was 800 fJ, 3 pJ and 15 pJ respectively. There is an obvious trade-off between a long exposure

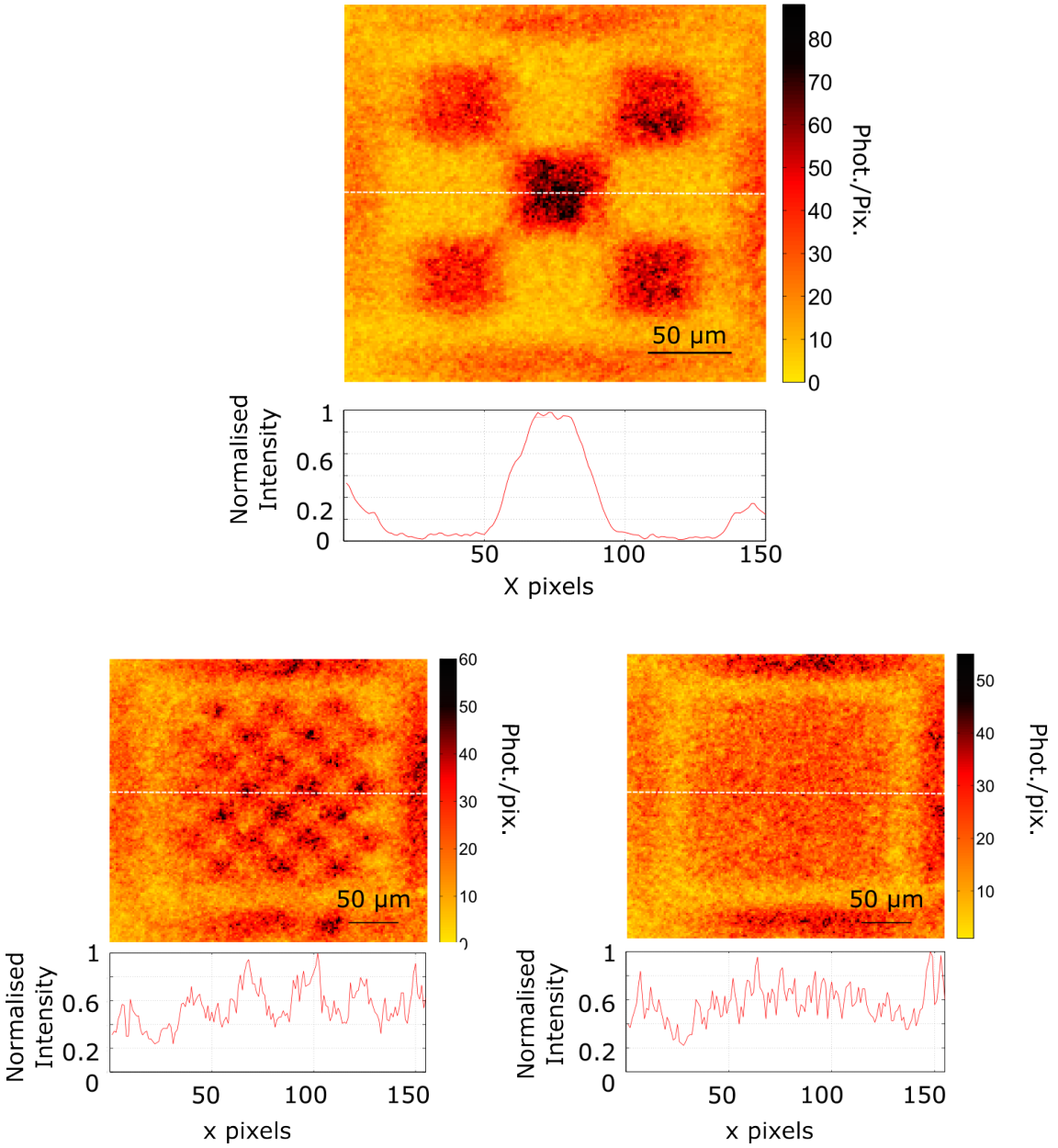

FIGURE 5.4: **Resolution test:** Squares of size 50 µm, 20 µm and 10 µm with associated cross sections. The spatial resolution of the system was calculated by deconvolving the transition in the cross section of the image of the 50 µm with a step function. The PSF of 18 µm (2σ) is highlighted by the low visibility 20 µm squares and indistinguishable 10 µm squares. The cross-sections are an average of the 5 rows surrounding the white dotted line in the image.

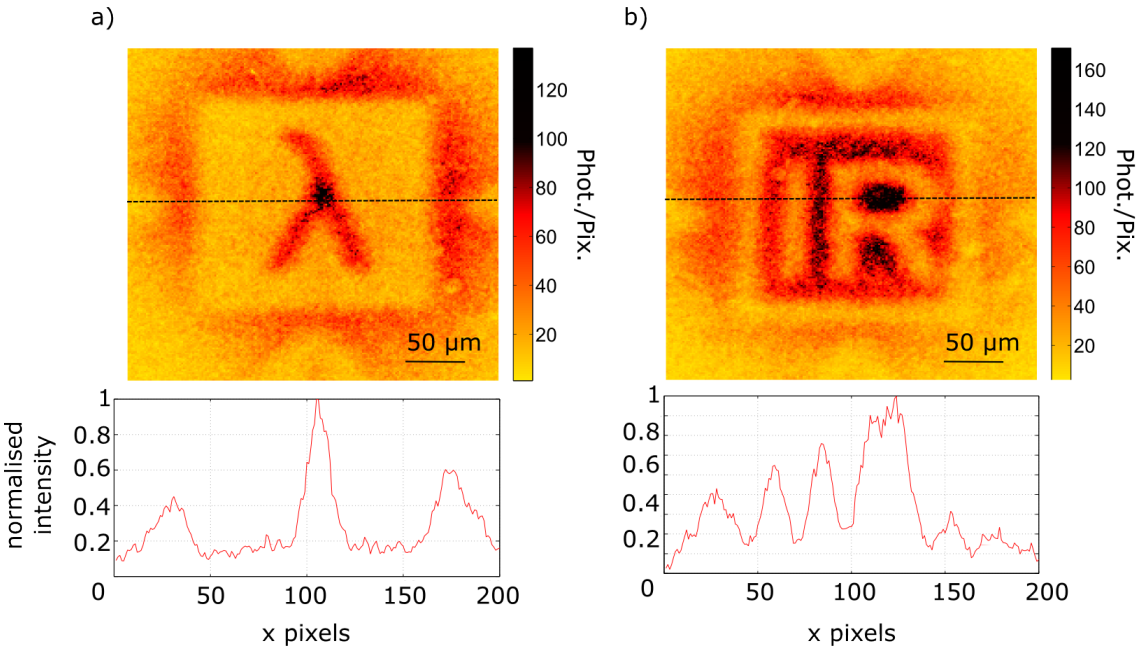

FIGURE 5.5: **Long exposure trans-spectral images:** 30 min acquisitions of a) a silicon λ on a gold background and b) a gold IR on a silicon background. The normalised cross-sections are the average intensity of the 10 pixels centred along the dotted line. The images have a contrast of $\sim 70\%$.

time resulting in high image quality, and a shorter exposure time and lower energy deposition, but lower quality images. However, whilst the total energy deposition in the sample is very low, the relatively long image acquisition times in our system still limit potential live-cell imaging applications.

5.6 Conclusion

In section 1.1, I raised the question "Is it possible to image a sample with a very small number of very low-energy photons?" In this chapter I have gone some way to answering this question by demonstrating that it is possible to obtain microscope images from visible photons at 460 nm, by illuminating the sample with position-correlated infrared photons at 1.55 µm.

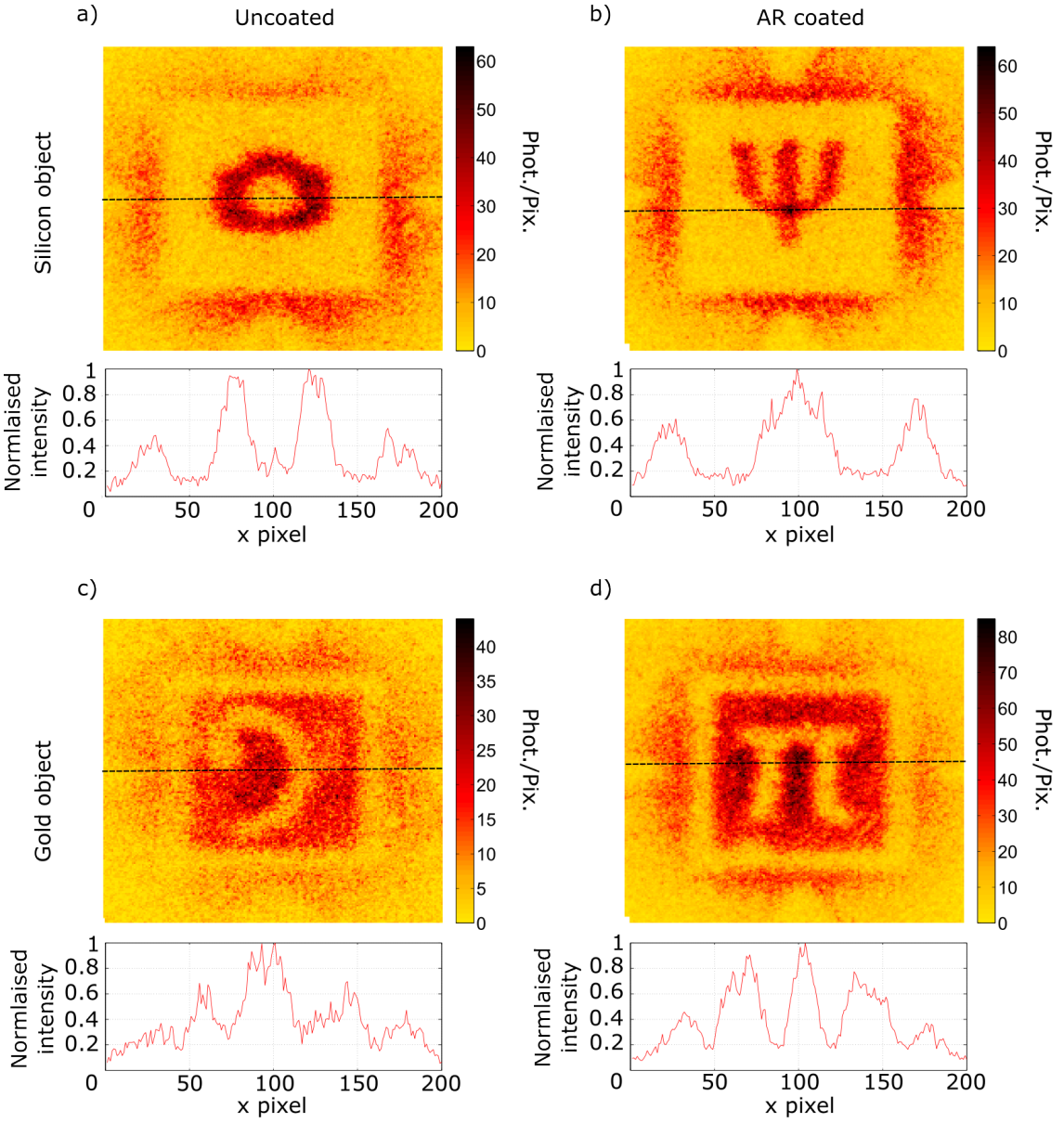

FIGURE 5.6: **Comparison of images acquired using an uncoated and an anti-reflection coated silicon chip:** Images from an a) uncoated and b) anti-reflection coated silicon chip.

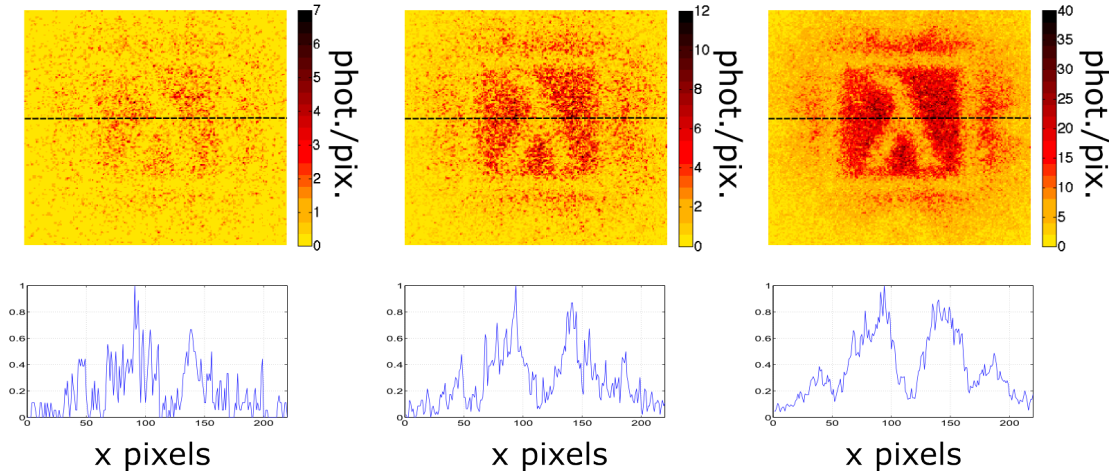

FIGURE 5.7: **Images with a very small energy deposition on the sample:** Images for 30 s, 2 mins and 10 mins exposures, corresponding to energy deposition on the sample of 800 fJ, 3 pJ and 15 pJ.

This system demonstrates that is possible to image a sample with energy depositions of several orders of magnitude less than typically used in live-cell imaging. Whilst this provides a positive answer to the question posed, the long acquisition times needed to acquire the images still suggest a practical application is some way off. Due to the heralded nature of the system, it is not possible to simply increase the illumination power to acquire an image, and any improvement on the system must therefore come from decreasing the inefficiencies currently present within the system. In the next chapter I shall discuss the origins of these inefficiencies, and the corresponding influence on the acquisition time and resolution of the acquired images.

Chapter 6

Detector Design

6.1 Introduction

The experiments presented thus far in chapters 3, 4 and 5 have all used multimode single-pixel heralding detectors. Multimode detectors, in order to have the capacity to detect many orthogonal modes, have a large FOV and NA. Detecting many modes clearly allows for a greater collection efficiency and thus enables a higher trigger rate. However, what is not immediately clear is whether or not a single mode heralding detector can be used for imaging, and what effect the FOV and NA of the heralding detector has on the efficiency and contrast of the acquired heralded images.

In this chapter I shall discuss aspects of heralding detector design with reference to images acquired for each detector type. I shall investigate interference effects, the resolution and contrast of the heralded images acquired on the camera and the influence of the heralding detector on the contributions to the camera readout.

6.2 Comparison of Single and Multimode Detectors

The modal bandwidth of the heralding detector is set by the input facet to the detector. In fibre-coupled detectors this may be limited by the collection optics or the fibre properties and in free space detectors is ordinarily limited by the input window to the detection area. By definition, only photons in the fundamental Gaussian mode are able to couple to a single mode detector whereas multimode detectors detect many different spatial modes - the number being dependent on the aperture size and NA of the detector. The NA of an optical component describes the maximum angle of incidence for which the beam is able to be detected and further propagated through the system. The NA of a fibre is determined by the step change in refractive index between the core and cladding within the fibre, given as

$$NA_{fibre} = \frac{1}{n_0}\sqrt{n_{core}^2 - n_{cladding}^2} \tag{6.1}$$

where n_0 is the refractive index of the medium around the fibre. Typical values for NA and FOV of a single mode fibre at 710 nm are $NA = 0.1$ and $d_{core} = 5$ µm, whereas multimode fibres typically have $NA \geqslant 0.22$ and $d_{core} \geqslant 50$ µm.

In free space optics the NA is defined as the sine of the half angle of collection of the optics. In the small angle approximation the NA for a lens is thus defined as

$$NA_{lens} = \frac{r_{lens}}{f} \tag{6.2}$$

where r_{lens} and f are the radius and focal length of the optic respectively.

6.3 Theory of Heralded Single Mode Detection

The mathematical description of heralded imaging provided in section 1.5.1 considered a multimode heralding detector in the object arm. I shall now adapt this theory to describe the detected state at the camera when using a single mode heralding detector.

The state detected by the multimode heralding detector, derived in equation (1.11), is $|\phi_1\rangle = \int d\boldsymbol{\eta}_1 g_1(\boldsymbol{\eta}_1)|\boldsymbol{\eta}_1\rangle$. However, the single mode detector only detects those photons which, after diffraction by the aperture function, are in the fundamental Gaussian mode, TEM_{00}. This change in modal composition within the detected state is expressed mathematically by replacing, $g_1(\boldsymbol{\eta}_1)$, the expression representing the transfer function for all spatial modes present in the beam, with $s_1(\boldsymbol{\eta}_1)$, a subset of $g_1(\boldsymbol{\eta}_1)$ which represents the transfer function for only the fundamental mode within the beam. The state detected by the single mode detector is therefore expressed as

$$|\phi_1\rangle = \int d\boldsymbol{\eta}_1 s_1(\boldsymbol{\eta}_1)|\boldsymbol{\eta}_1\rangle \,. \tag{6.3}$$

The coincidence measurement, rather than being across all spatial modes, detects only those photons at the camera that are correlated with photons that were diffracted into the fundamental mode and detected by the heralding detector. This limits the state detected by the coincidence measurement to

$$P_i = |\langle\phi_1|\langle\phi_2^i|\Psi_{1,2}\rangle|^2 = \iint d\boldsymbol{\eta}_1 d\boldsymbol{\eta}_2 \Psi(\boldsymbol{\eta}_1, \boldsymbol{\eta}_2) s_1^*(\boldsymbol{\eta}_1) f_i^*(\boldsymbol{\eta}_2) \,, \tag{6.4}$$

where $\Psi(\boldsymbol{\eta}_1, \boldsymbol{\eta}_2)$ is the transverse wavefunction of the down-converted photons, described by equation (1.10).

Despite the multimode nature of the ICCD, the coincidence image acquired is much smaller than the full FOV of the imaging system due to the restriction on the FOV imposed on the coincidence measurement by the heralding detector. The single mode restriction at the heralding detector not only results in a much lower collection efficiency over a smaller area, but also changes the coincidence state detected at the camera from a mixed state to a pure state. When considered according to the AWP, this is modelled by replacing the incoherent source with a source displaying coherence. Whilst it is possible to acquire an image using both source types, it is critical to have a coherent source if one wishes to measure a diffraction pattern. The different spatial modes in the multimode case interfere and so effectively wash out any interference pattern, whereas in the single mode case it is possible to obtain a heralded image of the diffraction pattern. In this chapter I shall discuss the full ramifications of single and multimode heralding detection in terms of imaging capabilities and resolution of the acquired images.

6.4 Imaging and Diffraction

The experimental apparatus and methodology used to investigate the effect of multimode and single mode heralding detectors on the heralded images and diffraction patterns largely follows that described previously in section 3.3, with the following minor modifications. Rather than using the interchangeable lens system between the BBO crystal and the BS, an interchangeable lens system was placed after the delay line to re-image or to Fourier transform the down-converted field at the output plane of the delay onto the ICCD. The transformation from the SPDC source to the ICCD was therefore characterised either by an imaging system with magnification $M = 3$ or a Fourier system with an effective focal length of $f_e \approx 167$mm. We also replaced

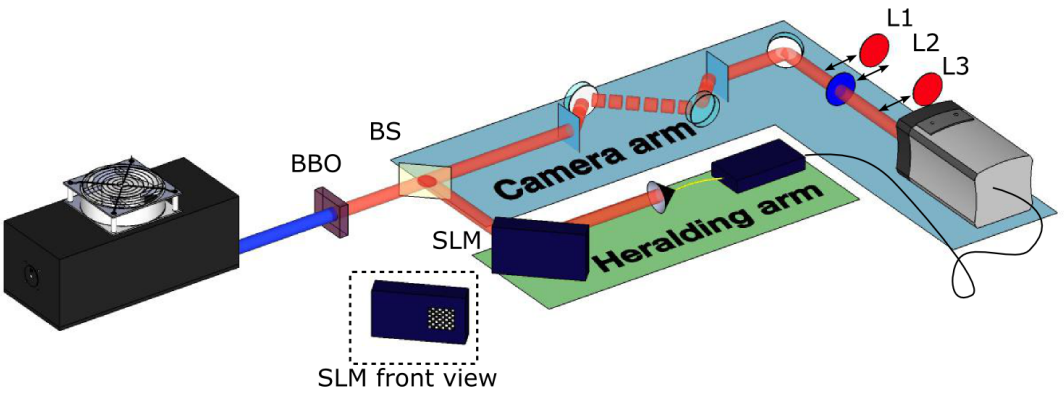

FIGURE 6.1: **Imaging and diffraction experimental setup:** An interchangeable lens system was placed after the delay line before the camera. Lenses 1 and 3 Fourier transformed the output of the delay onto the camera, such that the camera was in the far-field of the object. Lens 2 imaged the object onto the plane of the ICCD. The object was displayed on a spatial light modulator (SLM).

the object with a spatial light modulator (SLM) which displayed a binary intensity object. The reduced experimental setup is shown in figure 6.1.

Our SLM was a LCOS-SLM from Hamamatsu with an array of 600×800 pixels of pitch 20 µm. SLM's use liquid crystals which can be individually addressed with a voltage, causing them to rotate. This rotation can be used to imprint any arbritrary phase or amplitude modulation onto the impinging light field. In order to investigate imaging and diffraction effects, we programmed the SLM to produce an amplitude modulation with the shape of a chess board, *i. e.* a pattern of alternate opaque and transparent squares. The aperture function $A(\eta_o)$ associated with this modulation assumed only the values "0" or "1", such that $A^2 = A = A^\star$. The side length of each square was 300 µm, corresponding to 15 pixels of the SLM.

6.4.1 Results

We used four different configurations in order to fully characterise the system: single mode or multimode heralding detector, with the ICCD in either the image plane or far-field of the object for both heralding detector types. We used the same trigger mechanism and image acquisition settings as those used in chapter 3. The trigger rate of the ICCD when using the single mode heralding detector was 1.3 kHz where as the trigger rate when using the multimode heralding detector was 104.7 kHz. In both instances the dark count rate from the SPAD was ≈ 1 kHz.

We worked with a ROI on the ICCD comprising 600×600 pixels, giving a FOV of (7.8×7.8) mm^2. Figure 6.2 shows the resulting images acquired using the single mode and multimode heralding detectors. Horizontal cross-sections of the acquired images are shown in figure 6.3. The strip over which the cross-sections were taken is displayed over the top of each, and consists of the average of the 20 central rows for the images taken in the image plane and the 120 central rows for the images taken in the far-field. It is clear from the images that it is possible to acquire an image of the object with either a single mode or multimode heralding detector, albeit with a marked difference in imaging efficiency. It is also clear from the cross-sections in figure 6.3 that despite the difference in imaging efficiency, the contrast in the multimode and single mode images is the same, $\approx 75\%$. However, it is only possible to obtain a diffraction pattern of the chess board pattern when using a single mode heralding detector, due to the requirement for coherence in the detected coincidence state. I shall now discuss the aspects of the imaging system which affect the resolution, contrast and detection efficiency of the acquired heralded images, with reference to both single mode and multimode heralding detectors.

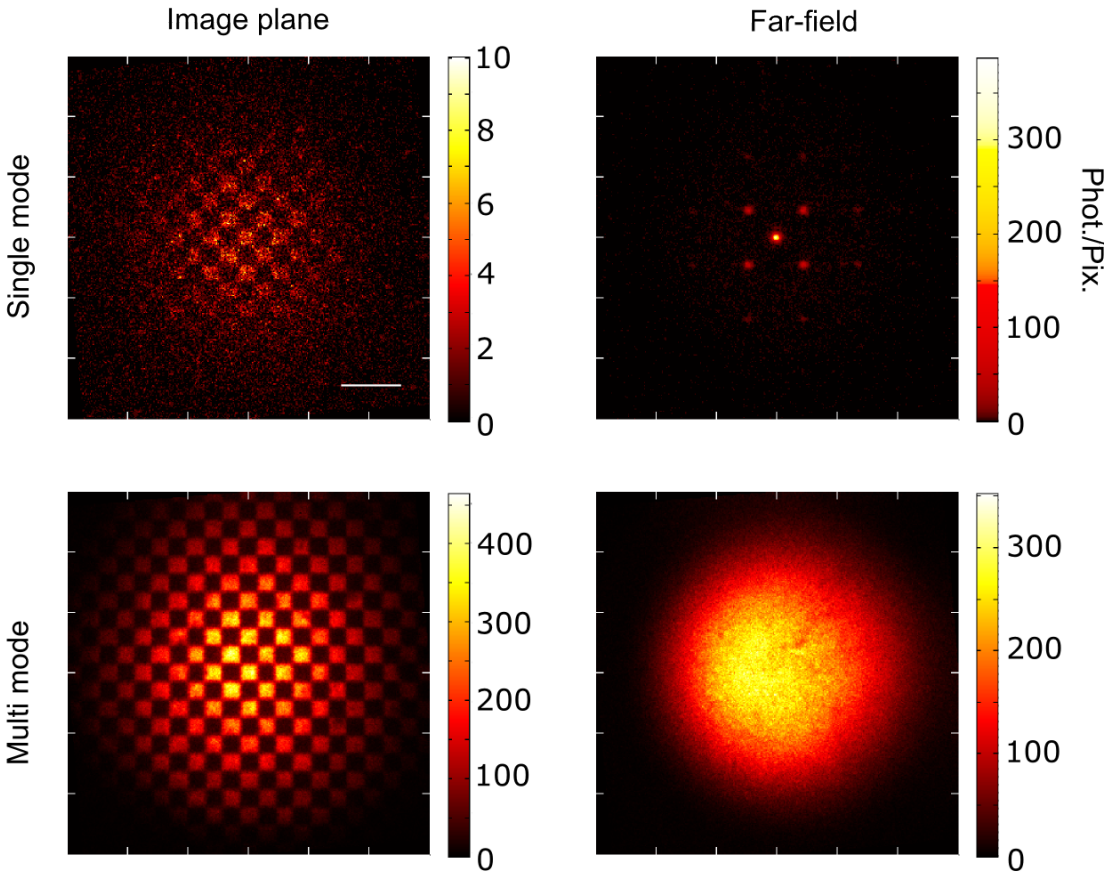

FIGURE 6.2: **Images and diffraction pattern obtained using single and multimode heralding detectors:** The images (left hand column) and diffraction patterns (right hand column) of the object using single mode (top row) and multimode (bottom row) heralding detectors. Whilst both detectors can be used to acquire an image, albeit with differing efficiencies, only the single mode detector enables the acquisition of the diffraction pattern. This is due to the requirement for coherence within the detected coincidence state. Scalebar=1.3 mm.

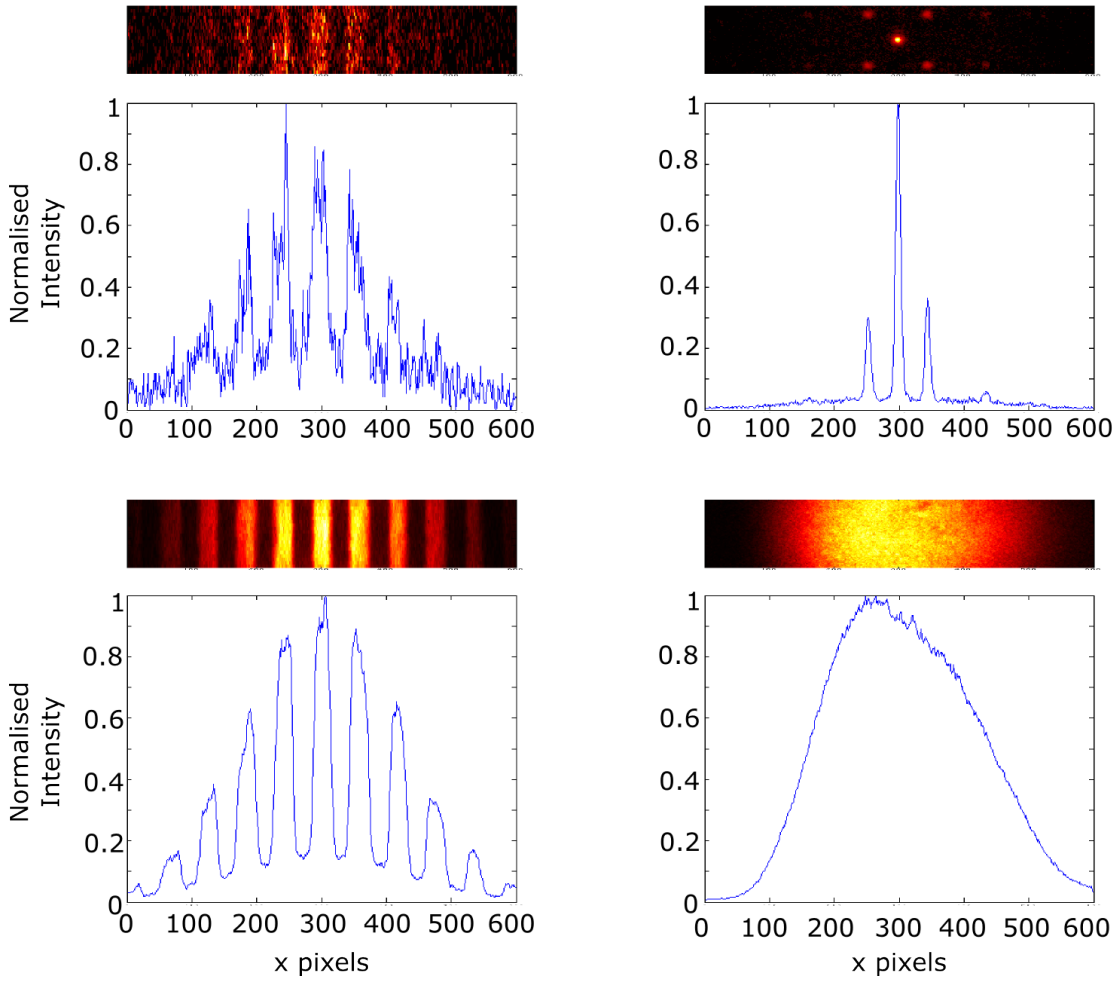

FIGURE 6.3: **Cross-sections of the images and diffraction patterns for single and multimode detectors:** The contrast and resolution in the images (left hand column) obtained with single and multimode detectors is comparable. The diffraction pattern obtained using a single mode heralding detector has a high contrast whereas the image obtained with the ICCD in the far-field of the multimode heralding detector has no internal structure beyond that of the down-converted field.

6.5 Discussions on Contrast and Resolution

There are several factors which determine the resolution of the acquired images on the ICCD. These factors rely on the characteristics of 3 parts of our system: The source, the detectors and the relay optics. In the following section, I shall describe the influence each of these components has on the acquired heralded image and how they combine to give the overall image resolution. In the first instance, the strength

of the correlations and the correlation length between the down-converted photons will be discussed. I shall then look at the heralding detector and compare single and multimode detection with regard to modal composition and then discuss the limiting factors of the detection mechanism within the ICCD. I will show that whilst the source places fundamental limitations on the resolving power of our system, the resolution of the acquired image is often limited by the relay optics and ICCD camera.

6.5.1 Source characteristics

The strength of the correlations between the photons in the down-converted photon pairs not only allows the acquisition of high-resolution, high-contrast heralded images in both the image plane and far-field of our source, as shown in chapter 3, but also places a fundamental limit on the resolution of the imaging system. The degree to which the measured position of the visible signal photon recorded by the ICCD camera corresponds to that of the idler probe photon is set by the width of the correlations between the twin photons, a function of the phase-matching within the SPDC process. This correlation length can be estimated from the two-photon wave function, equation (3.1). As mentioned, in that equation $\sigma_{\pm}$ are the standard deviations of two Gaussian functions that describe the strength of the position and momentum correlations respectively. The strength of the momentum correlations between the down-converted photons is described by σ_{+}^{-1}, the inverse of the transverse width of the pump beam. However, given that the imaging experiments presented in this thesis predominantly have the object and ICCD in an image plane of the crystal, it is thus the width of the position correlation between the twin down-converted photons that fundamentally determines the resolution of the imaging system. This length at the plane of the object is described by σ_{-} [71] and is calculated according to

$$\sigma_{-} \approx M\sqrt{\frac{\alpha L}{k_p}}\,, \tag{6.5}$$

where α is an adjustment constant taken to be 0.455 such that the sinc function in the phase-matching term can approximated by a Gaussian [71, 102] and M is the magnification between the crystal and the imaging plane. For the experiment described above in section 6.4.1, the correlation length is $\sigma_{-} = 8.8$ μm. Whilst this is the fundamental limit to the resolution of the system, it is clear that this number is lower than the acquired resolution in the imaging experiments presented thus far, suggesting the detectors and relay optics play a limiting role in determining the resolution of the imaging system.

6.5.2 Relay optics and detectors

The size of resolvable feature in the imaging system can never be smaller than the size of the mode generated in the SPDC process. However, a more obvious limiting factor to the resolution of the acquired images is the relay optics and imaging detector. Imaging systems can be characterised by a PSF, a function that describes the response of the system to an infinitely small point source. An acquired image can thus be described as the convolution between the object being imaged and the PSF,

$$\mathcal{I}(x,y) = \mathcal{O}(x,y) * PSF(x,y)\,. \tag{6.6}$$

The PSF is ordinarily described by a Gaussian function, the width of which is determined by the imaging optics. In our imaging systems, I calculated the PSF by deconvolving a sharp binary transition in the image with a step function, giving a

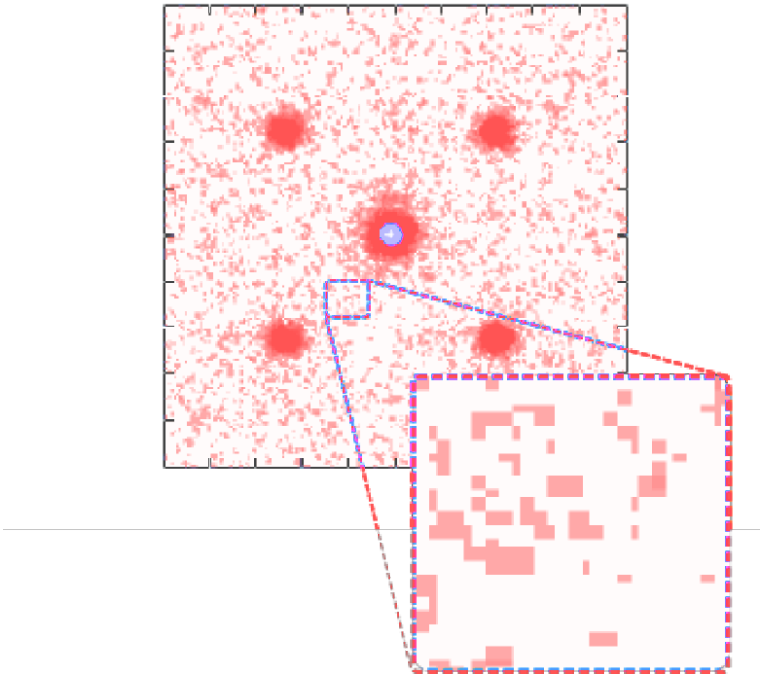

FIGURE 6.4: **Multi-pixel islands on the ICCD:** Due to blooming effects in the intensifier, each photo-detection appears on the camera as a multi-pixel island, as shown in the enlarged section of the single mode diffraction pattern.

Gaussian described by a standard deviation, σ_{PSF}, which is used to describe the resolution of our imaging system. The PSF of the system described in section 6.4.1 is $\sigma = 38$ µm at the plane of the BBO crystal.

The PSF in the camera arm of the system is a function of the optics used in the delay arm, and the intensifier of the ICCD. The photo-detections on the CCD chip of an ICCD happen after the amplification of the input photons on the intensifier. This amplification process spreads the signal resulting from a single photon over neighbouring pixels on the CCD chip, reducing the resolution of the detection mechanism. Thus whilst the size of the pixel on the ICCD is $(13\ \mu\text{m})^2$, the actual resolution of the camera is more readily approximated as an "island" with a 2×2 pixel extent, as shown in figure 6.4 [103]. The effect of this blooming in the intensifier on the resolution can be reduced by suitable magnification of the down-converted beam in the camera arm.

6.5.3 Modal bandwidth of the heralding arm

The correlation length of the generated down-converted photons and the PSF of the imaging system sets the resolution of the imaging system. However, the relay optics and choice of single-pixel detector in the heralding arm can limit the modal capacity of the system, in turn limiting the FOV and detection efficiency of the imaging system.

The modal capacity of a system is quantified by the optical etendue of the imaging system [104], defined as

$$N \equiv \frac{A\Omega}{\lambda^2} \tag{6.7}$$

where A is the effective area of the source and Ω is the effective solid opening angle, proportional to α, the emission angle of the source in equation (1.8).

For the above experiment, working in a near-collinear regime set a maximum emission angle of ≈ 0.01 rad from the BBO crystal. The effective area of the source was set by the waist of the pump beam, 1.5 mm FWHM. For maximum collection efficiency at both detectors, the relay optics and heralding detector must be selected such that the system has a greater etendue than the source at all points.

Assuming relay optics which fulfil this criteria, the choice of single-pixel detector becomes the limiting factor in the heralding arm. The down-conversion source used in the imaging system is clearly multimode, with associated etendue. As such the etendue of a single mode heralding detector will always be less than that of the source, with corresponding impairment of collection efficiency. The correct choice of multimode detector allows etendue matching throughout the heralding arm and thus removes this fundamental limit to efficiency.

An estimation of the coupling efficiency of the heralding arm can be calculated as the ratio between the number of modes generated at the source and the modal capacity of the detector. As a trivial approximation, the number of modes in the source is the square of the ratio between the correlation width of the down-converted photons and the waist of the pump beam. Approximating the detector with a square collection area of size D, the modal capacity of the heralding detector can be estimated as

$$M_D \approx \left(\frac{2NA \times D}{\lambda}\right)^2 . \tag{6.8}$$

Using the above approximations, the multimode detector in the above experiment had a collection efficiency of ~ 50 times that of the single mode detector. This is evident in figure 6.2 and figure 6.3. One sees that the number of photons in the multimode image of the chess board is ~ 50 times that of the number of photons in the single mode image, but one also sees that the resolution and contrast in both images are comparable.

When considering the question raised in section 1.1, "Is it possible to image a sample with a very small number of very low-energy photons?", it is clear from the above argument that, when considering position-correlated heralding imaging, a large multimode heralding detector is advantageous. It is only when considering imaging applications that require a coherent source, i. e. phase imaging [53, 105] or diffractive effects as shown in section 6.4.1, that using a single mode heralding detector becomes appealing.

6.6 Camera Readout

In previous chapters I have made passing mention of the various background contributions in the images, and discussed how to remove some of these in section 2.5. In

this section I will detail the components of the readout from the camera and discuss how to maximise the SBR of the acquired images.

The camera is gated by a trigger signal from the heralding detector, and the signal is read out after a certain exposure time, ordinarily $2-3$ seconds as discussed in section 2.2.2. The gating time is short (several ns) in order to detect only the correlated photon. This short gating time not only reduces much unwanted noise from the surroundings, but makes each contribution to the camera readout signal quantifiable.

The gate of the intensifier is fired for each detection at the heralding detector, and this heralding signal per second is described by

$$S_{HD} = \sum_{x}^{U} \sum_{y}^{V} g_{x,y} \eta_{HA} \mathcal{N}_{sec} \,, \tag{6.9}$$

where $U(V)$ is the number of pixels in $x(y)$, g is the transfer function of the down-converted field from the crystal to the detector, including the relay optics and object transmission function, η_{HA} is the detection efficiency of the heralding arm, including the relay optics and detector efficiencies and $\mathcal{N}_{sec}$ is the average number of down-converted photon pairs generated per second.

The total readout signal from the ICCD camera per second summed over all pixels consists of 4 terms: 1 signal term and 3 noise terms. The signal term is described by

$$S_{signal} = S_{HD}(P(\mathcal{N}_{pul}, 1) \times \mathcal{R}) \eta_{HE} \,, \tag{6.10}$$

where $P(\mathcal{N}_{pul}, 1)$ is the Poissonian probability of one down-converted pair per pulse given an average number of pairs generated per pulse, $\mathcal{N}_{pul}$, $\mathcal{R}$ is the repetition rate of the laser, and η_{HE} is the heralding efficiency of the system.

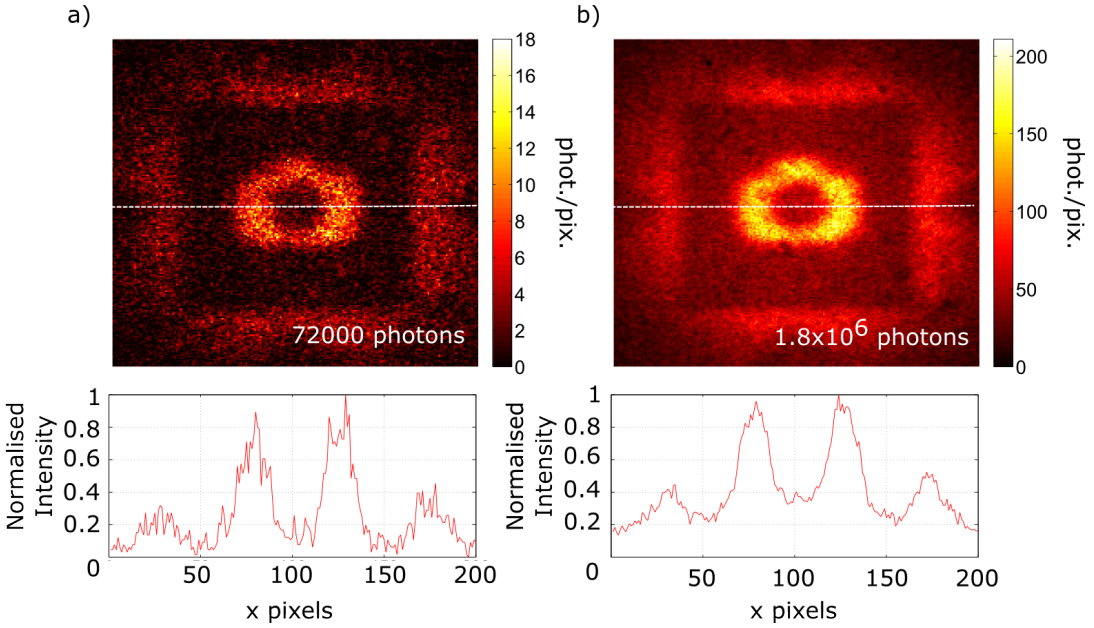

FIGURE 6.5: **The effect of increasing pump power on the noise in heralded images:** Images obtained using a) attenuated by a factor of 3 and b) full pump power. The image in b) has a much lower SBR as a result of detecting uncorrelated photons generated through double pair production in the SPDC process.

The first noise term arises from the probability of detecting an uncorrelated photon due to double pair production in one pulse, given by

$$S_{double} = S_{HD}(P(\mathcal{N}_{pul}, 2) \times \mathcal{R})\eta_{CA}\,, \tag{6.11}$$

where $P(\mathcal{N}_{pul}, 2)$ is the Poissonian probability of 2 down-converted pairs per pulse and η_{CA} is the detection efficiency of the camera arm. This noise contribution is illustrated in figure 6.5, where the image on the left is attenuated to reduce the probability of double pair production, and the image on the right is the image obtained using the full pump power.

The heralding detector also triggers the intensifier of the camera with each dark count, leading to the detection of uncorrelated photons being detected during these trigger windows. This noise term is given by

$$S_{DC} = DC(\tau \times \mathcal{R})\mathcal{N}_{pul}\,, \tag{6.12}$$

where DC is the number of dark counts from the heralding detector and τ is the gate width of intensifier. The final noise term is independent of the trigger rate of the heralding detector and is the probability of registering a false count from read-out noise on the camera. This probability can be calculated within the photon counting methodology described in section 2.5, and is given by

$$S_{RN} = (N \times M)\xi\,, \tag{6.13}$$

where ξ is the probability of a read-out noise count per pixel. Figure 6.6-a) demonstrates this noise contribution by showing the total number of photons in an image of a λ for different threshold values, and also the total number of photons once the noise events, calculated from the noise probability per pixel, have been subtracted. It is clear that the acquired images, when using a low threshold in the photon counting methodology, have a substantial noise contribution. However, for high threshold values the effect of camera read-out noise becomes negligible. Sample images of the λ for a threshold of 20, 40 and 60 are displayed in figure 6.6-b)-d) with associated cross-sections. Whilst the lower threshold image is clearly noisier, the contrast in the two higher threshold images is comparable. There is however a noticeable decrease in the number of photons detected in the threshold of 60 image and it is therefore important that not too high a threshold is set so as to avoid the unecessary discarding of real photons in the image.

By combining these terms, I derive a total readout per second from the camera, summed over all pixels,

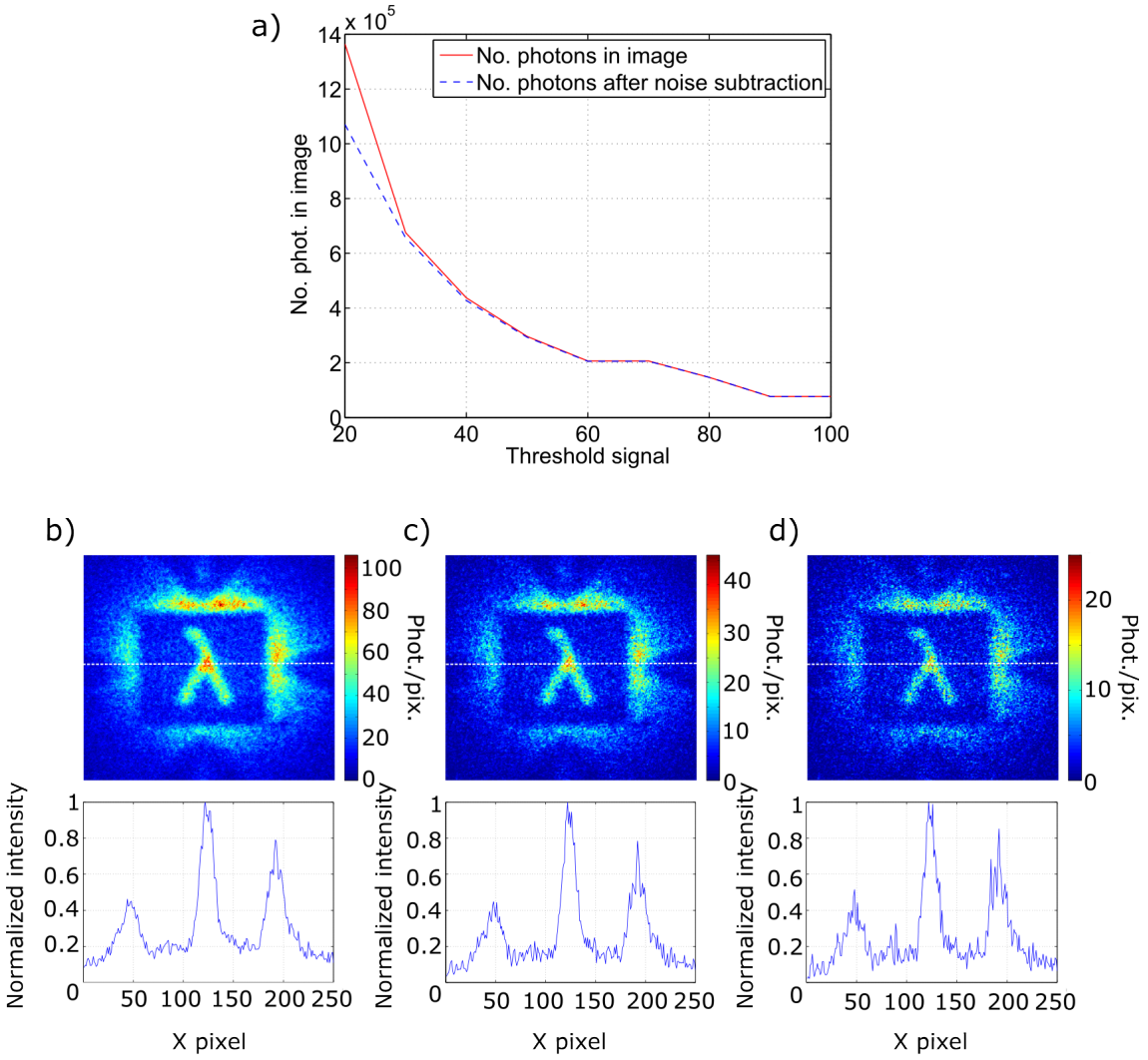

FIGURE 6.6: **The effect of changing the photon counting threshold on the noise in heralded images:** a) The summed total number of photons in the heralded image and number of photons in the heralded image after subtracting the number of noise photons calculated using the noise probability per pixel. b)-d) Images obtained for threshold values of b) 20, c) 40 and d) 60. The noise decreases significantly up to a threshold value of approximately 30, care must be taken not to set too high a threshold so as to avoid unnecessarily discarding real photo-events in the acquired image. For the data shown here, the optimum threshold is 40.

$$S = S_{signal} + S_{double} + S_{DC} + S_{RN} \,. \tag{6.14}$$

From equation (6.14), one can describe the SBR of the acquired image,

$$\begin{aligned} SBR &= \frac{S_{signal}}{S_{double} + S_{DC} + S_{RN}} \\ &= \frac{S_{HD}(P(\mathcal{N}_{pul}, 1) \times \mathcal{R})\eta_{HE}}{S_{HD}(P(\mathcal{N}_{pul}, 2) \times \mathcal{R})\eta_{CA} + DC(\tau \times \mathcal{R})\mathcal{N}_{pul} + (N \times M)\xi} \end{aligned} \tag{6.15}$$

By careful choice of parameters within each experiment, it is possible to reduce the noise terms in equation 6.15, thus maximising the SBR per frame.

In order to minimise double pair generation per pulse (equation (6.11)), it is important to ensure $\mathcal{N}_{pul} < 1$, i. e. there are fewer than one down-converted photon pairs generated per pump laser pulse. SPDC is a non-linear process, and so the number of down-converted photons generated scales with the square of the power of the pump beam [106]. Assuming degenerate SPDC, the maximum power conversion from pump frequency, ω, to down-converted pair frequency, 2ω, is given by

$$\frac{P(2\omega)}{P(\omega)} = 1.068 \left(\frac{128\pi^2 \omega_1^3 d_{eff}^2 L}{c^4 n_1 n_2} \right) P(\omega) \tag{6.16}$$

where d_{eff} is the optical non-linear coefficient of the BBO crystal, L is the length of the crystal, $n_{1(2)}$ are the refractive indices of the BBO crystal for pump (1) and signal (2) frequencies respectively.

Using equation (6.16), one can calculate the average number of down-conversion photons per second, and it is therefore trivial to determine the average number of down-converted photons per pulse of the pump laser. In the single photon regime, Poissonian statistics are used to calculate the probabilities associated with generating

k photon-pairs per pulse, based on an average number of down-converted photon pairs per pulse, $\mathcal{N}_{pul}$.

$$P(k, \mathcal{N}_{pul}) = \frac{\mathcal{N}_{pul}^{k} e^{-k}}{k!}\,, \tag{6.17}$$

where k is the desired number of photons and $\mathcal{N}_{pul}$ is the average number of down-converted photon pairs generated per pump laser pulse. We attenuate the power of the pump laser such that the average number of down-converted pairs produced per pump laser pulse is small enough that the probability of generating two down-conversion pairs per pulse is negligible.

The probability of a false detection arising from read-out noise on the camera, ξ, is determined by the photon counting methodology presented in section 2.5, and is typically of order 10^{-4} per pixel. The dark counts from the heralding detector are detector dependent. Typical values however are ~ 1000 Hz for a SPAD and ~ 50 Hz for a SNSPD.

6.7 Trans-spectral Imaging with Single Mode and Multimode Heralding Detectors

The trans-spectral images presented in section 5.5 were acquired using a multimode SPAD as the heralding detector. We also performed this experiment using a single mode fibre-coupled SNSPD. I shall now briefly discuss the differences between these detectors, with associated results.

6.7.1 Comparison of detector types

There are advantages and disadvantages to using either an SNSPD and a SPAD for SWIR single photon detection, related to the detection mechanisms described in section 2.2.3.

The nature of the superconducting transition and the biasing of SNSPDs mean they are very sensitive to fluctuations in the ground of the system and thus fluctuations in the power supply to the lab can arbitrarily lead to large spikes in the dark counts from the detector. However, the bias can be controlled such that the dark count rate is minimal - ~ 50 Hz for our experiment - and the dead time of the detector is only of order pico-seconds with no possibility of double-pulsing, the phenomemon whereby the pulse from the detected photon also gives an output signal. These allow very fast photo-detection with a minimal probability of dark count detection.

In contrast, the InGaAs/InP SPAD is much easier to use as it is not so dependent on a perfectly stable power supply and does not require bulky compressors and other apparatus to cool it to superconducting temperatures. However, the dead time and trigger rate must be carefully controlled so as to avoid potential double-pulsing, and this dead time places a fundamental limit to the number of detections which can be made per second. The SPAD also has a much higher dark count rate, $>$ 1kHz, which leads to a higher background signal in the images on the camera, as described in section 6.6.

Figure 6.7 shows a direct comparison between the image of the λ acquired using the multimode SPAD as heralding detector, and the image acquired using the single mode fibre-coupled SNSPD. It is clear that the FOV using the single mode detector is smaller, as is the overall efficiency - the multimode image has five times more photons across the wider FOV. The resolution in the single mode image is also noticeably less than the resolution in the multimode image.

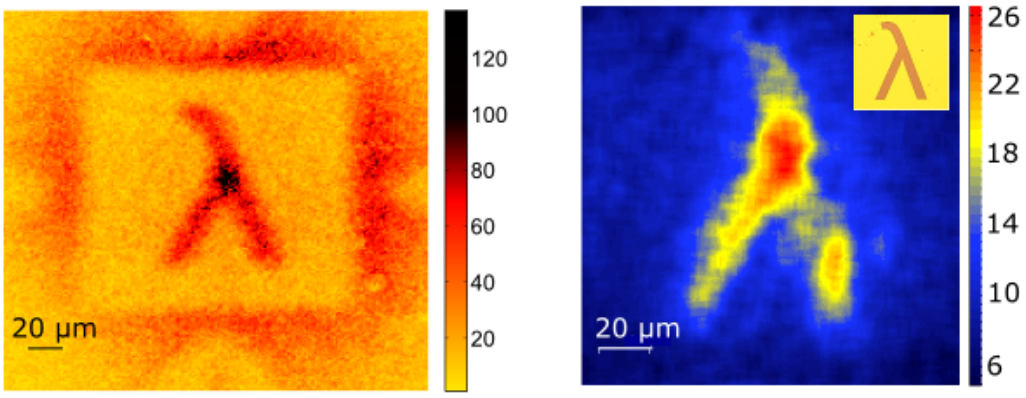

FIGURE 6.7: **Trans-spectral images using single and multimode heralding detectors:** Images obtained using a multimode (left) and single mode (right) heralding detector. The efficiency of the imaging system is greatly improved by using a multimode heralding detector. The difference in resolution between the two images is an experimental defect resulting from poor alignment due to very low signal.

The modal capacity of the heralding detector does not have an affect on the acquired resolution of the images, as shown previously in figure 6.2. Rather the difference in resolution between the two images in figure 6.7 is a consequence of the relative detection efficiencies and thus usability of each detector. When using the single mode heralding detector it was much harder to detect a meaningful level of signal, particularly when dramatically attenuating the pump laser in order to reduce double down-converted pair generation within one pump pulse. This made it very hard to align and image the object at precisely the correct focus.

The experiment was initially performed using the single mode heralding detector, and a further consequence of changing heralding detector to a multimode detector was the realisation of the possible resolution of the system. Initial tests when using

the single mode detector suggested a resolution limited to that shown in figure 6.7-b). However, the increased efficiency and signal when using the multimode heralding detector highlighted the achievable resolution of the system. In view of this, and in order to circumvent the need to acquire large amounts of data before evaluating the focus of the image, we built an alignment "spotter" using a standard CCD and white light illumination. Viewing the sample on this spotter enabled the quick and easy alignment of the object such that it was no longer necessary to wait for an accumulated image to see the precise alignment in all 3 dimensions.

The PSF of the trans-wavelength system, determined by analysing the sharp transisition between the gold boundary of the sample and the silicon internal box on the image of the λ, figure 6.7, was $2\sigma = 18$ µm at the sample plane. By considering this PSF and the size of our sample we calculate that our acquired images in chapter 5 contain ~ 9 effective pixels within the boundary box in each transverse direction.

6.8 Conclusion

As described in this chapter, there are many diverse elements to the heralded imaging system presented in this thesis, all of which contribute in some measure to the resolution, contrast and efficiency of the acquired images. In this chapter I have discussed the influence of the heralding detector on the acquired images, discussing the superiority of multimode detection when imaging a transmissive object, but acknowledging the requirement of single mode detection when wishing to image phase objects or diffraction patterns. I have also presented an analysis of the resolution of the system and the various contributions to the data acquired on the camera. Optimisation of each of the factors discussed in this chapter allows efficient acquisition of low photon flux heralded images.

Chapter 7

Discussion and Conclusion

7.1 Discussion

At the beginning of this thesis I posed two questions:

- "How many photons does it take to form an image?"
- "Is it possible to image a sample with a very small number of very low-energy photons?".

In order to answer these questions, my colleagues and I developed a heralded quantum imaging system. This system, described in chapter 2, used an ICCD camera to obtain images of an object with very few photons, none of which had themselves interacted with the object. It did this by exploiting the strong spatial correlations between the twin photons generated through the SPDC process. One of these photons probed the object and was detected by a single-pixel heralding detector. The signal from this heralding detector triggered the intensifier of the ICCD to detect the correlated photon. The high sensitivity and short gating time of the camera allowed the acquisition of images with a very small number of photons and a low background signal. The use of a camera allowed the detection of the photons across the full image

scene simultaneously and thus enabled the acquisition of images with a significantly higher detection efficiency than previous scanning imaging systems.

High-sensitivity, multi-megapixel cameras typically acquire images containing many millions of photons. However, one can imagine several scenarios where imaging using very small numbers of photons would be beneficial, for instance in covert imaging, or the imaging of light-sensitive samples. It is considerations such as these which encourage a definitive answer to the question of the number of photons needed to acquire an image. Compressive sampling techniques and our heralded imaging system provided an ideal test bed for searching for an answer to this question. We showed that it is possible to acquire an image using an average of only 0.5 photons per pixel. There are, however, several further considerations contained within this simplistic statement, that require further thought.

We used compressive sampling techniques to reconstruct an image from a sparse data set by exploiting sparsity in the DCT basis. However, calculating the DCT of an entire image for each iteration was computationally intensive and time consuming leading to questions of efficiency: Is the DCT basis the optimum for all images or are there certain situtations where an alternative basis would be sparser? Under what circumstances can one divide the images into smaller sections (as done in JPEG compression) so as to only calculate the DCT of a small section? In order for this compressive technique to find application in a practical application, these questions would need to be answered such that it became possible to reconstruct images in timescales approaching real-time.

A significant advantage to using our system for low-light imaging is the ability to image at disparate wavelengths; probing the object with SWIR whilst developing the image using visible photons. This circumvents the need to use inefficient and expensive multi-pixel SWIR-sensitive detector arrays. In chapter 5, I showed that one can acquire images using an illumination power of only 25 fW, and an energy deposition

on the sample of 40 pJ cm^{-2} s^{-1}. This is of order 8 orders of magnitude lower than typical cellular damage thresholds [107, 108]. Any live-cell imaging application must naturally fall below this threshold, and typical live-cell microscopy systems have an energy deposition on the sample of order $mJcm^{-2}$. Even beside this lower limit, the trans-spectral imaging system presented here deposits ~ 3 orders of magnitude less energy in the sample. However, whilst the energy deposition in the sample is significantly smaller than current live-cell imaging techniques, there are a number of challenges to overcome before this system could be realised in practical applications.

The resolution of our system is fundamentally limited by our down-conversion source. However, in our current system the relay optics degrade the resolution significantly. The acquisition time for each image is also long, of order minutes, and is therefore impractical for any live-cell imaging. Both of these factors are influenced by the length of the image-preserving, free-space delay line in the camera arm of the experiment. This both degrades the resolution and efficiency of the system. In order to bring the system closer to a practical application, this delay line would need to be reduced, possibly by using an alternative method such as techniques currently being developed that reconstruct an image from the signal emerging from a multimode fibre using the transmission matrix of the fibre [109].

In this thesis, the two questions stated above have largely been treated as separate questions. However, longer term development of both compressive techniques and the trans-spectral imaging system would invite the combination of both within a single imaging system. Real-time compressive imaging of a biological sample would enable live-cell imaging at energy levels significantly below current state-of-the-art systems.

7.2 Conclusion

In this thesis I have sought to quantify the number of photons required to form an image, and develop a system that enables the acquisition of an image of an object using very small numbers of low-energy photons.

Chapter 1 discussed previous developments of the quantum ghost imaging technique and the theoretical framework that underpins my imaging system. I then described the necessary equipment for building the system and the methods used for aligning the heralded imaging system in chapter 2.

Having laid the foundations for building and aligning the system, I then presented images acquired using this imaging system in chapter 3. The efficiency of the imaging system was shown to be 3 orders of magnitude higher than previous scanning systems, and an image based utilisation of the EPR-type correlations of the source was also presented.

Whilst this imaging system allowed for the acquisition of images using a very small number of photons, the images still contained several photons per pixel, measured over a long exposure time. In chapter 4, I characterised the imaging system for several low-light imaging configurations and determined the optimum experimental setup. I then presented an image processing technique based on compressive sampling which enabled the reconstruction of an image with less than 1 photon per image pixel. This technique utilised the Poissonian statistics inherent in the detection of individual photons, and the sparsity of real images in a spatial frequency basis, to iteratively make changes to the acquired sparse data set and thus reconstruct an image. Using the combination of the heralded imaging system and these compressive techniques, I acquired an image of a wasp wing reconstructed using only an average of 0.5 photons per pixel.

Having answered the first question, "How many photons does it take to form an image?", chapter 5 presented an adapted heralded quantum imaging system, such that the generated correlated twin photons were at significantly different wavelengths - 460 nm and 1.55 µm respectively. This meant that the object could be probed using the low energy infrared photon whilst the image was developed using a standard silicon-based ICCD camera. The sample was probed with $\sim 2 \times 10^5$ photons per second, corresponding to an illumination power of 25 fW. The images shown in chapter 5 demonstrate that it is possible to illuminate an object with very few infrared photons whilst developing an image using visible photons on highly sensitive silicon-based cameras.

There are many different facets to the heralded imaging system, each of which affects the resolution and efficiency of the image process. In chapter 6 I discussed the influence the non-imaging detector had on the efficiency of the acquired images. I showed that, other than for specific applications such as phase imaging, a large area multimode heralding detector allows for the highest efficiency image acquisition. I then also discussed the resolution of the acquired images based on characteristics of source and detectors: Whilst the resolution is fundamentally limited by the width of the correlations in the source, the relay optics and detectors have a larger influence on the resolution of the acquired heralded images in this thesis. The camera acquisition settings were also then considered in order to minimise readout noise and dark counts in the image and thus enhance image contrast.

Imaging techniques that are enabled by quantum correlations have been utilised over the past 25 years. The system developed here was, however, the first imaging system to utilise a camera in a single-photon, heralded imaging configuration. This allowed the acquisition of images using a very small number of photons, demonstrating that one requires only 0.5 photons per pixel in order to reconstruct an image, and that

images can be acquired with illumination energy depositions of only several pico-Joules. The development of this system, and the images obtained represent a notable step forward in the development of low-light imaging techniques.

Bibliography

[1] M. Gatton. *Acts of Seeing*, chapter First Light: Inside the Palaeolithic camera obscura, pages 146–153. Artakt and Zidane Press, 2009.

[2] G. Sines and Y. A. Sakellarakis. Lenses in antiquity. *Am. J. Archaeol.*, 91(2): 191–196, 1987.

[3] G. Gasson. The oldest lens in the world: a critical study of the Layard lens. *The Opthalmic Optician*, page 1267, Dec 1972.

[4] Joseph N. Mait. A history of imaging: Revisiting the past to chart the future. *Opt. Photon. News*, 17(2):22–27, Feb 2006.

[5] Omar S. Magaña-Loaiza, Gregory A. Howland, Mehul Malik, John C. Howell, and Robert W. Boyd. Compressive object tracking using entangled photons. *Appl. Phys. Lett.*, 102(23):231104, 2013.

[6] Peter A. Morris, Reuben S. Aspden, Jessica E. C. Bell, Robert W. Boyd, and Miles J. Padgett. Imaging with a small number of photons. *Nat. Commun.*, 6 (5913), 2015.

[7] Lee A. Rozema, James D. Bateman, Dylan H. Mahler, Ryo Okamoto, Amir Feizpour, Alex Hayat, and Aephraim M. Steinberg. Scalable spatial superresolution using entangled photons. *Phys. Rev. Lett.*, 112(22):223602, Jun 2014.

[8] R. W. Boyd and C. H. Townes. An infrared upconverter for astronomical imaging. *Appl. Phys. Lett.*, 31(7):440, 1977.

[9] Jeffrey H. Shapiro and Robert W. Boyd. The physics of ghost imaging. *Quantum Inf. Process*, 11(4):949–993, 2012.

[10] Ori Katz, Pierre Heidmann, Mathias Fink, and Sylvain Gigan. Non-invasive single-shot imaging through scattering layers and around corners via speckle correlations. *Nat. Photonics*, 8(10):784–790, 2014.

[11] Genevieve Gariepy, Nikola Krstajic, Robert Henderson, Chunyong Li, Robert R. Thomson, Gerald S. Buller, Barmak Heshmat, Ramesh Raskar, Jonathan Leach, and Daniele Faccio. Single-photon sensitive light-in-flight imaging. *Nat. Commun.*, 6(6021), 2015.

[12] Patrick Llull, Xuejun Liao, Xin Yuan, Jianbo Yang, David Kittle, Lawrence Carin, Guillermo Sapiro, and David J. Brady. Coded aperture compressive temporal imaging. *Opt. Express*, 21(9):10526–10545, May 2013.

[13] B. Sun, M. P. Edgar, R. Bowman, L. E. Vittert, S. Welsh, A. Bowman, and M. J. Padgett. 3D computational imaging with single-pixel detectors. *Science*, 340(6134):844–7, May 2013.

[14] Stephen S. Welsh, Matthew P. Edgar, Richard Bowman, Phillip Jonathan, Baoqing Sun, and Miles J. Padgett. Fast full-color computational imaging with single-pixel detectors. *Opt. Express*, 21(20):23068–74, Oct 2013.

[15] Petros Zerom, Kam Wai Clifford Chan, John C. Howell, and Robert W. Boyd. Entangled-photon compressive ghost imaging. *Phys. Rev. A*, 84(6):061804, 2011.

[16] A. Einstein, B. Podolsky, and N. Rosen. Can quantum-mechanical description of physical reality be considered complete? *Phys. Rev.*, 47(10):0777–0780, May 1935.

[17] E. J. S. Fonseca, P. H. S. Ribeiro, S. Padua, and C. H. Monken. Quantum interference by a nonlocal double slit. *Phys. Rev. A*, 60(2):1530–1533, 1999.

[18] Nicolas Gisin, Grégoire Ribordy, Wolfgang Tittel, and Hugo Zbinden. Quantum cryptography. *Rev. Mod. Phys.*, 74(1):145–195, 2002.

[19] X. Y. Zou, L. J. Wang, and L. Mandel. Induced coherence and indistinguishability in optical interference. *Phys. Rev. Lett.*, 67(3):318–321, July 1991.

[20] Stephen M. Barnett. *Quantum Information*. Oxford University Press, 2009.

[21] M. D. Reid. Demonstration of the Einstein-Podolsky-Rosen paradox using nondegenerate parametric amplification. *Phys. Rev. A*, 40(2):913–923, Jul 1989.

[22] S. P. Walborn, C. H. Monken, S. Padua, and P. H. Souto Ribeiro. Spatial correlations in parametric down-conversion. *Phys. Rep.*, 495(4-5):87–139, October 2010.

[23] John C. Howell, Ryan S. Bennink, Sean J. Bentley, and R. W. Boyd. Realization of the Einstein-Podolsky-Rosen paradox using momentum- and position-entangled photons from spontaneous parametric down conversion. *Phys. Rev. Lett.*, 92(21):210403, May 2004.

[24] James Schneeloch and John C. Howell. Introduction to the transverse spatial correlations in spontaneous parametric down-conversion through the biphoton birth zone. *arXiv:1502.06996v2 [quant-ph]*, 2015.

[25] Milena D'Angelo, Yoon-Ho Kim, Sergei P Kulik, and Yanhua Shih. Identifying entanglement using quantum ghost interference and imaging. *Phys. Rev. Lett.*, 92(23):233601, Jun 2004.

[26] A. Mair, A. Vaziri, G. Weihs, and A. Zeilinger. Entanglement of the orbital angular momentum states of photons. *Nature*, 412(6844):313–316, July 2001.

[27] Timothy Yarnall, Ayman F. Abouraddy, Bahaa E. A. Saleh, and Malvin C. Teich. Experimental violation of Bell's inequality in spatial-parity space. *Phys. Rev. Lett.*, 99(17):170408, Oct 2007.

[28] J. Romero, J. Leach, B. Jack, S. M. Barnett, M. J. Padgett, and S. Franke-Arnold. Violation of Leggett inequalities in orbital angular momentum subspaces. *New J. Phys.*, 12:123007, December 2010.

[29] David C. Burnham and Donald L. Weinberg. Observation of simultaneity in parametric production of optical photon pairs. *Phys. Rev. Lett.*, 25(2):84–87, 1970.

[30] S. Friberg, C. K. Hong, and L. Mandel. Intensity dependence of the normalized intensity correlation function in parametric down-conversion. *Opt. Commun.*, 54(5):311–316, 1985.

[31] Hong, Ou, and Mandel. Measurement of subpicosecond time intervals between two photons by interference. *Phys. Rev. Lett.*, 59(18):2044–2046, Nov 1987.

[32] P. H. S. Ribeiro, S. Pádua, J. C. Machado da Silva, and G. A. Barbosa. Controlling the degree of visibility of Young's fringes with photon coincidence measurements. *Phys. Rev. A*, 49(5):4176–4179, May 1994.

[33] R. M. Gomes, A. Salles, F. Toscano, P. H. Souto Ribeiro, and S. P. Walborn. Quantum entanglement beyond Gaussian criteria. *P. Natl. Acad. Sci. USA.*, 106(51):21517–21520, 2009.

[34] C. H. Monken, P. H. S. Ribeiro, and S. Padua. Transfer of angular spectrum and image formation in spontaneous parametric down-conversion. *Phys. Rev. A*, 57(4):3123–3126, 1998.

[35] Robert W. Boyd. *Nonlinear Optics*. Academic Press, 3rd edition, 2008.

[36] Gabriela B. Lemos, Victoria Borish, Garrett D. Cole, Sven Ramelow, Radek Lapkiewicz, and Anton Zeilinger. Quantum imaging with undetected photons. *Nature*, 512(7515):409, 2014.

[37] Charles C. Kim and Gary Kanner. Infrared two-color ghost imaging using entangled beams. *Proc. of SPIE*, 7815(781503), 2010.

[38] F. M. Miatto, D. Giovannini, J. Romero, S. Franke-Arnold, S. M. Barnett, and M. J. Padgett. Bounds and optimisation of orbital angular momentum bandwidths within parametric down-conversion systems. *Eur. Phys. J. D*, 66 (7):178, 2012.

[39] Alessandro Fedrizzi, Thomas Herbst, Andreas Poppe, Thomas Jennewein, and Anton Zeilinger. A wavelength-tunable fiber-coupled source of narrowband entangled photons. *Opt. Express*, 15(23):15377–15386, Nov 2007.

[40] J. Romero, D. Giovannini, S. Franke-Arnold, S. M. Barnett, and M. J. Padgett. Increasing the dimension in high-dimensional two-photon orbital angular momentum entanglement. *Phys. Rev. A*, 86(1):012334, 2012.

[41] W. Wiechmann, S. Kubota, T. Fukui, and H. Masuda. Refractive-index temperature derivatives of potassium titanyl phosphate. *Opt. Lett.*, 18(15):1208–1210, 1993.

[42] Shai Emanueli and Ady Arie. Temperature-dependent dispersion equations for KTiOPO4 and KTiOAsO4. *Appl. Optics*, 42(33):6661–6665, 2003.

[43] T. B. Pittman, Y. H. Shih, D. V. Strekalov, and A. V. Sergienko. Optical imaging by means of two-photon quantum entanglement. *Phys. Rev. A*, 52(5): 3429–3432, Nov 1995.

[44] Ryan S. Bennink, Sean J. Bentley, and Robert W. Boyd. "Two-photon" coincidence imaging with a classical source. *Phys. Rev. Lett.*, 89(11):113601, Sep 2002.

[45] A. Gatti, E. Brambilla, M. Bache, and L. A. Lugiato. Ghost imaging with thermal light: comparing entanglement and classical correlation. *Phys. Rev. Lett.*, 93(9):093602, Aug 2004.

[46] A. F. Abouraddy, B. E. Saleh, A. V. Sergienko, and M. C. Teich. Role of entanglement in two-photon imaging. *Phys. Rev. Lett.*, 87(12):123602, Sep 2001.

[47] A. Gatti, E. Brambilla, and L. A. Lugiato. Entangled imaging and wave-particle duality: from the micro-scopic to the macroscopic realm. *Phys. Rev. Lett.*, 90 (13):133603, 2003.

[48] Ryan S. Bennink, Sean J. Bentley, Robert W. Boyd, and John C. Howell. Quantum and classical coincidence imaging. *Phys. Rev. Lett.*, 92(3):033601, Jan 2004.

[49] A. Gatti, E. Brambilla, M. Bache, and L. A. Lugiato. Correlated imaging, quantum and classical. *Phys. Rev. A*, 70(1):013802, 2004.

[50] Baoqing Sun, Stephen S. Welsh, Matthew P. Edgar, Jeffrey H. Shapiro, and Miles J. Padgett. Normalized ghost imaging. *Opt. Express*, 20(15):16892–16901, Jul 2012.

[51] Jeffrey H. Shapiro. Computational ghost imaging. *Phys. Rev. A*, 78(6):061802, 2008.

[52] Neal Radwell, Kevin J. Mitchell, Graham M. Gibson, Matthew P. Edgar, Richard Bowman, and Miles J. Padgett. Single-pixel infrared and visible microscope. *Optica*, 1(5):285–289, 2014.

[53] B. Jack, J. Leach, J. Romero, S. Franke-Arnold, M. Ritsch-Marte, S. M. Barnett, and M. J. Padgett. Holographic ghost imaging and the violation of a Bell inequality. *Phys. Rev. Lett.*, 103(8):083602, Aug 2009.

[54] Nestor Uribe-Patarroyo, Andrew Fraine, David S. Simon, Olga Minaeva, and Alexander V. Sergienko. Object identification using correlated orbital angular momentum states. *Phys. Rev. Lett.*, 110(4):043601, 2013.

[55] Mehul Malik, Heedeuk Shin, Malcolm O'Sullivan, Petros Zerom, and Robert W. Boyd. Quantum ghost image identification with correlated photon pairs. *Phys. Rev. Lett.*, 104(16):163602, 2010.

[56] R. M. Gomes, A. Salles, F. Toscano, P. H. Souto Ribeiro, and S. P. Walborn. Observation of a nonlocal optical vortex. *Phys. Rev. Lett.*, 103(3):033602, 2009.

[57] D. S. Tasca, R. S. Aspden, P. A. Morris, G. Anderson, R. W. Boyd, and M. J. Padgett. The influence of non-imaging detector design on heralded ghost-imaging and ghost-diffraction examined using a triggered ICCD camera. *Opt. Express*, 21(25):30460–30473, 2013.

[58] D. S. Tasca, S. P. Walborn, P. H. Souto Ribeiro, F. Toscano, and P. Pellat-Finet. Propagation of transverse intensity correlations of a two-photon state. *Phys. Rev. A*, 79(3):033801, 2009.

[59] Reuben S. Aspden, Daniel S. Tasca, Robert W. Boyd, and Miles J. Padgett. EPR-based ghost imaging using a single-photon-sensitive camera. *New J. Phys.*, 15:073032, 2013.

[60] M. P. Buchin. Low-light imaging: ICCD, EMCCD, and sCMOS compete in low-light imaging. *Laser Focus World*, 47(51), 2011.

[61] Lijian Zhang, Leonardo Neves, Jeff S. Lundeen, and Ian A. Walmsley. A characterization of the single-photon sensitivity of an electron multiplying charge-coupled device. *J. Phys. B-At. Mol. Opt.*, 42(11):114011, 2009.

[62] D Herriott, R Kompfner, and H Kogelnik. Off-axis paths in spherical mirror interferometers. *App. Optics*, 3(4):523, 1964.

[63] D. N. Klyshko. A simple method of preparing pure states of the optical-field, a realization of the Einstein, Podolsky, Rosen experiment and a demonstration of the complementarity principle. *Uspekhi Fizicheskikh Nauk*, 154:133–152, 1988.

[64] Yoonshik Kang, Kiyoung Cho, Jaewoo Noh, Dashiell L. P. Vitullo, Cody Leary, and M. G. Raymer. Remote preparation of complex spatial states of single photons and verification by two-photon coincidence experiment. *Opt. Express*, 18(2):1217–1233, 2010.

[65] T. B. Pittman, D. V. Strekalov, D. N. Klyshko, M. H. Rubin, A. V. Sergienko, and Y. H. Shih. Two-photon geometric optics. *Phys. Rev. A*, 53(4):2804–2815, 1996.

[66] S. S. R. Oemrawsingh, J. A. de Jong, X. Ma, A. Aiello, E. R. Eliel, G. W. 't Hooft, and J. P. Woerdman. High-dimensional mode analyzers for spatial quantum entanglement. *Phys. Rev. A*, 73(3):032339, 2006.

[67] Melanie McLaren, Jacquiline Romero, Miles J. Padgett, Fillipus S. Roux, and Andrew Forbes. Two-photon optics of Bessel-Gaussian modes. *Phys. Rev. A*, 88(3):033818, 2013.

[68] Reuben S. Aspden, Daniel S. Tasca, Andrew Forbes, Robert W. Boyd, and Miles J. Padgett. Experimental demonstration of Klyshko's advanced-wave picture using a coincidence-count based, camera-enabled imaging system. *J. Mod. Optic.*, 61(7):547–551, 2014.

[69] D. V. Strekalov, A. V. Sergienko, D. N. Klyshko, and Y. H. Shih. Observation of two-photon "ghost" interference and diffraction. *Phys. Rev. Lett.*, 74(18): 3600–3603, May 1995.

[70] J. Leach, R. E. Warburton, D. G. Ireland, F. Izdebski, S. M. Barnett, A. M. Yao, G. S. Buller, and M. J. Padgett. Quantum correlations in position, momentum, and intermediate bases for a full optical field of view. *Phys. Rev. A*, 85(1): 013827, 2012.

[71] M. P. Edgar, D. S. Tasca, F. Izdebski, R. E. Warburton, J. Leach, M. Agnew, G. S. Buller, R. W. Boyd, and M. J. Padgett. Imaging high-dimensional spatial entanglement with a camera. *Nat. Commun.*, 3:984, Aug 2012.

[72] Paul-Antoine Moreau, Joe Mougin-Sisini, Fabrice Devaux, and Eric Lantz. Realization of the purely spatial Einstein-Podolsky-Rosen paradox in full-field images of spontaneous parametric down-conversion. *Phys. Rev. A*, 86(1):010101, 2012.

[73] P. Ben Dixon, Gregory A. Howland, James Schneeloch, and John C. Howell. Quantum mutual information capacity for high-dimensional entangled states. *Phys. Rev. Lett.*, 108(14):143603, 2012.

[74] Robert Fickler, Mario Krenn, Radek Lapkiewicz, Sven Ramelow, and Anton Zeilinger. Real-time imaging of quantum entanglement. *Nat. Sci. Rep.*, 3:1914, 2013.

[75] G. Brida, M. Genovese, and I. Ruo Berchera. Experimental realization of sub-shot-noise quantum imaging. *Nat. Photonics*, 4(4):227–230, April 2010.

[76] S. P. Walborn, D. S. Lemelle, M. P. Almeida, and P. H. Souto Ribeiro. Quantum key distribution with higher-order alphabets using spatially encoded qudits. *Phys. Rev. Lett.*, 96(9):090501, Mar 2006.

[77] Simon Groblacher, Thomas Jennewein, Alipasha Vaziri, Gregor Weihs, and Anton Zeilinger. Experimental quantum cryptography with qutrits. *New J. Phys.*, 8:75, May 2006.

[78] D. S. Tasca, R. M. Gomes, F. Toscano, P. H. Souto Ribeiro, and S. P. Walborn. Continuous-variable quantum computation with spatial degrees of freedom of photons. *Phys. Rev. A*, 83(5):052325, 2011.

[79] G. Michael Morris. Image correlation at low light levels: a computer simulation. *Appl. Optics*, 23(18):3152–3159, 1984.

[80] C. E. Shannon. A mathematical theory of communication. *A.T. & T. Tech. J.*, 27(623), 1948.

[81] Emmanuel J. Candes and Michael B. Wakin. An introduction to compressive sampling. *IEEE Signal Proc. Mag.*, 25(2):21–30, 2008.

[82] Justin Romberg. Imaging via compressive sampling. *IEEE Signal Proc. Mag.*, 25(2):14–20, 2008.

[83] David L. Donoho. Compressed sensing. *IEEE T. Inform. Theory*, 52(4):1289 – 1306, 2006.

[84] Yoav Shechtman, Yonina C. Eldar, Alexander Szameit, and Mordechai Segev. Sparsity based sub-wavelength imaging with partially incoherent light via quadratic compressed sensing. *Opt. Express*, 19(16):14807–22, Aug 2011.

[85] A. Shabani, R. L. Kosut, M. Mohseni, H. Rabitz, M. A. Broome, M. P. Almeida, A. Fedrizzi, and A. G. White. Efficient measurement of quantum dynamics via compressive sensing. *Phys. Rev. Lett.*, 106(10):100401, Mar 2011.

[86] Xiaodi Hou and Liqing Zhang. Saliency detection: a spectral residual approach. *Proc. IEEE Conf. Computer Vision and Pattern Recognition (CVPR)*, pages 1–8, 2007.

[87] Tie Liu, Zejian Yuan, Jian Sun, Jingdong Wang, Nanning Zheng, Xiaoou Tang, and Heung-Yeung Shum. Learning to detect a salient object. *IEEE T. Pattern Anal.*, 10(20), 2009.

[88] Bogdan Alexe, Thomas Deselaers, and Vittorio Ferrari. What is an object? *Proc. IEEE Conf. Computer Vision and Pattern Recognition (CVPR)*, pages 73–80, 2010.

[89] Syed Afaq Ali Shah, Mohammed Bennamoun, Farid Boussaid, and Amar A. El-Sallam. Automatic object detection using objectness measure. *IEEE Proc. Conf. on Communication and Signal Processing Applications (ICCSPA)*, 1:1–6, 2013.

[90] Gregory A. Howland, James Schneeloch, Daniel J. Lum, and John C. Howell. Simultaneous measurement of complementary observables with compressive sensing. *Phys. Rev. Lett.*, 112(25):253602, Jun 2014.

[91] J. E. Midwinter. Infrared up conversion in lithium-niobate with large bandwidth and solid acceptance angle. *Appl. Phys. Lett.*, 14(1):29, 1969.

[92] R. F. Lucy. Infrared to visible parametric upconversion. *Appl. Optics*, 11(6): 1329–1336, 1972.

[93] Joel Falk and W. B. Tiffany. Theory of parametric upconversion of thermal images. *J. App. Phys.*, 43(9):3762, 1972.

[94] Christian Pederson, Emir Karamehmedović, Jeppe Seidelin Dam, and Peter Tidemand-Lichtenberg. Enhanced 2D-image upconversion using solid-state lasers. *Opt. Express*, 17(23):20885–20890, 2009.

[95] Jeppe Seidelin Dam, Christian Pederson, and Peter Tidemand-Lichtenberg. High-resolution two-dimensional image upconversion of incoherent light. *Opt. Lett.*, 35(22):3796–3798, 2010.

[96] Kun Huang, Xiaorong Gu, Haifeng Pan, E Wu, and Heping Zeng. Few-photon-level two-dimensional infrared imaging by coincidence frequency upconversion. *Appl. Phys. Lett.*, 100(15):151102, 2012.

[97] Ruikai Tang, Wenjie Wu, Xiongjie Li, Haifeng Pan, E Wu, and Heping Zeng. Two-dimensional infrared and mid-infrared imaging by single-photon frequency upconversion. *J. Mod. Optic.*, pages 1–6, March 2015.

[98] Morton H. Rubin and Yanhua Shih. Resolution of ghost imaging for nondegenerate spontaneous parametric down-conversion. *Phys. Rev. A*, 78(3):033836, Sep 2008.

[99] Kam Wai Clifford Chan, Malcolm N. O'Sullivan, and Robert W. Boyd. Two-color ghost imaging. *Phys. Rev. A*, 79(3):033808, Mar 2009.

[100] Yu-Lang Xue, Ren-Gang Wan, Fei Feng, and Tong-Yi Zhang. Standoff two-color quantum ghost imaging through turbulence. *Appl. Optics*, 53(14):3035–42, May 2014.

[101] H. H. Li. Refractive index of silicon and germanium and its wavelength and temperature derivatives. *J. Phys. Chem. Ref. Data*, 9(3):561, 1980.

[102] K. W. Chan, J. P. Torres, and J. H. Eberly. Transverse entanglement migration in Hilbert space. *Phys. Rev. A*, 75(5):050101, May 2007.

[103] C. H. Séquin. Blooming suppression in charge coupled area imaging devices. *Bell Syst. Tech. J.*, 51(8):1923, 1972.

[104] F. M. Miatto, H. Di Lorenzo Pires, S. M. Barnett, and M. P. van Exter. Spatial Schmidt modes generated in parametric down-conversion. *Eur. Phys. J. D*, 66 (10):263, 2012.

[105] F Zernike. Phase contrast, a new method for the microscopic observation of transparent objects part I. *Physica*, 9:686–698, 1942.

[106] G. D. Boyd and D. A. Kleinman. Parametric interaction of focused Gaussian light beams. *J. Appl. Phys.*, 39(8):3597, 1968.

[107] Rüdiger Bachor, Christopher R. Shea, Robert Gillie, and Tayyaba Hasan. Photosensitized destruction of human bladder carcinoma cells treated with chlorine e6-conjugated microspheres. *P. Natl. Acad. Sci. USA.*, 88(4):1580–1584, 1991.

[108] E. M. M. Manders, A. E. Visser, A. Koppen, W. C. de Leeuw, R. van Liere, G. J. Brakenhoff, and R. van Driel. Four-dimensional imaging of chromatin dynamics during the assembly of the interphase nucleus. *Chromosome Res.*, 11 (5):537–547, 2003.

[109] Tomás Cizmár and Kishan Dholakia. Exploiting multimode waveguides for pure fibre-based imaging. *Nat. Commun.*, 3(1027), 2012.